THERMAL BEHAVIOR OF LITHIUM-ION BATTERIES UNDER NORMAL AND ABUSE OPERATING CONDITIONS

LİTYUM İYON PİLLERİN OLAĞAN VE OLAĞAN DIŞI ÇALIŞMA ŞARTLARINDAKİ ISIL DAVRANIŞI

TANILAY ÖZDEMİR

ASSOC. PROF. DR. ÖZGÜR EKİCİ
Supervisor
PROF. DR. MURAT KÖKSAL
Co-Supervisor

Submitted to
Graduate School of Science and Engineering of Hacettepe University
as a Partial Fulfillment to the Requirements
for the Award of the Degree of Doctor of Philosophy
in Mechanical Engineering

2022

ABSTRACT

THERMAL BEHAVIOR OF LITHIUM-ION BATTERIES UNDER NORMAL AND ABUSE OPERATING CONDITIONS

Tanılay ÖZDEMİR

Doctor of Philosophy, Department of Mechanical Engineering

Supervisor: Assoc. Prof. Dr. Özgür Ekici

Co-Supervisor: Prof. Dr. Murat Köksal

December 2022, 158 pages

This doctoral thesis investigates the electrical and thermal behaviors of Li-ion battery cells during the normal and abnormal conditions using the experimental and modeling methods. First, various standard battery tests were conducted in the study in order to define the related electrical and thermal parameters, such as specific heat, density, and open-circuit voltage. Then both galvanostatic charge and discharge experiments were conducted at various C-rates under various operating temperatures. Besides, thermal abuse tests were performed in an oven at different operating temperatures for both completely charged and discharged cells. In addition, the electrical behavior of the cell was observed at elevated ambient temperatures. Lastly, film heater experiments were conducted to investigate the thermal runaway behavior of the Li-ion cells at various SoC values under high operating temperatures.

In the modeling part, first, an axisymmetric 2-D Lumped model is developed using constant and variable internal resistance approaches to estimate the cylindrical Li-ion battery's thermal and electrical performances during various discharge

rates and operating temperatures. Then, a 1-D electrochemical and 3-D thermal model was developed in order to predict the voltage and temperature variations of the Li-ion battery. Both models were developed and implemented within the framework of COMSOL. The developed model includes a large number of geometrical, electrochemical, and thermal parameters. Therefore, a comprehensive sensitivity analysis was done to obtain the optimum model input parameters. The sensitivity analysis also presented the important parameters that can significantly alter the cell's thermal and electrical performance during the discharging processes. Lastly, four main exothermic reactions were implemented into the electrochemical model so that the total heat generation during these exothermic reactions was evaluated using the Arrhenius-type temperature-dependent equations.

Keywords: Li-ion batteries, thermal runaway, electrochemical and thermal battery model, lumped battery model, Arrhenius equations.

ÖZET

LİTYUM İYON PİLLERİN OLAĞAN VE OLAĞAN DIŞI ÇALIŞMA ŞARTLARINDAKİ ISIL DAVRANIŞI

Tanılay ÖZDEMİR

Doktora, Makina Mühendisliği Bölümü

Tez Danışmanı: Doç. Dr. Özgür Ekici

Eş Danışman: Prof. Dr. Murat Köksal

Aralık 2022, 158 sayfa

Bu doktora çalışması Lityum-iyon pillerinin, normal ve normal olmayan çalışma koşulları altındaki elektriksel ve ısıl davranışlarını incelemektedir. Çalışmada hem deneysel yöntemlerle, hem de modelleme yöntemleriyle sonuçlar elde edilmiştir. Deneysel çalışmalar kapsamında ilk olarak standart batarya testleri yapılmıştır. Özgül ısı, iç direnç ve açık devre gerilimi gibi bazı elektriksel ve ısıl parametreleri elde etmek amacıyla bir batarya test düzeneğinden faydalanılmıştır. Bu test düzeneği aynı zamanda Lityum-iyon pillerin çeşitli akımlarda ve çalışma sıcaklıklarındaki şarj ve deşarj işlemlerini gerçekleştirmek için kullanılmıştır. Bunun yanı sıra, hem tamamen dolu, hem de tamamen boş pillerin yüksek sıcaklıklardaki davranışını gözlemlemek amacıyla fırın testleri yapılmıştır. Bu çalışmalara ek olarak, Lityum-iyon pillerin yüksek sıcaklıklardaki elektriksel davranışı incelenmiştir. Son olarak, çeşitli doluluk oranlarındaki Lityum-iyon pillerin yüksek çalışma sıcaklığı altındaki ısıl sürüklenme davranışını incelemek için film ısıtıcı testleri gerçekleştirilmiştir.

Modelleme çalışmalarında ise ilk olarak iki boyutlu yığık bir model, silindirik bir Lityum-iyon pilin farklı çalışma sıcaklıkları ve deşarj koşullarındaki elektriksel ve termal özelliklerini tahmin etmek üzere, sabit iç direnç ve değişken iç direnç yaklaşımları kullanılarak geliştirilmiştir. Sonrasında ise bir boyutlu elektrokimyasal bir model ile üç boyutlu ısıl modelin birlikte kullanıldığı bir benzetimde, Lityum-iyon pil hücresinin elektriksel ve ısıl davranışları tahmin edilmiştir. Her iki model de COMSOL programı yardımıyla geliştirilmiş ve uygulanmıştır. Elektrokimyasal-ısıl model, çok sayıda geometrik, elektro-kimyasal ve ısıl parametreyi içinde barındırır. Bu nedenle, uygun değer model parametrelerini elde etmek amacıyla kapsamlı bir duyarlılık analizi yapılmıştır. Bu analiz aynı zamanda deşarj işlemleri sırasında hücrenin elektriksel ve termal davranışını önemli ölçüde değiştirebilecek parametrelerin de gözlemlenmesini sağlamıştır. Çalışmanın son kısmında, elektrokimyasal-ısıl model, Lityum-iyon pillerin normal olmayan koşullardaki davranışını incelemek amacıyla güncellenmiş ve hücredeki ısı üretimini artıran dört ana ekzotermik reaksiyon, Arrhenius tipi sıcaklığa bağlı denklemler kullanarak modele eklenmiştir.

Anahtar Kelimeler: Lityum iyon piller, ısıl sürüklenme, elektrokimyasal-ısıl batarya modeli, lumped batarya modeli, Arrhenius denklemleri.

ACKNOWLEDGEMENTS

First of all, I would like to express my sincere gratitude to my supervisor, Dr. Özgür Ekici, for his endless support, guidance, and motivation throughout my studies. He always encouraged me with his friendly and precious assistance in my academic research.

I would like to offer my special thanks to my co-supervisor, Dr. Murat Köksal, for his continuous support and guidance. I am deeply grateful due to his insightful comments, suggestions, and invaluable help.

I am also thankful to Dr. S. Çağlar Başlamışlı and Dr. İlker Tarı for accepting to be a member of my Thesis Monitoring Committee and for their enlightening comments and directions.

I would like to thank my lab mates, Dr. Ali Amini, Emre Gümüşsu, and Altay Tekin, for their support and friendship.

I sincerely thank The Scientific and Technological Research Council of Turkey (TÜBİTAK) for their financial support through national scholarship (TÜBİTAK-BİDEB 2211).

I would like to express my sincere thanks to my family, Havva, O. Cumhur, and A. Berkay Özdemir, for their endless support and love. My dear family has never hesitated to provide mental and material support throughout my studies.

Finally, I am deeply grateful to my wife, Aylin Taş Özdemir, for her patience, continuing support, and precious love.

TABLE OF CONTENTS

LIST OF FIGURES

LIST OF TABLES

SYMBOLS AND ABBREVATIONS

Symbols

a	Degree of conversion
A	Ampere
a_{surf}	Electrode specific surface area
A_e	Electrode plate area
A_{ele}	frequency factor for the electrolyte
A_{ne}	Frequency factor for the negative electrode-solvent reaction
A_{pe}	frequency factor for the positive electrode-solvent reaction
A_{sei}	Frequency factor for the SEI layer
c	concentration
c_{ele}	Dimensionless concentration of the reacting species in the electrolyte
c_{ne}	Dimensionless concentration of the Li-ion in negative electrode
c_p	Specific heat
c_{sei}	Dimensionless concentration of the reacting species in the SEI layer
d	Diameter
$D_{l,eff}$	Effective electrolyte diffusion coefficient
$D_{s,ne}$	Solid phase diffusion coefficient for negative electrode
$D_{s,pe}$	Solid phase diffusion coefficient for positive electrode
E	Equilibrium potential

E_a	Reaction activation energy
f	Electrolyte activity coefficient
F	Faraday's constant
h	Convective heat transfer coefficient
H	Released specific heat during the reaction
i_0	Exchange current density
I	Current
J_0	Dimensionless charge exchange current
J_{Li}	Volumetric rate of electrochemical reaction at the particle surface
k	Reaction rate coefficient
L	Length
m	Reaction order
n	Normal component
N_{shape}	Shape factor for coordinate
p	Bruggeman coefficient
$\dot{q}_c$	Cell heat generation rate
$\dot{q}_{mix}$	The rate of heat of mixing
$Q_{c,0}$	Cell nominal capacity
$\dot{Q}$	The rate of heat generation per unit volume
$\dot{Q}_J$	The rate of Joule heating per unit volume
r_c	Cell internal resistance
r	Radius

R	Load Resistance
R_u	Universal gas constant
Ra_d	Rayleigh number with respect to diameter
t_+	Transference number of Li-ions
T	Temperature
V	Voltage
W	Specific mass of the carbon content
y	Height

Greek Symbols

α	Charge transfer coefficient
ε	Emissivity
$\varepsilon_{s,ne}$	Solid phase volume fraction at negative electrode
$\varepsilon_{s,pe}$	Solid phase volume fraction at positive electrode
$\varepsilon_{l,ne}$	Liquid phase volume fraction at negative electrode
$\varepsilon_{l,pe}$	Liquid phase volume fraction at positive electrode
$\varepsilon_{l,sep}$	Liquid phase volume fraction at separator
η	Overpotential
λ	Thermal conductivity
ρ	Density
σ	Stefan-Boltzmann constant
$\sigma_{l,eff}$	Effective electrolyte conductivity

$\sigma_{s,eff}$	Effective electrical conductivity
τ	Diffusion time constant
ϕ_l	Electrolyte phase potential
ϕ_s	Solid phase potential

Subscript

0	Initial
a	Average
act	Activation
an	Anode
ang	Angular
app	Applied
bat	Battery
c	Cell
ca	Cathode
conc	Concentration
e	Electrode
ec	Electrochemical
eff	Effective
eq	Equivalent
ext	External
gen	Generation
IR	Irreversible
l	Liquid

ne	Negative electrode
necc	Negative electrode current collector
pe	Positive electrode
pecc	Positive electrode current collector
rad	Radial
ref	Reference
REV	Reversible
s	Solid
sei	Solid electrolyte interphase
sep	Separator
surf	Surface
surr	Surrounding

Abbrevations

Ah	Ampere hours
ARC	Acceleration Rate Calorimetry
BTMS	Battery Thermal Management System
CJC	Cold Junction Compensation
DoD	Depth of Discharge
DSC	Differential Scanning Calorimetry
ECM	Electrochemical Model
ELE	Electrolyte
FSR	Full Scale Range
Li	Lithium
LTM	Lumped Transient Model

Max	Maximum
Min	Minimum
MIV	Model input values
NE	Negative Electrode
ODE	Ordinary Differential Equation
OCV	Open Circuit Voltage
PE	Positive Electrode
RMSE	Root Mean Square Error
SEI	Solid Electrolyte Interphase
SoC	State of charge
SoH	State of Health
TM	Thermal Model
TR	Thermal Runaway

1. INTRODUCTION AND LITERATURE REVIEW

1.1 Introduction

Numerous types of research have been done to investigate batteries since the 18th century. The first Lithium-ion (Li-ion) cell was introduced in 1991 [1]. As a reliable energy storage system, Li-ion batteries are one of the favored options due to their relatively longer cycling life and higher energy density than other batteries. The rechargeability without memory effect is another prominent advantage, along with the low self-discharge rate. The Li-ion batteries can be used in both low and high-power-needed applications to sustain the required voltage and capacity whenever it is demanded. They have been mainly utilized in various applications, from electronic devices to electric/hybrid vehicles. Despite their prominent above-stated advantages, the thermal behavior of Li-ion batteries is still one of the critical areas. The chemical structure of the Li-ion battery leads to heat production during the charging and discharging processes. The generated heat is transferred within the cell by conduction and rejected via convection and radiation to the ambient. However, the produced heat may not be entirely released from the battery's surface, causing a temperature increase within the cell, adversely affecting the battery’s life cycle, state of health, and power capability in long term [2].

The increasing temperature may activate various exothermic reactions inside the cell. These reactions increase the temperature further if the heat dissipation rate is lower than the heat generation rate. Besides, abuse conditions such as heating, overcharging/discharging, nail penetration, and external or internal short circuits can also significantly increase the cell temperature. Eventually, these conditions may lead to a thermal runaway (TR) situation that not only degrades the battery’s performance but also threatens the reliability of the Li-ion cells and causes serious safety concerns for consumers.

Numerical and experimental investigations are vital for understanding the methodology of TR conditions. Abusive experiments are challenging due to

hazardous conditions that arise but essential for examining the thermal behavior of the Li-ion batteries under abnormal operating conditions. On the other hand, developing a model that predicts the thermal behavior of the batteries under abnormal operating conditions helps to foresee the critical TR initiation time, which may prevent the battery from hazardous conditions. Thus, simulation studies are required, and the development of reliable models is crucial to examine the Li-ion battery's electrical and thermal performances under normal and abuse operating conditions.

1.2. Background

1.2.1. Structure and Working Principle of Li-ion Batteries

Li-ion cell consists of a positive electrode, a negative electrode, a separator to divide these electrodes from each other as an electrical insulator, the electrolyte to provide movement of Li-ions between electrodes while charging and discharging, current collectors, and a case to cover these components [3]. Figure 1.1 displays the schematic illustration of a Li-ion battery.

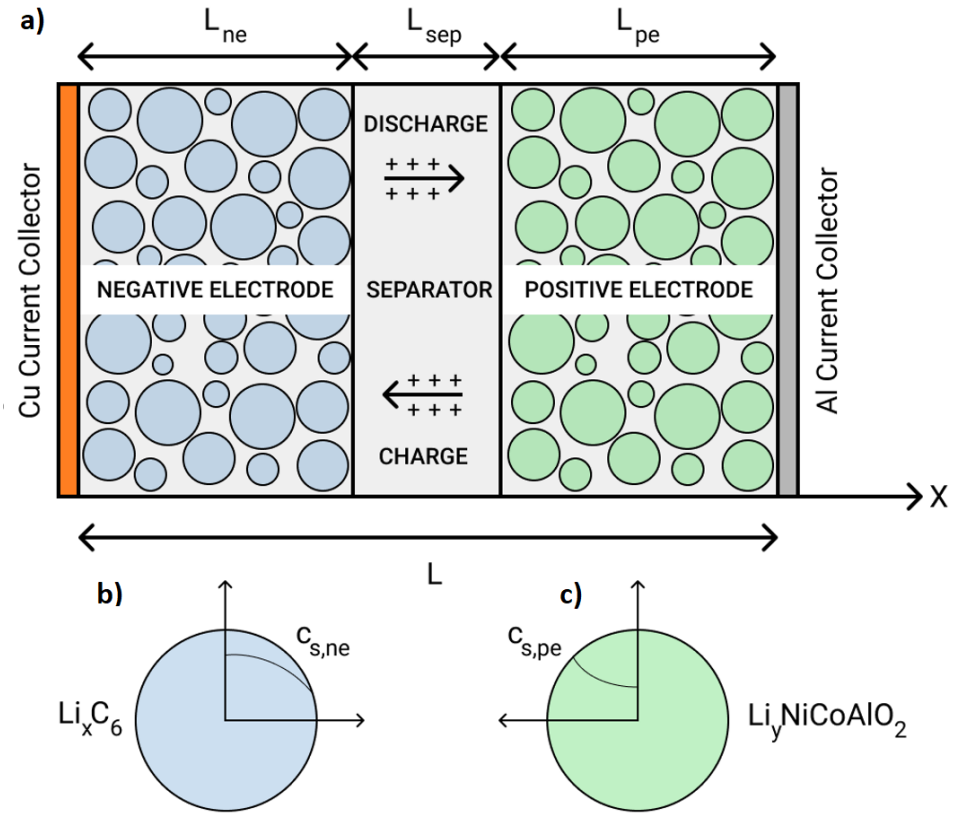

Figure 1.1 a) Li-ion cell structure. b) Negative electrode active particle. c) Positive electrode active particle.

The electrolyte is ordinarily liquid and fills the pores within the negative and positive electrodes. The electrodes include active spherical particles of various sizes. Li-ions are placed in the active material or the electrolyte. Li-ions are removed from the positive electrode during the charging process and travel to the negative electrode. The separator here works like a semi-permeable membrane, allowing the Li-ions to pass but not electrons. The electrons can only move in solids and are released concurrently from the cathode side current collector to provide the electrical balance. These electrons flow to the negative electrode through the external circuit to create the charge current. The inverse process emerges during the discharging process [4].

1.2.2. Geometry of the Li-ion Cells

The contents and geometry of Li-ion cells may vary depending on the area in which they are used. Li-ion batteries are geometrically classified as cylindrical, coin, pouch, and prismatic cells in Figure 1.2.

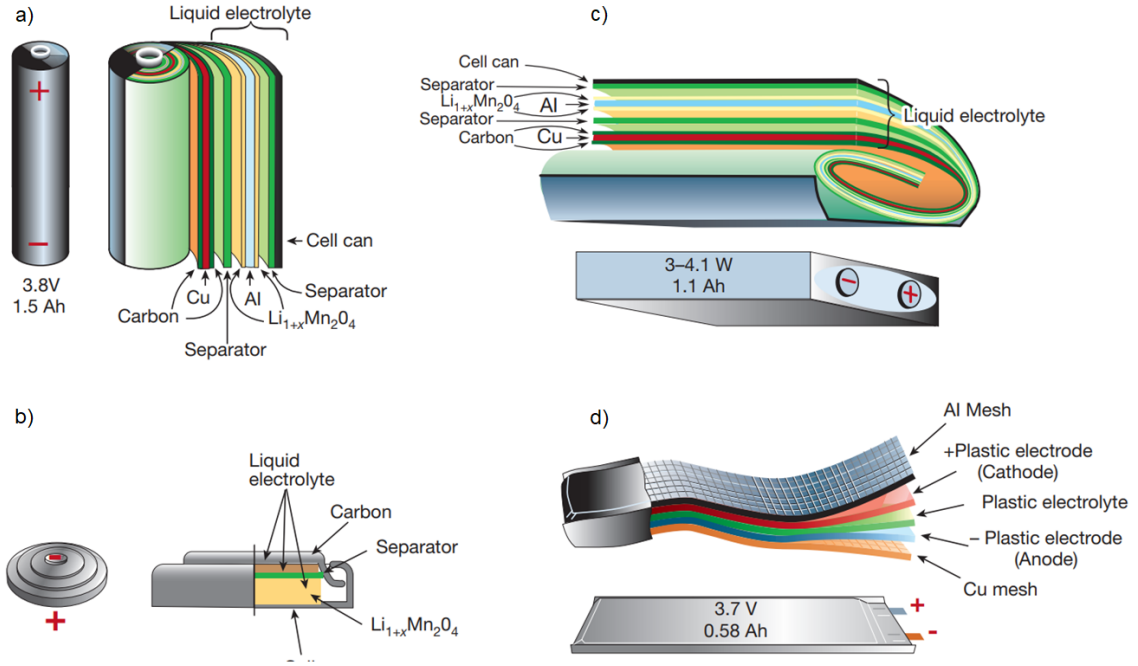

Figure 1.2 a) Cylindrical cell geometry, b) Coin cell geometry, c) Prismatic cell geometry, d) Pouch cell geometry [5].

The cylindrical Li-ion cells are the most preferred option due to their low cost and high energy density. Their size is referred to by five numbers in which the first two digits denote the cell diameter in mm. Meanwhile, the last three digits define the cell length in mm. 18650, 26650, 21700, and more cylindrical Li-ion cells are currently employed in different fields, such as hybrid and electric cars, laptops, and other portable electronic devices.

The coin cells are low-power sources that are convenient for compact and portable devices since they are minimal. Their usage areas are implants in the medical industry, wrist watches, cars, and garage keys [6].

The prismatic cells provide a higher density of energy and better use of space than the other types of batteries, which increases the flexibility of designers, but manufacturing costs can be significantly higher [6]. Prismatic cells are commonly used in smartphones, laptops, and electric vehicles.

The pouch cells have the highest packing efficiency and gravimetric energy density compared to the other battery types. However, they are prone to mechanical damage and thermal conditions. Pouch cells are primarily used in the military, automotive, and aerospace industries [6]. The benefits and drawbacks of the Li-ion cells, according to their geometric shapes, are given in Table 1.1.

Table 1.1. Li-ion battery's advantages and disadvantages according to their geometrical shapes [3, 6].

Cell Geometry	**Advantages**	**Disadvantages**
Cylindrical	Relatively cheap. Relatively easy production.	High series inductance. Packing efficiency is low.
Coin	Relatively cheap. Produced for compact portable devices.	Relatively unsafe.
Prismatic	Improves space utilization. Increases flexibility. High capacity	Expensive. Risk of swelling.
Pouch	High gravimetric energy density. Efficient packing.	Vulnerable to external damages. Allowing high heat transfer rate among adjacent cells. Risk of swelling

1.2.3. Fundamental Concepts About the Li-ion Batteries

1.2.3.1. Capacity

The Li-ion battery's capacity can be defined in ampere-hours (Ah), which indicates the generated electricity within the battery [7]. The cell capacity relies on the active material substance on the electrodes [8].

Although Li-ion batteries can be recharged, they have limited utilization time, and their lifespan is defined by the amount of charge and discharge. Besides, each experienced charging/discharging cycle leads to a capacity reduction called aging.

1.2.3.2. C Rate

The term C rate is typically used to define the applied current more straightforwardly, as seen in Eq. (1.1).

$$\text{C-rate} = \frac{\text{Applied Current (A)}}{\text{Capacity (Ah)}} \tag{1.1}$$

For instance, discharging a cell at 1C rate corresponds to a current value that can completely discharge the cell in an hour. In this study, the NCR18650b cell capacity is 3.25 Ah, so 1C rate implies applied current to the cell is equal to 3.25 A.

1.2.3.3. State of Charge

The battery's State of Charge (SoC) is indicated by the ratio of the instant charged capacity to its maximum charged capacity. It shows the charge condition of a Li-ion cell between 0 and 1; one for a fully charged cell and zero for a fully discharged cell.

For instance, if the SoC value is 1, it implies the negative electrode side reaches its maximum allowable Li-ion concentration, which also denotes that the battery has reached its maximum available capacity. SoC limits are specified by the manufacturers for each cell type and correspond to a certain voltage value. The upper and lower voltage limits are adjusted for the battery used in this study as 4.2 V and 2.5 V, respectively.

1.2.3.4. Depth of Discharge

The depth of Discharge (DoD) value of a battery expresses the amount of discharged part of a Li-ion cell between 0 and 1. It equals zero for a fully charged cell and one for a fully discharged cell.

1.2.3.5. State of Health

The State of Health (SoH) denotes the ratio of the cell's maximum charged capacity to its rated capacity. It gives an opinion about the remaining number of cycles the cell will be experienced. A Li-ion cell can be perfectly healthy if its current capacity is equal to the rated capacity, which shows that the battery has no charging or discharging history.

1.2.3.6. Open Circuit Voltage

The battery's Open Circuit Voltage (OCV) value demonstrates the voltage value when there is no applied current to the cell [9]. A voltmeter or digital multimeter can measure the OCV value of the cell. However, the measurements after a charge or discharge should be done by considering the chemical stabilization process within the cell. In this study, the experimental data show that the NCR18650b Li-ion cells can be assumed as chemically stable after an approximate 4-hour resting period. OCV value of the cell is calculated as,

$$OCV = I(r_c + R) = Ir_c + V \tag{1.2}$$

where, I denotes the applied current, r_c is the cell's internal resistance in ohms, R is the load resistance in the circuit in ohms, and V is the cell voltage.

1.2.3.7. Internal Resistance

The internal resistance denotes the cell's resistance to the applied load and mainly depends on the age condition, ambient temperature, and the applied current. It can be calculated by rearranging Eq. (1.2).

$$r_c = \frac{OCV - V}{I} \tag{1.3}$$

1.2.3.8. Solid Electrolyte Interphase (SEI)

Li-ions move between the cathode and anode sides during the charge and discharge operations. SEI layer forms on the surface of the anode side after the first charging-discharging cycle. The SEI layer prevents the decomposition of the electrolyte by hindering the electron transfer from the anode to the electrolyte. It also allows the Li-ions to travel between the anode and electrolyte. On the other hand, unstable components can cause a thickening of the layer, increasing the resistance and reducing the battery capacity. Thus, the optimum usage conditions of the SEI layers are still under investigation [10, 11].

1.2.3.9. Overpotential Terms in Li-ion Batteries

The overpotential defines the potential difference produced by the internal resistance [12]. As mentioned in this chapter, the cell voltage is named OCV if there is no applied current to the cell. The overpotential, on the other hand, changes the cell's OCV during the current applied applications [13]. Typical voltage variations are presented in Figure 1.3 for various charging (a) and discharging (b) processes at room temperature. The overpotentials alter the cell's voltage and mainly consist of ohmic, activation, and concentration terms.

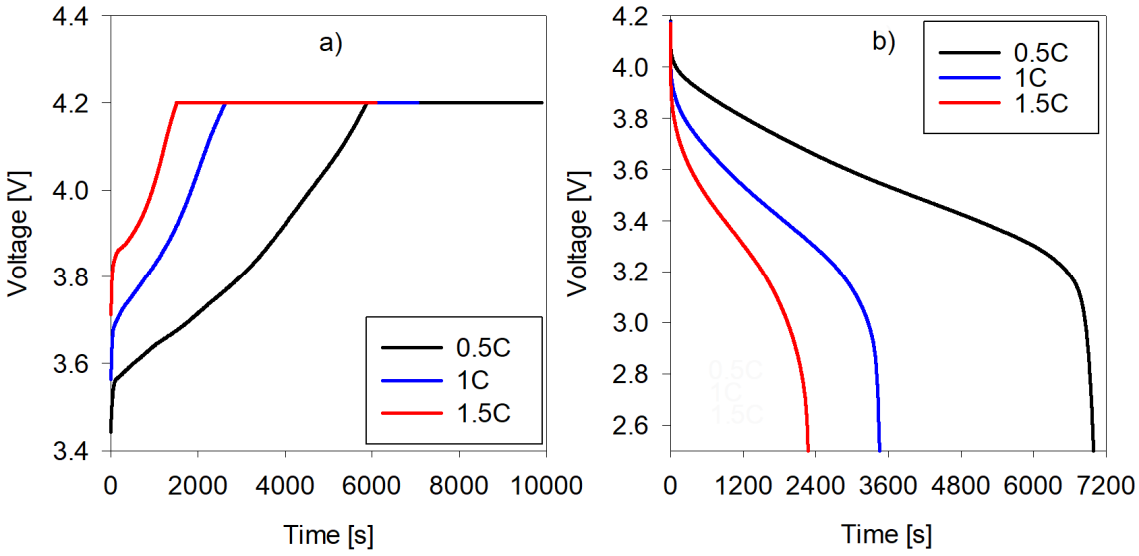

Figure 1.3. Voltage variations of the cell during 0.5-1-1.5C rate charging (a) and discharging (b) processes.

Ohmic overpotential causes voltage changes due to the ohmic resistance within the cell. Activation overpotential is associated with electrochemical kinetics and electron migration [14]. Concentration overpotential describes the mass transport limitations associated with electrochemical processes. The voltage changes regarding the concentration overpotential may reach high values as the current density increases [15].

1.3. Literature Review

1.3.1. Thermal Behavior of Li-ion Batteries

The Li-ion batteries generate heat during both charging and discharging. Bernardi et al. [12] developed an energy balance equation for a single cell and demonstrated that the heat sources within the discharging cell are due to the electrical power (irreversible, also known as Joule heating), entropic heating (reversible), mixing, and phase changes. Recent studies that mainly focused on the thermal behavior of the batteries mostly neglect the mixing and phase change effects and simplify the generated heat to reversible and irreversible terms, as presented in Eq. (1.4).

$$\dot{q}_c = I(OCV-V)-I(T\frac{\partial OCV}{\partial T}) \quad (1.4)$$

The reversible term significantly affects heat generation at low discharge currents [13, 14]. However, it can be neglected in high-current applications since the irreversible term dominates the heat production from the cell [15, 16]. On the other hand, the reversible term depends on SoC and operating conditions such as ambient temperature. Therefore, some studies [17, 18] assume that it varies as a function of SoC. Besides, some [19, 20] disregard the variation of this term for simplicity.

The battery's electrochemical and thermal characteristics, geometrical structure, and operational conditions significantly affect heat production. The generated heat is transferred within the cell by conduction and rejected via radiation and convection to the ambient. Thus, the natural heat transfer from the battery surface mostly depends on the ambient temperature that directly affects the thermal performance of the battery.

Both operation and storage temperatures strongly influence Li-ion batteries' performance, lifespan, and safety [21]. Motloch et al. [22] indicate that at a temperature between 30-40°C, each increment of working temperature causes a reduction in the battery life of approximately two months. Li-ion batteries' current operating temperature is settled to between -20°C and 60°C [23], but a restricted temperature range from 15°C to 35°C is suggested to preserve its optimal performance [24].

The thermal and electrical characteristics of the cell are also adversely influenced by the cold ambient. Low operating temperature causes less ionic conductivity within the cell and restricts ion movement, leading to high internal resistance [25]. Besides, charging at low temperatures leads to a critical lithium plating situation, which reduces the battery capacity [26].

Moreover, the cell's energy density and capacity significantly decrease at low temperatures, which could create serious range problems for electric vehicles that operate in cold climates. Nagasubramanian [27] compared the volumetric energy density of the cell at 25°C and -40°C operating temperatures and stated that the cell's energy density reduced from 100 Wh/L to 5 Wh/L at -40°C.

The thermal behavior of Li-ion batteries under different operating conditions and varying power requirements is an important aspect that needs to be researched in detail since it significantly affects the power capability, life cycle, charge acceptance of the battery, and safety [2]. Thus, many models have been developed in the literature to predict the thermal characteristics of Li-ion batteries [28, 29]. These models can be classified into three main categories; physics-based electrochemical models [12, 30-39] with high complexity that investigate the battery mechanism in detail, data-based models [2, 40-49] with relatively low accuracy that utilize empirical relationships to predict the battery dynamics, and equivalent circuit-based models [8, 28, 29, 50] with acceptable accuracy and complexity that utilize active and passive electrical components to estimate the battery states [28].

In thermal models, the main aim is to predict the temperature variation within the battery during the charging/discharging processes, considering the heat generation and the heat dissipation from the battery. A battery thermal model should work accurately under standard test conditions such as galvanostatic charging/discharging. Many studies investigate only the galvanostatic discharging processes at various C rates from 0.5 to 5 C [23, 30, 33, 35, 41, 43, 49]. Some studies also investigate the charging and discharging behavior of the cell separately [37, 38, 44, 46, 47, 51-53], or in driving cycle applications [31, 32, 36, 42, 48, 54]. Table 1.2 presents a classification of the available major numerical and experimental Li-ion battery studies in the literature on charge/discharge processes.

Table 1.2. Numerical and experimental studies investigating charge/discharge processes and driving cycle behavior.

Application	Experimental	Numerical and Experimental
Galvanostatic discharge	[23]	[30] [33] [35]* [41] [43] [49]
Galvanostatic charge and discharge	[51-53]	[37, 38] [44] [46]** [47]
Driving cycle	[54]*	[31] [32]** [36]** [42]* [48]

*No thermal investigation.

** Charging process is not modeled.

1.3.1.1. TR Behavior of Li-ion Batteries

Li-ion cells are usually connected and used in battery packages in relatively high-power needed applications, so there is a possibility to propagate the generated heat between the cells. Eventually, the increment in the battery temperature can trigger exothermic side reactions, exponentially increasing the cell's heat generation and possibly leading to a TR condition [21]. This undesired condition can emerge due to mechanical, electrical, and thermal abuse conditions. In this section, studies regarding mechanical abuse conditions will be introduced first. Then, some studies that handled the electrical abuse of the batteries will be discussed. Eventually, research on the batteries exposed to abnormal thermal conditions will be presented.

Nail penetration tests are usually performed to examine the TR of Li-ion cells. Feng et al. [55] built a 3-D TR propagation model and examined a nail penetration case for a battery pack including six pouch cells, as shown in Figure 1.4. They validated the model through experiments and proposed four methods to delay or prevent TR propagation by:

- Increasing the resistance of the separator to elevated temperatures by adjusting it.

- Decreasing the released electric energy during TR by discharging the battery.
- Improving the convective heat transfer by increasing the heat transfer coefficient.
- Preventing TR propagation by using a low-conductive layer between the batteries.

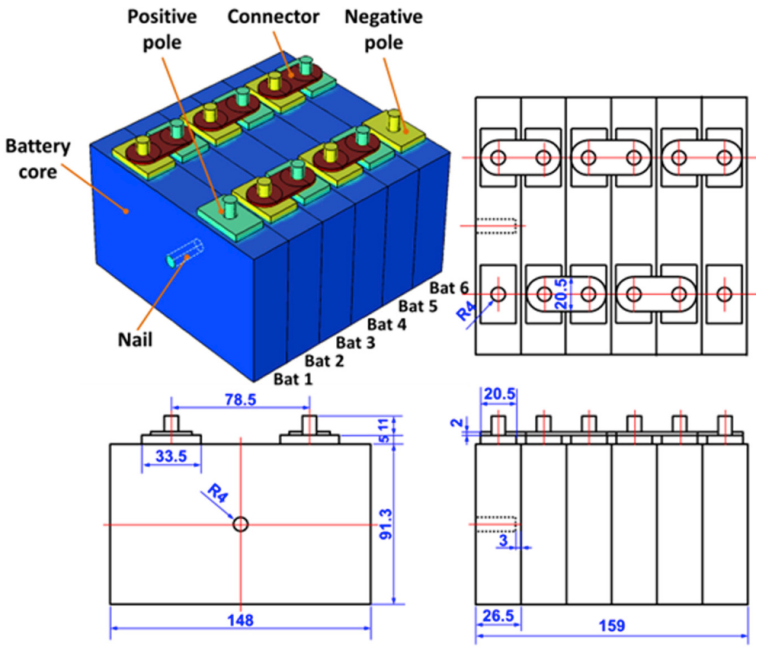

Figure 1.4. Nail penetration model including six prismatic battery cells [55].

Chiu et al. [56] developed an electrochemical model to predict the initiation of the TR and the thermal behavior of the LMO prismatic cell during a nail penetration experiment. The simulation employs thermal abuse equations to predict the heat generation rate from the exothermic side reactions. They validated the model results with the experiments.

Abuse conditions such as overcharging, over-discharging, internal short circuits, and external short circuits are the electrical reasons that may lead the cell into a TR. An external short circuit occurs when a conductor connects the electrodes with a voltage difference. Unlike penetration, the released heat generally does not heat the cell [57].

Zavalis et al. [58] developed a 2D coupled electrochemical-thermal model to examine three short circuit scenarios of a short-circuited prismatic battery cell, such as a nail penetration, an external short circuit, and an impurity-induced short circuit. They found that the initiation time of the exothermic side reactions is similar in each scenario. Besides, they also demonstrated that the temperature increment rate is strongly influenced by the Li-ion's mass transport within the electrolyte.

Another electrical abuse condition that can initiate a TR is overcharging. The main overcharging situations can be listed as electrolyte decomposition, anode and cathode failure, and Lithium plating (formation of metallic lithium around the anode during charging) [59].

Ouyang et al. [60] investigated the overcharged-induced capacity fading behavior of a 20 Ah pouch Li-ion battery. They divided the 0.5C rate overcharging phase into four different regions in order to observe the resistance, temperature, and voltage values, as stated in Figure 1.5. The cell temperature increased after 20% overcharging, and the TR occurred at an SoC value of 169%.

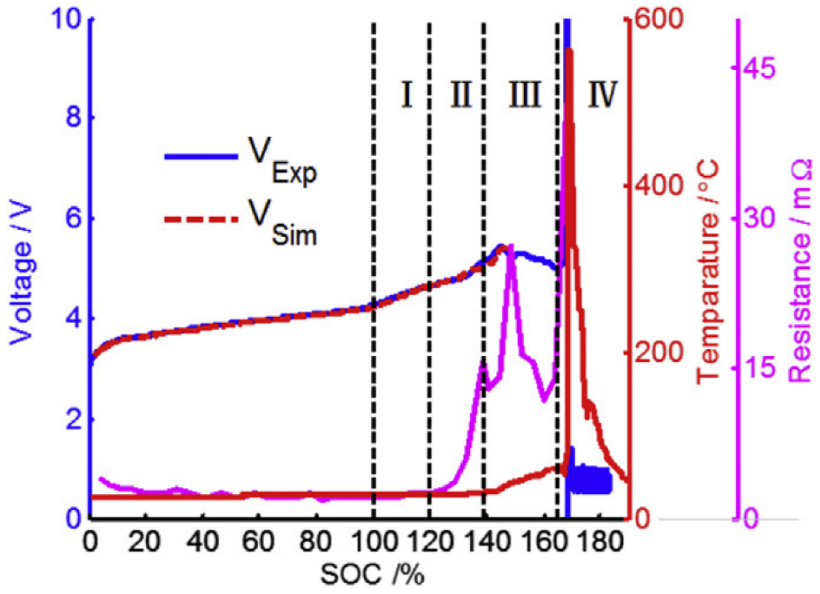

Figure 1.5. Thermal behavior of an overcharged battery [60].

Thermal abuse models examine the cell's TR behavior under elevated operating temperatures. The combined models are validated with the experiments conducted either at a predetermined temperature or with a specified rate of temperature increase. Most studies handle a single-cell model, but some investigate the effects of using multiple cells. These models can be developed in multiple dimensions. It is apparent that 3D modeling results in a better illustration of the thermal behavior of cells, but it requires high computational effort. Furthermore, the required thermal and chemical parameters must be obtained in each dimension. Abuse thermal models can evaluate the heat generation term in different approaches, such as using calorimetry-based experimental methods or modeling the electrochemical side reactions within the battery by using the calorimetric measurements to define the temperature based-parameters of the Arrhenius equations.

Lopez et al. [61] examined a model that estimates cell behavior under elevated operating temperatures. They validated the model considering the oven experiments, and the oven temperature effect, abuse reactions, physical configuration, and convection conditions were determined. They compared two distinct models with the test results to observe the cell temperature during TR and found that the model considering the reactions in the electrolyte represents the thermal behavior of the cell better than the other model, as stated in Figure 1.6. On the other hand, they calculated the cell surface temperature at various convective heat transfer coefficients such as 1, 5, 15, and 45 W/m^2K delayed the TR initiation time. However, none of those h values were sufficient to prevent the TR.

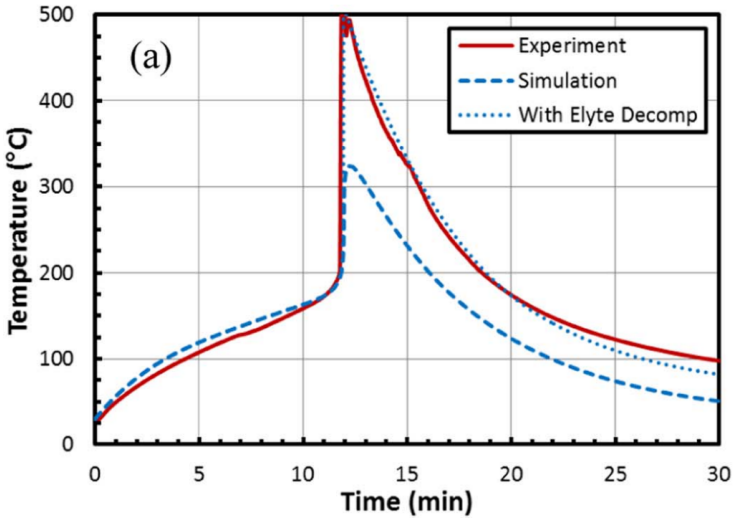

Figure 1.6. Temperature variations of the Li-ion cell under the abuse operating condition [61].

Esho et al. [62], Peng et al. [63], and Abada et al. [64] also investigated the influences of the convection heat transfer coefficient around a single cell. Esho et al. [62] developed a method for predicting the cell's critical temperature. Experimental results in different circumstances were found reasonable with the model predictions. The variation of critical temperature with respect to h is presented in Figure 1.7 for the cells with two different radial thermal conductivities. The critical temperature increases as the h increases, which indicates that the possibility of TR in a cell can be reduced by increasing the h value. The figure also demonstrates that increasing the cell conductivity increases the critical cell temperature, which helps delay the TR condition apart from the cell's convective heat transfer coefficient.

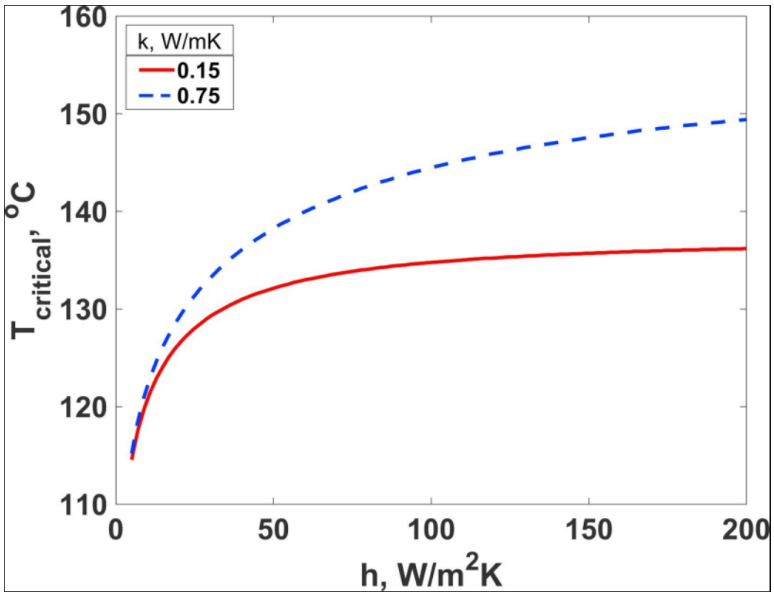

Figure 1.7. Critical temperature variations for the cells of different radial thermal conductivities [62].

Peng et al. [63] built a thermal abuse model to investigate the heat generation contributions from the decomposition and electrode-solvent reactions. They also observed the thermal behavior of the battery at various oven temperatures and the equivalent heat transfer coefficient values. The TR condition is prevented at various oven tests as the h increases from 0.1 to 45 W/m^{2}K. On the other hand, simulations demonstrated that the negative electrode-solvent reaction leads to maximum heat generation contribution during the oven test at 155°C. However, the reaction in the positive electrode was found as the most dominant heat generation for the 175°C oven test that ended up with a TR. These cases are compared in the following figure at a constant convection heat transfer coefficient of 1.5 W/m^{2}K.

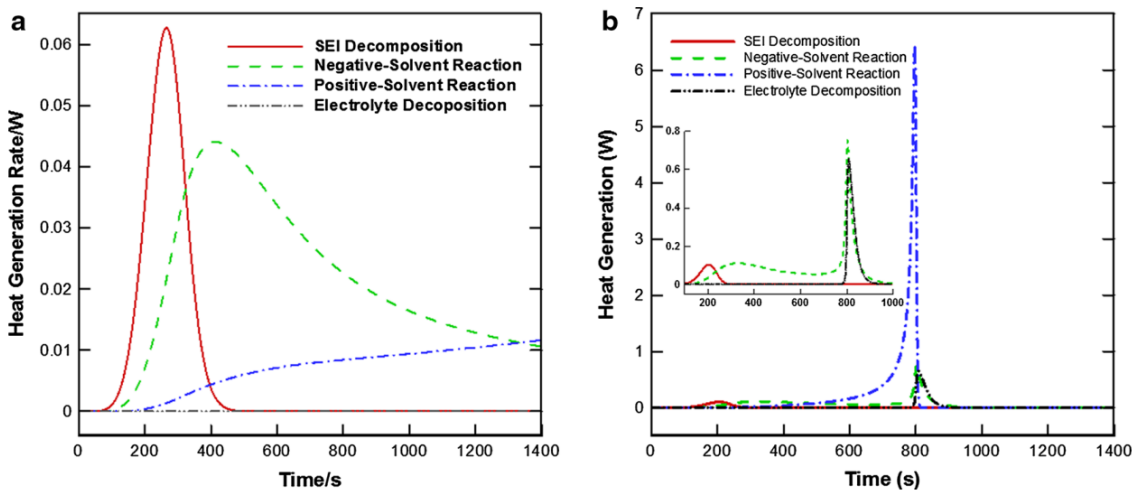

Figure 1.8. Heat generation rates of the various exothermic side reactions during the oven tests at a. 155°C and b. 175°C when 1.5 W/m^{2}K [63].

Thermal abuse models typically involve four main exothermic side reactions, which occur in the SEI layer, electrolyte, positive electrode, and negative electrode. However, some models in the literature [64, 65] regard the additional factors that can contribute to heat generation within the cell.

Abada et al. [64] created a model to observe the effects of calendar aging on the onset of TR temperature. They found that as the SEI layer thickness increases, it blocks the Li-ion's diffusion to the negative electrode so that it degrades later and delays the TR initiation time.

They also defined the h value around the cell as an equivalent heat transfer coefficient (h_{eq}) and investigated the impact of h_{eq} on the average surface temperature of the cell at 180°C and 200°C external temperatures, as presented in Figure 1.9. As the previous studies emphasized, the increment of h_{eq} prevents or delays the TR.

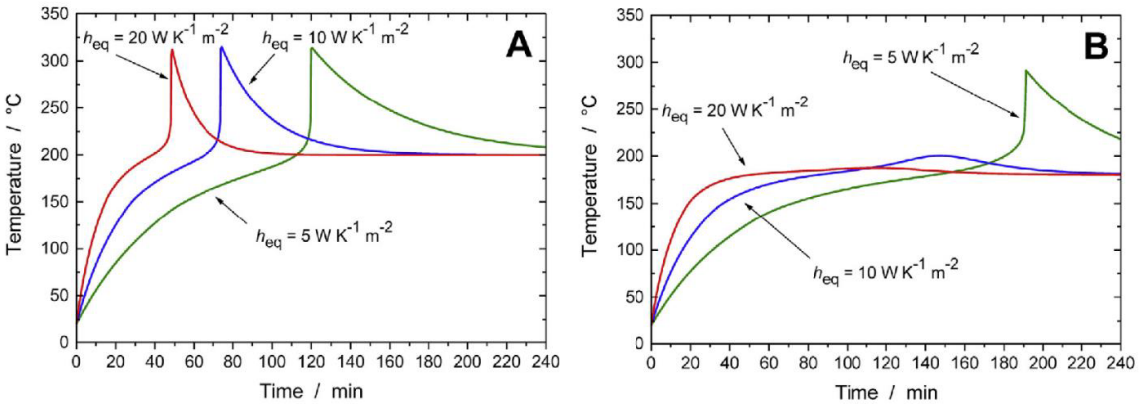

Figure 1.9. Average surface temperature vales of the cell at different equivalent heat transfer coefficients when A. T_{ext} is 200°C, B. T_{ext} is 180°C [64].

Coman et al. [65] developed a lumped model considering the heat generations during the cell's decomposition, venting, and boiling processes. To emphasize the contribution of the venting process, they compared the model results (with and without the venting effect) with the experimental data, as shown in Figure 1.10. They proved that the effects of the venting process are significant since the initiation time of the TR was predicted better with the model that considered the venting process.

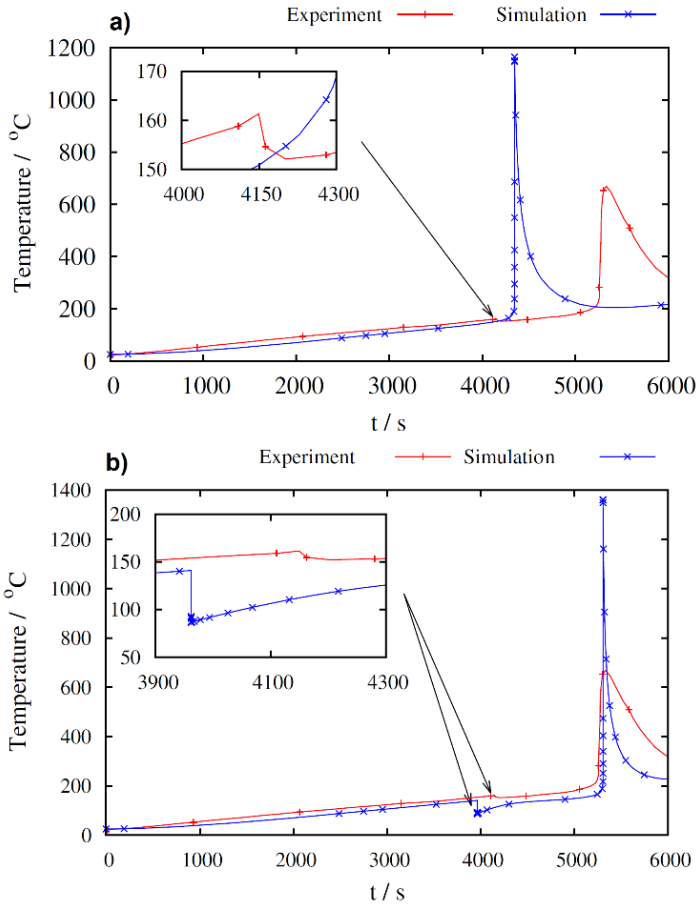

Figure 1.10. Comparison of the experimental and simulation results a) without considering the venting effects, b) considering the venting effects during the heating process at 2 °C/min [65].

Abuse models in literature usually do not consider the temperature variation within the cell and use lumped modeling methods for simplicity. Parhazi et al. [66], on the other hand, developed a model to predict the Li-ion cell's core temperature during a TR situation. The model uses the surface temperature values and is developed by considering the heat diffusion and Arrhenius equations. They employed the developed model in previous cases that experienced a TR and found out that the temperature difference between the cell core and surface may exceed hundreds of degrees Celsius, indicating the importance of predicting the cell's core temperature.

The TR behavior of the battery packages is examined in different cases [67-69], especially to monitor the thermal propagation between the adjacent cells. Huang et al. [67] forced seven 50 Ah batteries into TR by heating one of the batteries from the bottom. They also used Samenov and Frank-Kamenetskii approaches and the four main Arrhenius equations in order to analyze the TR onset and propagation within the battery module.

Anderson et al. [68] also heated five pouch 7Ah-cells and investigated the batteries' TR and fire propagation with experimental and numerical methods. They experimentally obtained the heat release rates at various SoC values but used only 75% SoC condition in the modeling part. The experimental results are underpredicted for the neighboring cell yet seem reasonable until the runaway initiation time.

Yeow and Teng [69] developed a model to investigate the TR behavior of a battery module for two cases, with and without a cold plate. Simulation results showed that the cell in the middle should reach at least 165°C to lead the module into a TR for each case. The heating rate due to the runaway is obtained by ARC (Acceleration Rate Calorimetry) test. The numerical results were compared with the literature and reasonably predicted the critical TR characteristics, as stated in Figure 1.11.

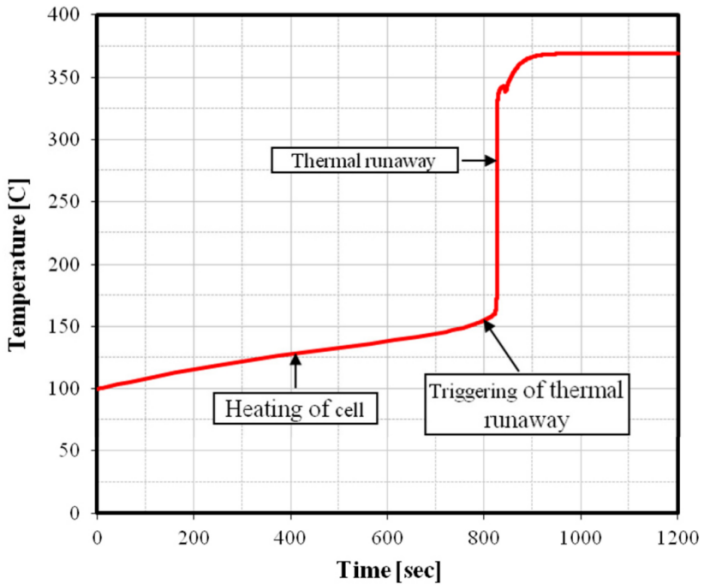

Figure 1.11. Simulated single cell TR in 150°C oven [69].

Tanaka and Bessler [70] simulated the formation and the decomposition of the SEI layer of a Li-ion cell with a one-dimensional model under constant and increasing ambient temperatures. They validated the model by comparing the results with previous research by Pasquier et al. [71], in which the heat released from the negative electrode reaction was measured by the differential scanning calorimetry (DSC) method. The simulation results were reasonably matched up to 525 K.

Calorimetry methods directly measure the amount of heat dissipation from the cell under certain conditions and help the model predict the cell's thermal behavior with less complexity. Besides, calorimetric measurements can also be used to validate the simulation results. Melcher et al. [72] developed an electrochemical-thermal coupled model and used temperature-dependent Arrhenius equations to predict heat generation due to exothermic side reactions within the Li-ion battery. Arrhenius equations were modeled with a constant fuel approach which assumes the dimensionless concentration term constant during the exothermic reactions. As a result of this study, they classified the TR behavior of the cell using three different regions considering the exothermic and electrochemical heat sources, as stated in Figure 1.12.

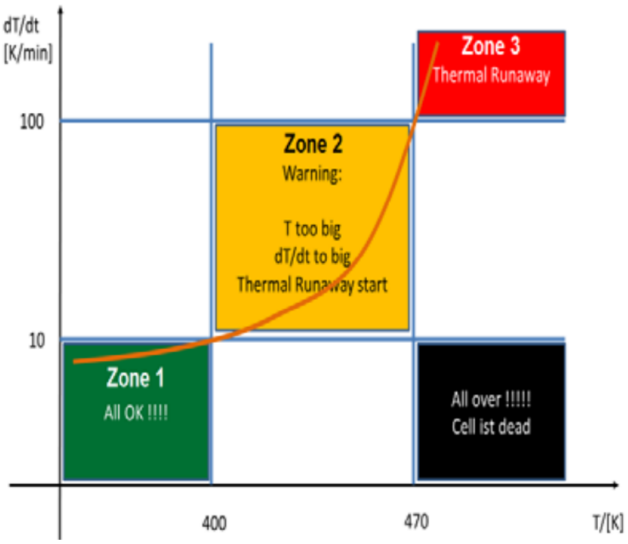

Figure 1.12. TR classification in the temperature rate vs. temperature plot [72].

Tables 1.3, 1.4, and 1.5 summarize studies investigating the thermal behavior of the li-ion cells under mechanical, electrical, and thermal abuse operating conditions, respectively. The battery type, test conditions, and model specifications are presented in these tables. Note that Ref. denotes reference, N stands for numerical research, and E indicates experimental research.

Table 1.3. Major Mechanical Abuse Applications from Literature.

Ref.	N-E	Battery Type	Test Condition
[55]	N & E	Prismatic.	0.1m nail penetration.
[56]	N & E	5.25 Ah LMO prismatic.	3mm nail penetrates with the speed of 10 mm/s.
[73]	N & E	NCM prismatic.	Nail penetration.
[74]	N & E	0.65, 3, 5 Ah Pouch LCO.	1.8 mm nail penetration from the center of the cell.

[75]	N & E	LFP 18Ah, NMC 25Ah pouch.	Pinch method.
[76]	N & E	2.2 Ah cylindrical LCO cell.	Rod, circular punch, three-point ben, flat plate tests. Speed is 1mm/min.
[77]	N & E	2.1 Ah cylindrical Sony Vtc4.	Flat plate, rigid rod, hemispherical punch tests.

Table 1.4. Major Electrical Abuse Applications from Literature.

Ref.	N-E	Battery Type	Test Condition
[78]	N & E	40 Ah NCM+LMO composite pouch.	Overcharge and Overdischarge tests at 0.33-0.5-1C rates.
[79]	N & E	2.4 Ah cylindrical NCA.	Short circuit by melting the wax in the separator.
[80]	N & E	Cylindrical NCM.	Charging and discharging at high C rates up to 18.
[81]	N & E	10 Ah NMC.	Overcharging with 2C rate.

Table 1.5. Major Thermal Abuse Applications from Literature.

Ref.	N-E	Battery Type	Test Condition
[61]	N & E	Cylindrical LCO.	T_{oven}= 145, 150, 155, 160, 170°C, h= 5, 10 W/m^{2}K
[62]	N & E	Cylindrical Li-ion.	T_{oven}= 160°C,
[63]	N & E	LCO.	T_{oven}= 135 to 215°C,

			h= 0.1 to 45 W/m^{2}K
[64]	N & E	Cylindrical, 2.3 Ah LFP/C.	T_{oven}= 180 to 250°C, 5°C/min
[65]	N	Cylindrical LCO.	2°C/min
[66]	N & E	Cylindrical LCO, NMC, LMO.	T_{oven}= 170, 240°C,
[67]	N & E	50 Ah NCM, LTO.	Constant heat source. Heating rate: 0.1 to 3.3°C/min
[68]	N & E	7 Ah LiFePO4 pouch.	15 kW propane burner, h= 25 W/m^{2}K
[69]	N	70 Ah NMC Pouch.	T_{oven}= 150°C, h = 10 W/m^{2}K, ε = 0.8.
[70]	N	Cylindrical Li-ion.	T_{amb}= 373 K, 400 K, 500 K
[72]	N & E	Cylindrical LCO.	Heating rate= 5 K/min
[82]	N & E	Cylindrical LCO.	T_{oven}= 150, 155°C h= 7.17 W/m^{2}K, ε = 0.8
[83]	N & E	55 Ah LiFePO4 prismatic.	T_{oven}= 140 to 160°C, h= 8.7 W/m^{2}K, ε = 0.8
[84]	N	Cylindrical LMO.	T_{amb}= 70°C, h= [-20,4] W/m^{2}K
[85]	N & E	Prismatic 24 Ah NCM.	T_{oven}= 130, 150°C, Heating rate= 5 to 20°C/min
[86]	E	2.4 Ah Cylindrical LMO.	T_{oven}= 215°C,

			Heating rate= 5°C/min
[87]	N & E	Cylindrical LiNiCoAlO based.	T_{oven}= 135, 140, 145, 150°C, Heating rate= 5, 10°C/min
[88]	N & E	1.5 Ah cylindrical LFP.	T_{oven}= 180, 218 and 250°C

Operating the Li-ion batteries under inconvenient conditions will adversely affect their electrical and thermal performance. Previous investigations have shown that the elevated temperature region around the cell should be dissipated to minimize the thermal effects on Li-ion batteries. Besides, severe temperature non-uniformity could not be allowed in the battery packages, and the maximum temperature difference between cells should be kept below 5°C to avoid the adverse effects of temperature maldistribution [2]. Thus, thermal management systems are necessary to provide the optimum operating conditions for Li-ion batteries and avoid TR conditions as well as possible.

1.4 Aim and Scope

Li-ion batteries have gained wide popularity in many applications due to their salient features, such as continuously improving life span, energy density, and discharge/charge efficiency [8, 52]. These features of Li-ion batteries are significantly affected by operating conditions as well as the thermal characteristics of the cell. Besides, the possibility of the TR condition threatens the reliability of the Li-ion cells and causes serious safety concerns for consumers. Therefore, reliable mathematical models are still needed to investigate the thermal behavior of Li-ion batteries under normal and abuse conditions.

As can be inferred from the literature review, the modeling studies in regarding the thermal behavior of Li-ion batteries offer varying degrees of complexity for the electrochemical and thermal parts. One of the common problems in all of these

studies is the extensive number of geometrical, thermal and electrochemical properties/parameters used and the possible uncertainty in their values. Due to the complex material structure of Li-ion batteries, measurements of these properties/parameters are often difficult. The effects of these parameters on the model results – regardless of the modeling approach – should be evaluated. Furthermore, most of the studies do not consider the effects of the temperature field on the convective heat transfer coefficient around the cell and neglect the radiative heat transfer Additionally, thermal abuse investigations are rare in the literature for the NCR18650b cylindrical Li-ion batteries.

Hence, the aims of this study are:

- To observe and investigate the thermal and electrical behaviors of the Li-ion batteries exposed to galvanostatic charging/discharging processes along with the thermal abuse operating conditions.
- To develop a comprehensive model that considers the effects of the convection and radiation heat transfer around the cell and predicts the thermal behavior of the Li-ion batteries under various discharging conditions and operating temperatures.
- To develop a thermal abuse model for accurately predicting the TR characteristics of the NCR18650b cylindrical Li-ion batteries,
- To investigate the electrical and thermal impacts of geometrical, electrochemical, and thermal parameters with a comprehensive sensitivity analysis.

This doctoral thesis investigates the thermal and electrical behaviors of Li-ion batteries under normal and abusive operating conditions and involves both experimental and modeling parts.

In the experimental part of this thesis, galvanostatic charge and discharge tests were performed at different C-rates under various operating temperatures. In addition, thermal abuse experiments were conducted using temperature adjustable oven and film heater. The oven tests were performed at different

operating temperatures for the Li-ion batteries at 0 and 1 SoC values. Finally, film heater tests were performed at 0, 0.5, and 1 SoC conditions. In one of the cases, the battery was also exposed to discharging conditions that lasted until the venting process.

In the modeling part, first, an axisymmetric 2-D Lumped model was developed with constant and variable internal resistance approaches to estimate a cylindrical Li-ion battery's thermal and electrical characteristics during various discharge rates at different operating temperatures. Then, a 1-D electrochemical model coupled with a 3-D thermal model was developed to predict the thermal and electrical behaviors of a Li-ion cell. Both models were developed and implemented within the framework of COMSOL, a finite element-based multiphysics solver. The electrochemical-thermal coupled model includes extensive number of geometrical, electrochemical, and thermal parameters. Therefore, a comprehensive sensitivity analysis was performed to obtain the optimum model input parameters. The sensitivity analysis also presented the important parameters that can significantly alter the electrical and thermal behavior of the cell during the discharging processes. Lastly, in order to model the TR, the electrochemical and thermal model was enhanced by adding temperature-dependent Arrhenius equations representing the four main heat generation contributions of the decomposition reactions during the TR. The model also defines the rate of change of the dimensionless concentration terms with the ordinary differential equations (ODE).

2. EXPERIMENTAL SET UPS, PROCEDURES AND PERFORMANCE AND THERMAL BEHAVIOR OF NCR18650B CYLINDRICAL LI-ION BATTERIES

The Energy Systems Laboratory in the Department of Mechanical Engineering involves the following devices and equipment to investigate the performance of Li-ion batteries.

- Maccor 4300 Battery Test System.
- Nüve FN300 Oven.
- NCR 18650b Cylindrical Li-ion batteries.
- T, K, and J Type Thermocouples.
- NI-DAQ (National Instrument Data Acquisition) card.
- Santech 33010 Triple Output Adjustable DC Power Supply.
- Plexiglass stand.
- Film Heaters.

The laboratory allows the investigation of the thermal and electrical behaviors of the Li-ion batteries during the standard charge and discharge processes. Apart from that, thermal abuse tests can be performed in two different ways.

- by heating the battery with a temperature-adjustable oven.
- by heating the battery with a film heater.

2.1. Experimental Procedure for Standard Charging/Discharging Processes

The testing system can measure the surface temperature and terminal voltage value of the cell at given current inputs during charging or discharging processes.

Figure 2.1 shows the battery testing system used to investigate the electrical and thermal behaviors of Li-ion batteries by applying simulated loads under computer control. Maccor 4300 battery test system was used to produce the simulated

loads. The cell's voltage is limited to 2.5 V for all discharging processes, considering the manufacturer's specifications presented in Table 2.1.

Table 2.1. Panasonic NCR18650b Li-ion Battery Specifications [89].

Property	Value
Minimum Rated capacity at 20°C	3200 mAh
Minimum Capacity at 25°C	3250 mAh
Nominal Voltage	3.6 V
Gravimetric Energy Density	676 Wh/l
Volumetric Energy Density	243 Wh/kg
Minimum Cell Voltage	2.5 V
Maximum Cell Voltage	4.2 V

The cell is connected from the negative and positive poles to the channel of the battery testing device in order to track the voltage variation of the cell during charging or discharging processes. Figure 2.1 also presents the T-type thermocouple located in the center of the Li-ion cell. The test stand was uniquely designed with plexiglass material to test 4 cylindrical Li-ion batteries simultaneously. Besides, the thermocouples are connected to the NI-DAQ device to measure the temperature variations on cells' surface. An exclusive clamp mechanism minimizes the contact resistance between the curved battery surface and the thermocouple tip.

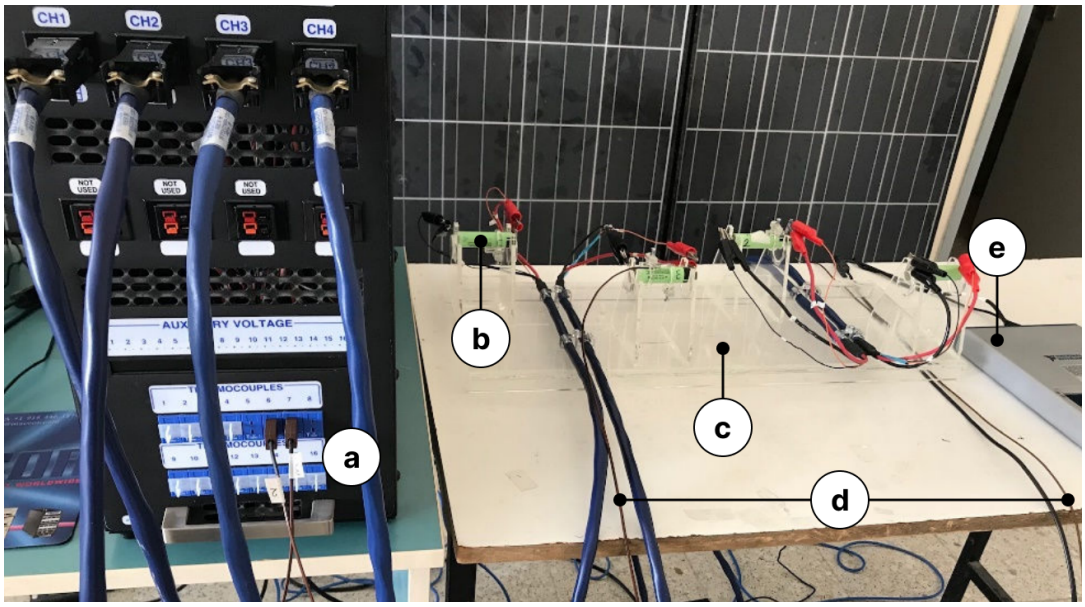

Figure 2.1. Battery testing system: a) Maccor 4300. b) Li-ion cell. c) Plexiglass stand. d) T-type thermocouples. e) NI DAQ card.

2.1.1. Experimental Uncertainty Calculations

Maccor test system has an accuracy of ±0.02% Full-Scale Range (FSR), which corresponds to a maximum ±3mV accuracy during the voltage measurements since the test system voltage is limited to 15 V. On the other hand, temperature measurements were performed using T-type thermocouples, analog-to-digital conversion was carried out with NI-DAQ card, and LabVIEW software was used for the control of the DAQ process. The sampling frequency in the temperature measurements was set as 2000 Hz. The mean value of 2000 data was used as the temperature value for a given time instant. The thermocouples were calibrated before each measurement by adequately adjusting the cold junction compensation (CJC) value. The bias error of the temperature measurements was ±1°C considering the T-type thermocouple characteristics.

The random voltage and temperature errors were calculated for a 95% confidence interval by repeating the 1C rate discharging experiments for four batteries at the same operating conditions. As the number of samples is less than

30, the t-distribution method was applied to evaluate the random error at each DoD value. The standard deviation of the samples was evaluated using Eq. (2.1),

$$SD = \sqrt{\frac{((X_1 - \overline{X})^2 + (X_2 - \overline{X})^2 + (X_3 - \overline{X})^2 + (X_4 - \overline{X})^2)}{df}} \quad (2.1)$$

where X values represent the voltage or temperature measurements at that SoC, $\overline{X}$ is the mean value, and df shows the degrees of freedom as,

$$df = n_s - 1 \quad (2.2)$$

where n_s indicates the number of samples. Then the random error can be calculated using Eq. (2.3).

$$P_x = \frac{t_{3,95} * SD}{2} \quad (2.3)$$

In this equation, the multiplier $t_{3,95}$ can be read from the t-table for 3 degrees of freedom at 0.05 level of significance as 3.182. As a result, combining the random and bias errors, the uncertainty of the voltage and temperature measurements at each DoD value was determined, as presented in Figure 2.2.

The presented figures indicate the variation in the uncertainty of the voltage and temperature measurements with DoD. During the voltage measurements, the uncertainty is more pronounced around the 0 and 1 DoD. Apart from that, the uncertainty of the temperature measurements tended to increase during the discharging process and reached the highest value at 1 DoD.

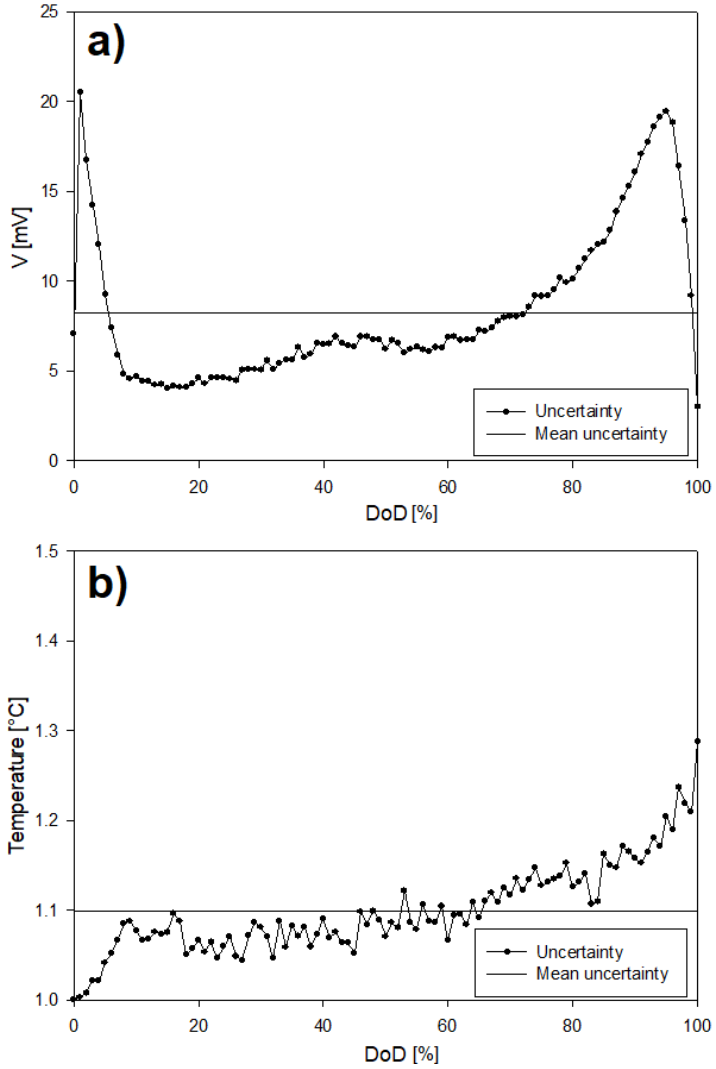

Figure 2.2. Voltage (a) and temperature (b) uncertainty values at various DoD values.

Maximum and mean uncertainty values of the voltage and temperature values are also stated in Table 2.2.

Table 2.2. Mean and maximum uncertainty values of the voltage and temperature measurements.

Uncertainty	Voltage [mV]	Temperature [°C]
Maximum	±20.5	±1.29
Mean	±8.26	±1.1

2.2. Experimental Procedure for Thermal Abuse Tests

2.2.1. Film Heater Test Set-up

A film heater was used in such geometry to almost entirely cover the cell's lateral area in order to heat the cell directly from the surface. A power supply was used to sustain the required voltage and current values. Temperature measurement was carried out by a T-type thermocouple connected to the NI DAQ device. As a precaution, the battery was placed inside an open-top wire mesh without touching anywhere. There was also a second wire mesh that covered the whole system to provide safety. The experimental set-up is illustrated in the figure below.

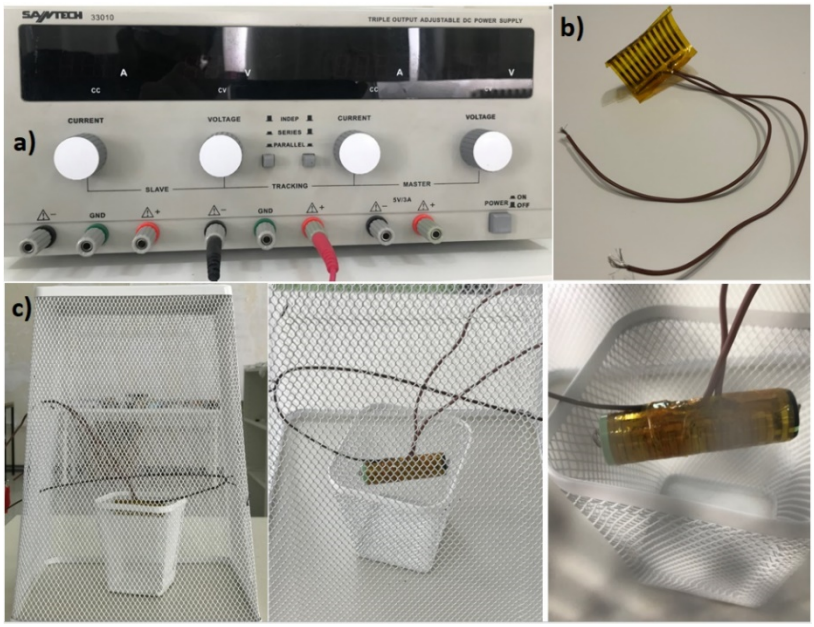

Figure 2.3. Set-up for abuse experiments: a) Power supply, b) Thin film heater 6x6 cm, c) wire mesh.

2.2.2. Oven Test Set-up

A natural convection oven shown in Figure 2.4c and a fridge were used to simulate the low and high-temperature ambient conditions. Figure 2.4 shows the components of the battery testing system and their connection to each other. The battery is placed inside the oven before the experiment. Before the placement,

necessary connections between the Maccor and the NI-DAQ device were made, as seen in Figure 2.4b.

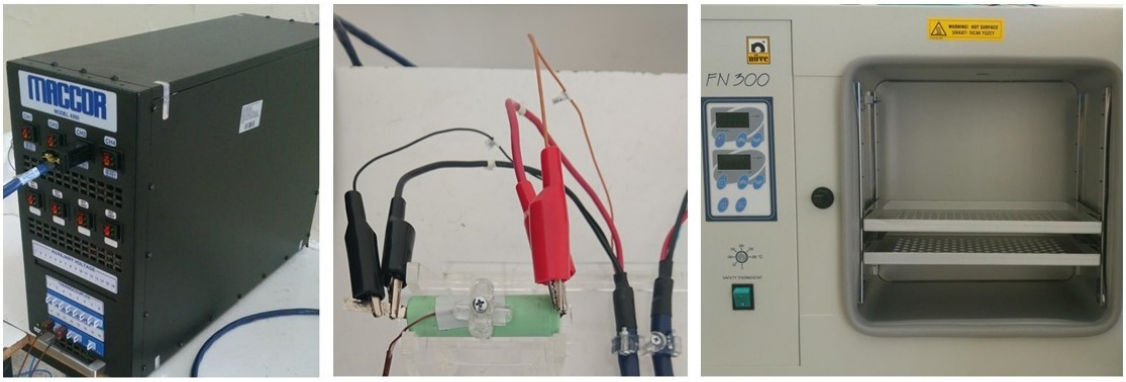

(a) (b) (c)

Figure 2.4. Battery testing system: (a) Maccor 4300 computer-controlled battery testing device, (b) Li-ion battery, (c) a natural convection oven.

2.3. Experimental Determination of the Li-ion Cell Parameters

2.3.1. Determination of the OCV

OCV value of the cell defines the potential difference between the anode and cathode terminals when there is no flowing current. It represents the maximum available voltage value of the cell and varies according to the battery's SoC. In this study, OCV was measured for various DoD values of an NCR18650b Li-ion cell at 20°C, as given in Figure 2.5.

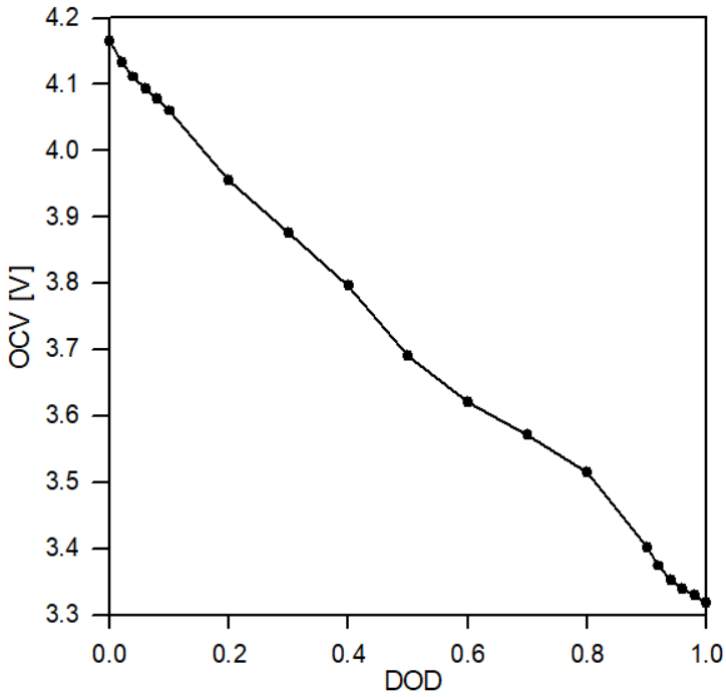

Figure 2.5. Variation of OCV with DoD during 1C discharging process at 20°C.

At first, the measurements were done in 0.1 DoD intervals. However, the OCV of the cell should have been measured more precisely at the beginning and the end of the discharging process due to sudden changes in terminal voltage values. Therefore, the corresponding OCV values were measured in each 0.02 DoD value for the first and the last 0.1 DoD intervals. There was a 5-hour break after each measurement to achieve chemical stabilization within the cell. The results are compared with the previous studies [8, 43] and found to be reasonably consistent.

Once the OCV values at a reference temperature are obtained, the results can be extended for different ambient temperatures using the entropic heat term. The entropic heat denotes the change in OCV value with respect to temperature. Recent studies show that an increase or decrease in ambient temperature does not change the battery's OCV value in a certain pattern. Hence, the studies regarding the OCV measurements at different ambient and charge conditions are still under investigation [43, 90].

2.3.2. Determination of the Specific Heat

The specific heat value of the battery was experimentally determined using the lumped transient model (LTM). LTM approach employs the general heat diffusion equation by using the corresponding boundary condition, neglecting the heat generation term. First, a cylindrical aluminum specimen was manufactured in a similar geometry to the Li-ion cell. The properties of the specimen are given in Table 2.3.

Table 2.3. Properties of the Aluminum Specimen.

Properties	**Amount**	**Reference**
Mass	0.046 kg	Measured
Length	0.065 m	Measured
Radius	0.0092 m	Measured
Density	2662.8 kg/m^3	Calculated
Specific Heat	875 J/kgK	[91]
Conductive Heat Transfer Coefficient	177 W/mK	[91]
Area	0.00429 m^2	Calculated
Volume	0.0000173 m^3	Calculated

Then both rods (aluminum rod and battery) were placed in an oven until they reached a specific surface temperature of around 50°C. The rods were then removed from the oven to be cooled down to ambient temperature. The LTM model of aluminum cooling was verified with its experimental data. This model can predict the cooling behavior of the aluminum block with a maximum error of 10.1%. Then the verified model was used to simulate battery cooling. The only unknown value in the model is the cell's specific heat. It was calculated by setting

different values for specific heat in the general heat conservation equation to fit the experimental and the model results well. As a result, the constant specific heat value of the battery was determined as 0.75 kJ/kg K. On the other hand, the maximum temperature estimation error was around 18.1% for Li-ion battery cooling. The experimental and predicted transient profiles that show the cooling behavior of the aluminum block and the Li-ion cell are presented in Figure 2.6.

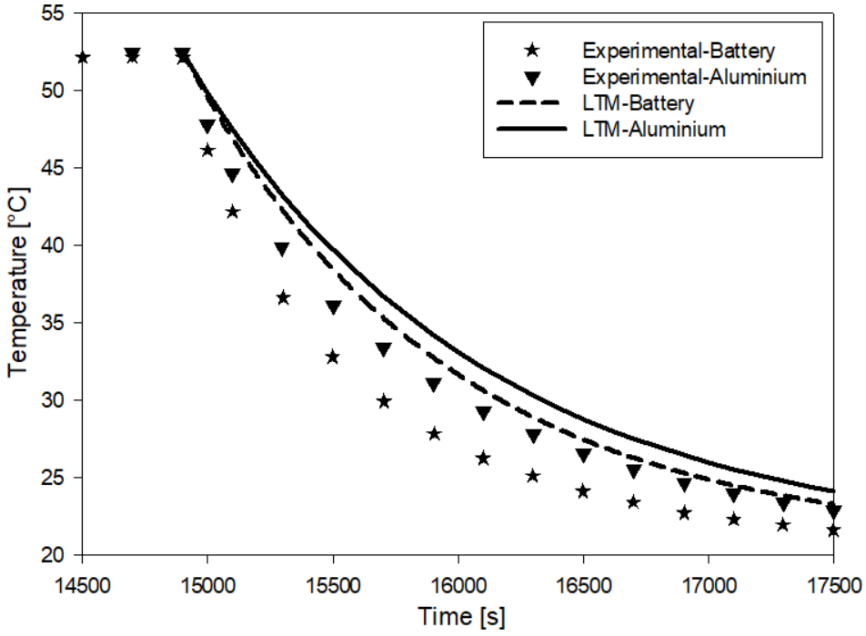

Figure 2.6. Cooling behavior of the aluminum specimen and the Li-ion battery cell at 20.6°C mean ambient temperature.

2.3.3. Determination of the Internal Resistance

Experiments were conducted to observe and examine the impacts of the various conditions on the cell's internal resistance, such as discharge rate and ambient temperature. Each experiment was conducted with NCR18650b Panasonic cells with no aging conditions, so the capacities of the cells preserve the nominal value of 3.25 mAh.

The cell internal resistance is one of the main characteristic properties, so it should be appropriately specified. It was calculated for 19 different DoD points using Eqs. (1.2) and (1.3) during the 0.5, 1, and 1.5C rate discharging processes

at 0, 20, and 50°C ambient temperatures. The results are presented in Figure 2.7. Note that in these calculations, the OCV value of the cell was assumed constant at each ambient condition.

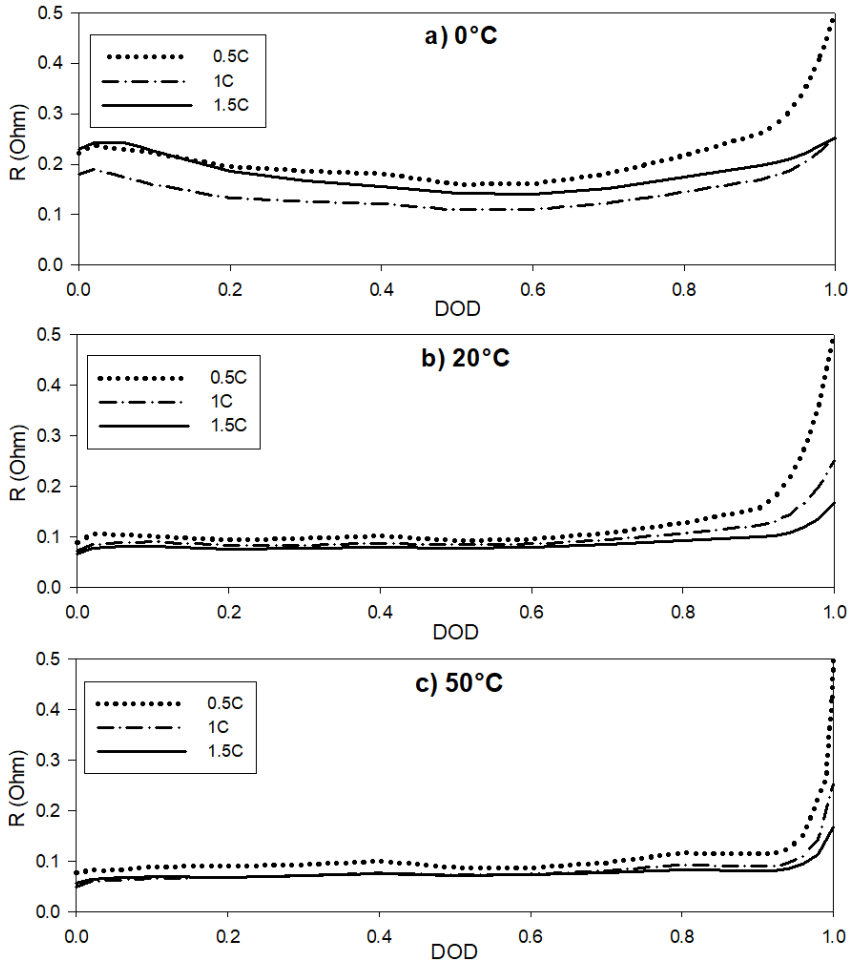

Figure 2.7. Variation of the internal resistance of the cell with DoD for various C rates and ambient temperatures.

Test results primarily validate the impacts of the ambient temperature since the resistance increases as the ambient temperature decreases. This is expected because the activity of the Li-ions is challenged more under low operating temperatures. Besides, at 0°C operating conditions, increasing cell temperature decreases the internal resistance at the beginning of the discharging process, but the cell has higher internal resistance during the last stage of the discharge. The common argument is that the total internal resistance increases as the DoD value

reaches 1 in each case. The movement of Li-ions becomes more difficult as the Li-ions pass since there is limited space left for the last ions.

Experiments also indicate that the discharge rate enormously affects the cell's resistance. Regardless of the temperature, the cell has the highest resistance for 0.5C rate, and it dramatically increases towards the end of the discharging process. Besides, disregarding the 0°C case, an increase in discharge rate causes a lower internal resistance value. In addition, independently of the operation conditions, the cell internal resistance is almost stable in a wide range between 0 and 0.8 DoD value.

2.4. Standard Charge and Discharge Tests

Constant current charging or discharging processes are named galvanostatic procedures. One of the fundamental concepts that were followed within the scope of this thesis is to observe and investigate the galvanostatic charge and discharge processes of a Li-ion cell by developing a model that estimates its thermal and electrical characteristics. In the following subsection, the charging behavior of the Li-ion batteries will be discussed based on experimental results obtained under different operating conditions.

2.4.1. Standard Charge Tests

Charging procedure involves serial constant current and constant voltage processes. Several experiments were conducted to observe the thermal and electrical performances of the charging battery at different operating conditions. Figure 2.8 illustrates the current and voltage variations of 0.5, 1, and 1.5C rate charging processes at -5, 25, and 52°C ambient temperatures.

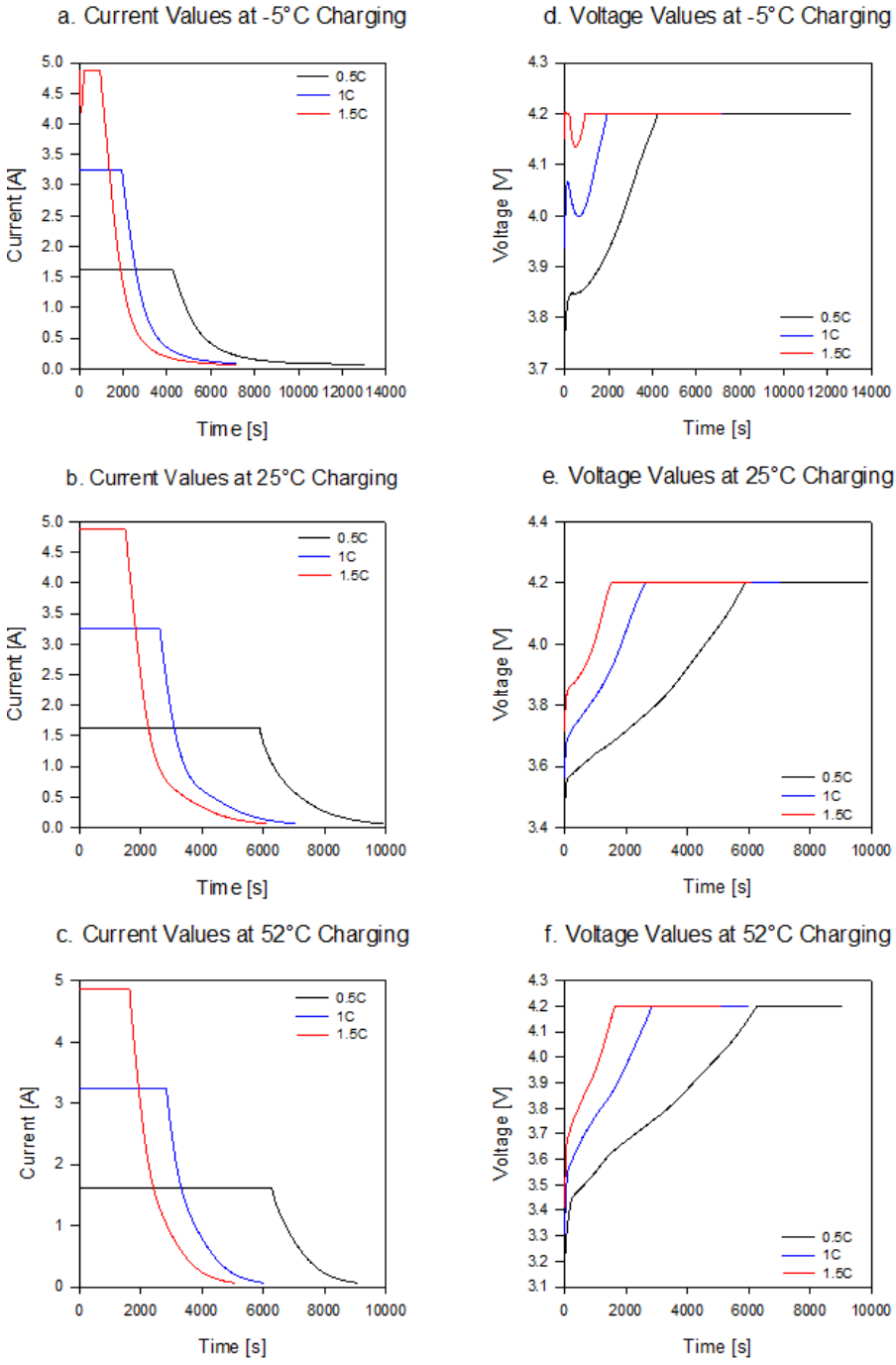

Figure 2.8. Current and voltage values of a charging cell at various operating conditions.

According to the manufacturer's instructions, NCR18650b cells are charged at a certain current value up to the terminal voltage is 4.2 V. The voltage is then held constant, and the charging process continues as the cell current reduces to 0.065 mA. The suggested maximum charging current is 0.5C rate. Besides, the

appropriate operating temperature range for the charging process is determined between 0-40°C. In these experiments, optimum temperature and voltage limits were intentionally exceeded to observe the electrical and thermal characteristics of a charging cell.

It is apparent from the given figures that the charging in cold ambient lasts longer than expected. In each charging condition, the time the battery is charged increases as the ambient temperature decreases, which can be explained by the activation of Li-ions. The movement capability of the ion is directly related to the operating temperature. In cold ambient, Li-ions are relatively less active, so it is challenging for the Li ions to travel between the electrodes. Therefore, in cold ambient, entire constant current-constant voltage charging processes may take an extended time compared to the relatively higher operating temperatures.

It can be deduced from the given figure that as the ambient temperature decreases, it is faster to reach the constant voltage process. In other words, constant current charging duration reduces as the ambient temperature decreases.

Most of the current and voltage profiles follow the expected trend but Figures 2.8a and 2.8d. These figures display a minor deviation during the charging at 1 and 1.5C rates and -5°C ambient.

Figure 2.9 shows the surface temperature profiles of the 0.5, 1, and 1.5C rate charging cells at -5, 25, and 52°C ambient temperatures. Common results of these experiments reveal that the cell's temperature increases throughout the charging process at a constant current and decreases during the charging process at a constant voltage. The charging cell's thermal behavior depends on the applied current and ambient temperature. As the applied current increases, the cell's temperature increases as well. In addition, the results also denote that the temperature difference increases as the operating temperature decreases.

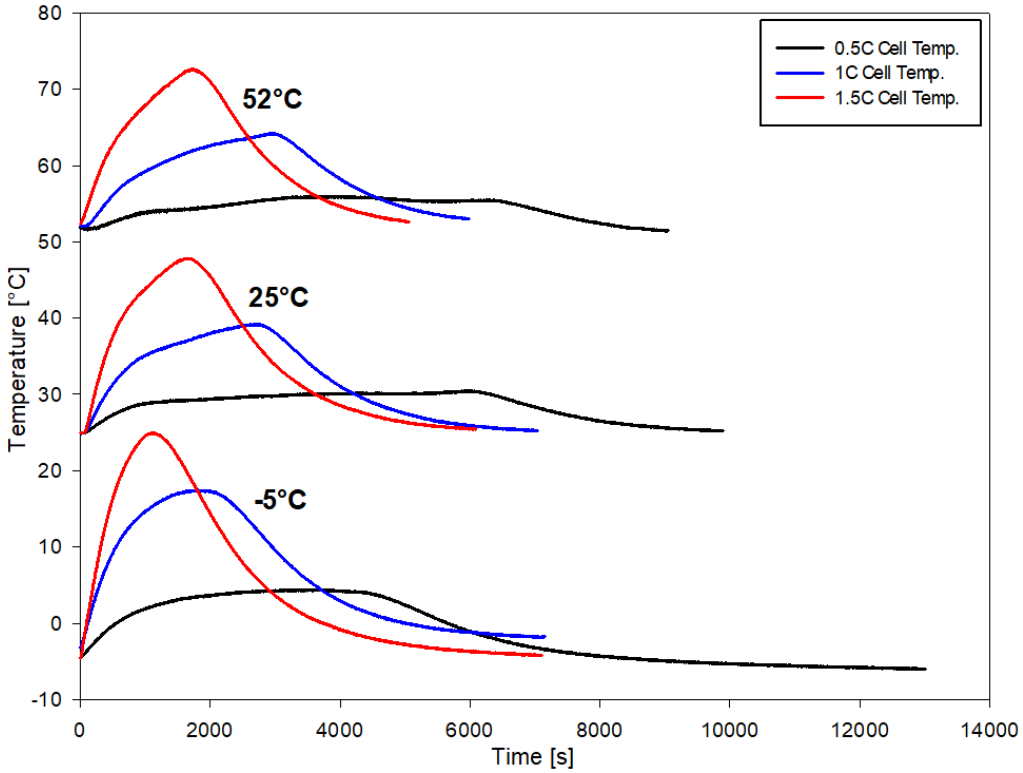

Figure 2.9. Surface temperatures of the 0.5, 1, and 1.5C rate charging cell at -5, 25, and 52°C ambient temperatures.

Temperature profiles follow the same trend during each experiment. However, the increase of cell temperature is more pronounced at -5°C charging process since the internal resistance increases at cold ambient temperatures.

2.4.2. Standard Discharge Tests

The thermal and electrical performances of the Li-ion cells are strongly influenced by the rate of discharge current and the operating temperature, so a series of experiments were conducted. Figure 2.10 shows the experimental voltage variation of the cells during various discharging processes at 0-20-50°C.

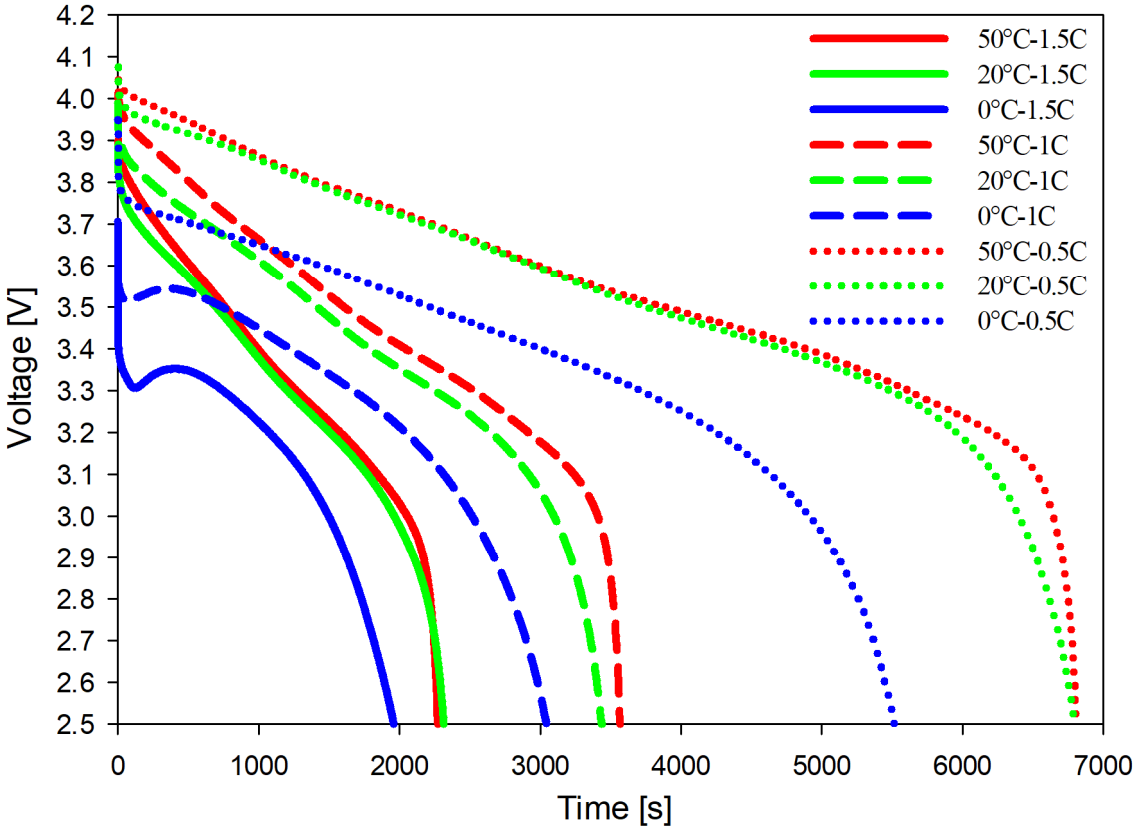

Figure 2.10. Voltage variations during various discharging conditions and operating temperatures.

Once the current is applied, the cell has a sudden voltage drop. Around this region, activation overpotential dominates. Subsequently, the cell voltage varies almost linearly toward the end of the discharge. The ohmic overpotential is effective in this part. Finally, in the last part of the discharging process, the battery voltage sharply decreases in a very short time, where the concentration overpotential is the most dominant loss.

The voltage variation during the same discharging process differs with respect to the operating temperature of the cell. The voltage variation seems close to each other at 20 and 50°C. However, the battery capacity considerably decreases at cold ambient (up to 23% of the rated capacity depending on the discharging C rate), most possibly due to the weak ionic conductivity within the cell. This also reduces the discharging time since the voltage reaches the limited voltage value of the cell early.

The temperature variation of the 0.5, 1, 1.5C rate discharging cells at 0, 20, and 50°C are presented in Figure 2.11.

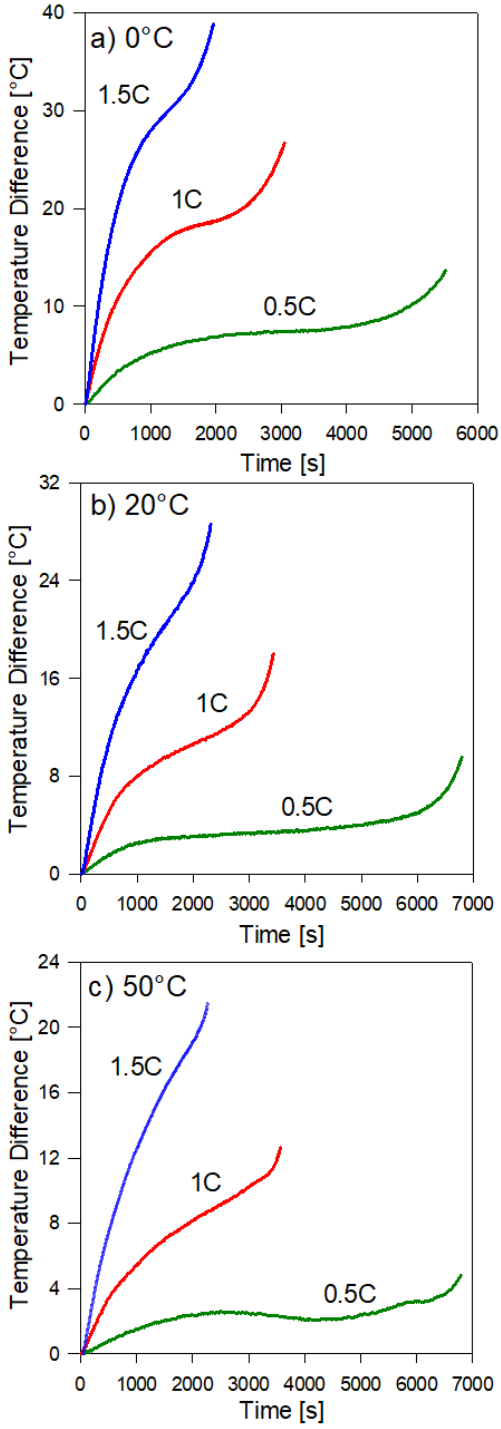

Figure 2.11. The temperature difference between the ambient and the cell surface during 0.5-1-1.5C rate discharging processes at a) 0°C, b) 20°C, c) 50°C.

Figure 2.11 shows that the operating temperature considerably affects the cell's thermal behavior. The cell’s temperature increases sharper as the voltage variation instantly drops through the end of the discharging processes in each case.

As expected, the cell temperature increase is more pronounced at lower temperatures and high discharge rates. Under the same discharge rate, the cell warms more at 0°C due to higher internal resistance. When the cell temperature reaches the optimum operating temperature, the slope of the temperature rise decreases, and the cell behaves as usual in terms of thermal characteristics.

The temperature increase is lower at 50°C operating temperature. Apart from that, the cell capacity is higher at elevated temperatures. However, the operation of the battery under high temperatures is a factor that will adversely affect its health and increase the possibility of TR.

3. LUMPED BATTERY MODEL

(The results of this chapter are published in Heat Transfer Engineering, vol.43, no.3-5, 314-325)

3.1. Lumped Battery Model

Lumped models are developed to reduce the computational cost by neglecting the variation of the cell temperature. Utilizing a materially lumped model simplifies the electrochemical calculations as an alternative approach. In this lumped model, the positive and negative electrode, separator, and electrolyte are represented by a uniform material with effective properties. Therefore, the model can be implemented by applying a reduced number of input parameters. In this study, the lumped battery model was developed using COMSOL Multiphysics software.

An axisymmetric 2-D lumped model was developed, coupling the heat transfer and the lumped battery interfaces to predict the cell's surface temperature during discharge. Figure 3.1 displays the 2-D and 3-D model geometry of a cylindrical Li-ion cell, which consists of a mandrel, active material, and a shell.

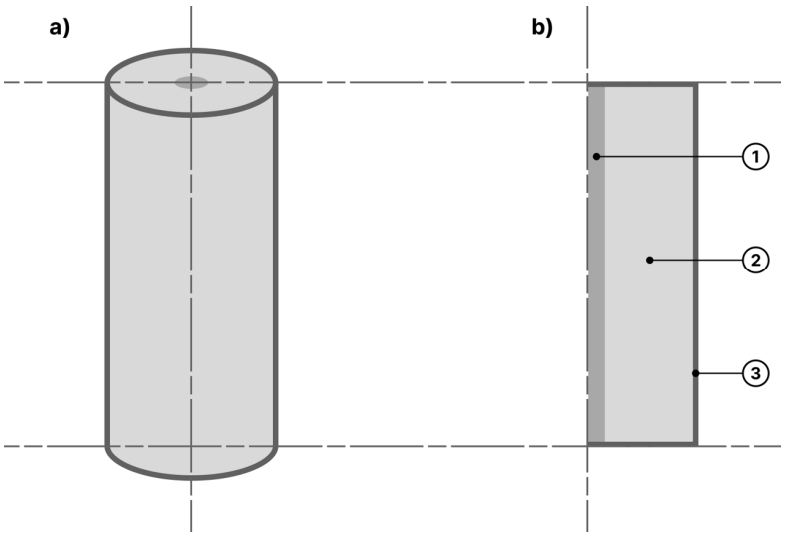

Figure 3.1. a) Li-ion cell in 3-D, b) 2-D model geometry of the Li-ion cell.1. Mandrel. 2. Active material. 3. Shell.

The active material is placed around a mandrel and represents the spiral layers that involve a positive electrode, a negative electrode, a separator as an electrical insulator, and the electrolyte solution. Besides, at the outmost layer, a shell covers these components. The lumped model is developed using assumed input parameters or obtained by experimental methods. Table 3.1 presents the parameters that were utilized in the lumped model.

Table 3.1. Lumped model parameters.

Material	Value	Reference
Thickness of the battery shell	4e-4 m	[43]
Battery radius	9e-3 m	Measured
Battery height	65e-3 m	Measured
Cell thermal conductivity, angular	28.05 W/mK	[43]
Cell thermal conductivity, radial	3 W/mK	[43]
Battery density	2782 kg/m^3	Calculated
Cell heat capacity	750 J/kgK	Measured
Nominal cell capacity	3.25 Ah	Measured
Dimensionless charge exchange current	0.8	[92]
Diffusion time constant	1000 s	[92]
Initial state of charge	1	Measured
Heat capacity of the shell	875 J/kgK	[92]
Shell density	2059 kg/m^3	[92]
Shell thermal conductivity	0.638 W/mK	[92]

The developed lumped model uses the constant internal resistance approach and the variable internal resistance approach. Both methods have some advantages and disadvantages, which will be discussed in the following parts in detail.

3.1.1. State of Charge and Voltage Predictions

In the lumped model the SoC variation of the discharging cell is calculated using Eq. (3.1),

$$\frac{\partial SoC}{\partial t} = \frac{I_c}{Q_{c,0}} \tag{3.1}$$

where SoC denotes the average state of charge value of the cell, t is the time, I_c is the applied current to the cell, and $Q_{c,0}$ is the nominal capacity of the cell [92]. This relation indicates that the SoC value is linearly proportional to the current of the cell during galvanostatic discharging processes. On the other hand, the charging behavior of the cell cannot be predicted with this equation since the charging process follows a constant current-constant voltage phase.

The lumped model uses the measured OCV values with the related overpotential terms to accurately predict the voltage variation of the cell during the discharging process. The following equation defines the terminal voltage variation of the cell,

$$V_c = OCV(SoC,T) + \eta_{ohmic} + \eta_{conc} + \eta_{act} \tag{3.2}$$

where V_c is the voltage value of the cell, OCV is the open circuit voltage value of the cell, and η_{ohmic}, η_{conc}, and η_{act} indicate the ohmic, concentration and activation overpotentials, respectively. In Eq. (3.2), the first term on the right hand side represents the OCV of the cell as a function of both SoC and the cell temperature. The effects of ambient temperature on the OCV measurement is calculated using Eq. (3.3).

$$OCV(SoC,T) = OCV_{ref}(SoC) + (T - T_{ref})\frac{\partial OCV(SoC,T)}{\partial T} \tag{3.3}$$

In this equation, $OCV_{ref}(SoC)$ is the open circuit voltage at a reference temperature T_{ref}, T is the instantaneous temperature value of the cell, and $\frac{\partial OCV(SoC,T)}{\partial T}$ represents the entropic term that shows the variation of OCV with respect to temperature. In this study, $OCV_{ref}(SoC)$ terms were measured for various depth of discharge (DoD) values at 20°C reference temperature and were already given in Chapter 2.

The entropic term normally varies with the SoC, discharge rate, and operating temperature. In this study, the entropic term is assumed independent from the state of charge variation. It is taken only as a function of the discharge rate and the operating temperature. The entropic term can be potentially determined by measuring the OCV values in at least two different ambient conditions [43]. However, since the variation in OCV with temperature was too small to be reliably determined by the existing testing system, it was assumed to be a model-fitting parameter.

For each discharge rate and operating temperature, a suitable value for the entropic term - which resulted in a reasonable match between experimental and model surface temperature values - was determined. The results of this so-called “entropic term mapping procedure” are presented in Table 3.2. This mapping procedure was followed for two lumped models that use variable and internal resistance approaches. The results are valid for simulating the discharge processing in an operating temperature range of 0 to 50°C.

Table 3.2. Entropic term mapping results.

Entropic Term mV/K	**0°C**	**20°C**	**50°C**
0.5C	0.58[a]/0.46[b]	0.34 [a]/0.34[b]	0.3[a]/0.26[b]
1C	0.6[a]/0.49[b]	0.53 [a]/0.54[b]	0.42[a]/0.32[b]
1.5C	0.8[a]/0.65[b]	0.66 [a]/0.65[b]	0.6[a]/0.45[b]

a. Entropic term mapping results for the constant internal resistance model.

b. Entropic term mapping results for the variable internal resistance model.

Overpotentials which were already presented in Chapter 1 mainly consist of ohmic, concentration, and activation overpotential terms to represent the voltage losses during the discharging processes. Ohmic overpotential can be defined as,

$$\eta_{ohmic} = \eta_{ohmic,1C} \frac{I_c}{I_{1C}} \tag{3.4}$$

where $\eta_{ohmic,1C}$ represents the ohmic losses in the cell during 1C discharging process, and I_{1C} corresponds to a current value that discharges the battery to its cut-off voltage within an hour [92]. These values are obtained experimentally for various SoC values and used as inputs to the model. The cell discharge current at 1C is obtained from Eq. (3.5),

$$I_{1C} = \frac{Q_{c,0}}{3600 \text{ secs}} \tag{3.5}$$

The nominal capacity of the Li-ion cell is 3.25 Ah and expressed by the term $Q_{c,0}$ [92]. On the other hand, in the lumped, Eq. (3.6) is used in order to evaluate the activation overpotential during the process [92].

$$\eta_{act} = \frac{2R_u T}{F} \text{asinh}\left(\frac{I_c}{2J_0 I_{1C}}\right) \tag{3.6}$$

In this equation, R_u is the universal gas constant, T is the surface temperature of the cell, F is the Faraday's constant, and J_0 is the lumped model parameter that denotes the dimensionless charge exchange current.

The voltage losses regarding the concentration overpotential may reach high values as the current density increases [93]. In the lumped model, concentration

overpotential effects were modeled based on diffusion in an idealized particle. The concentration overpotential during a charging or discharging process can be defined by Eq. (3.7) [92],

$$\eta_{conc} = OCV(SoC_{surf}, T) - OCV(SoC_a, T) \tag{3.7}$$

The surface state-of-charge SoC_{surf}, is defined at the surface of the particle. The average state-of-charge, SoC_a, is defined by integrating over the volume of the particle [92]. Eq. (3.8) presents the state of charge value at the battery surface as a boundary condition at x=1,

$$\frac{\partial SoC_{surf}}{\partial x} = \frac{\tau I_c}{N_{shape} Q_{c,0}} \tag{3.8}$$

where N_{shape} is 1 for Cartesian, 2 for cylindrical, and 3 for spherical coordinates, x is the dimensionless spatial variable, and τ is the lumped parameter that denotes the diffusion time constant [92].

3.1.2. Energy Conservation within the Cell

The general heat diffusion equation for the energy conservation is stated as,

$$\rho c_p \left(\frac{\partial T}{\partial t} + v.\nabla T\right) = \nabla.\lambda\nabla T + \dot{Q}_c \tag{3.9}$$

where, ρ is the density, c_p is the specific heat of the cell, λ is the thermal conductivity of the cell, and $\dot{Q}_c$ is the rate of heat generation per unit cell volume. If the cell components are inhomogeneous, these properties can be considered anisotropic and will have distinct values in each direction. The term representing convection is significant in batteries with flowing electrolytes, but it is neglected for stationary batteries [94]. Therefore, Eq. (3.9) is simplified to the transient heat

conduction equation. The corresponding boundary condition at the surface of the cell can be indicated as,

$$n.(\lambda \nabla T) = -h(T_{surf} - T_{surr}) - \varepsilon\sigma(T_{surf}^{4} - T_{surr}^{4}) \quad (3.10)$$

where n represents the normal component, T_{surf} denotes the surface temperature of the cell, T_{surr} states the temperature of the surrounding area, h is the convective heat transfer coefficient, ε is the emissivity, and σ is the Stefan-Boltzmann constant. The heat dissipation rate to the surroundings can be evaluated from Eq. (3.10), where the first term on the right-hand side represents the convective heat dissipation, and the second term shows the radiative heat dissipation rate.

In the lumped battery model, the heat transfer interface is defined for three solids that constitute the cell: mandrel, active battery material, and shell. At first, the energy conservation equation is applied in each part. Subsequently, Eq. (3.10) is applied at the boundary of the cell, neglecting the effects of thermal radiation. Then it is noticed that the radiation effect becomes significant as the temperature of the cell rises. Therefore, an additional heat transfer interface from the cell surface to the ambient was defined. The emissivity of the cell's surface was taken as 0.3 and 0.8 during discharging processes at 20°C and 0–50°C tests conducted in the freezer compartment and oven, respectively [69, 83].

The convective heat transfer coefficient is calculated using the Churchill-Chu correlation as stated in Eq. (3.11) [95],

$$h = \frac{\lambda}{d}\left(0.6 + \frac{0.387 Ra_d^{1/6}}{\left(1 + \left(\frac{0.559}{Pr}\right)^{9/16}\right)^{8/27}}\right)^2, \; Ra_d \leq 10^{12} \quad (3.11)$$

where d is the cylinder diameter, Ra_d is the Rayleigh number with respect to diameter, and Pr is the Prandtl number. This correlation is valid for airflow over a horizontal cylinder and is applicable over the entire range of Prandtl numbers.

A cell exposed to an electric load will generate heat due to the electrochemical reactions, phase changes, and mixing at discrete phases within the battery. The total electrochemical heat generated inside the battery is derived by the Bernardi et al. [12] applying the first law of thermodynamics around the cell control volume and is usually used in the simplified form as presented in Eq. (1.4), where the first term on the right-hand side is specified as the overpotential heat from the ohmic losses within the cell, charge-transfer overpotentials at the interface, and mass transfer limitations. The second term is entropic heat, which includes the entropic heat coefficient, the derivative of the open circuit potential with respect to temperature.

On the other hand, a similar equation, Eq. (3.12), can also be used in the lumped model to predict the heat generation rate of the cell by using the overpotential terms and the entropic heat as,

$$\dot{q}_c = I_c\left(\eta_{ohmic}+\eta_{act}+T\frac{\partial OCV(SoC_{surf},T)}{\partial T}\right)+\dot{q}_{mix} \tag{3.12}$$

where the rate of heat of mixing is expressed by the term $\dot{q}_{mix}$ and can be defined as Eq. (3.13).

$$\dot{q}_{mix} = \left(\frac{N_{shape}Q_{c,0}}{\tau}\int_0^1 \frac{\partial OCV}{\partial SoC}\frac{\partial SoC}{\partial x}\frac{\partial SoC}{\partial x}x^{N_{shape}-1}\partial x\right) \tag{3.13}$$

3.2. Lumped Battery Model Results

3.2.1. Results of the Constant Internal Resistance Model

The developed model was used to predict the electrical and thermal behavior of a discharging Li-ion cell at 0, 20, and 50°C operating temperatures. As indicated before, the model is valid between 1 and 0.2 SoC values since the cell's internal resistance can be assumed as constant in this interval.

In order to predict the surface temperature of a discharging cell, the total heat generation must be evaluated. The model uses Eq. (3.12) to specify the total heat generation within the cell during the discharging processes at 0, 20, and 50°C temperatures. The amount of generated volumetric heat during the discharging process for each operating condition can be observed in Figure 3.2.

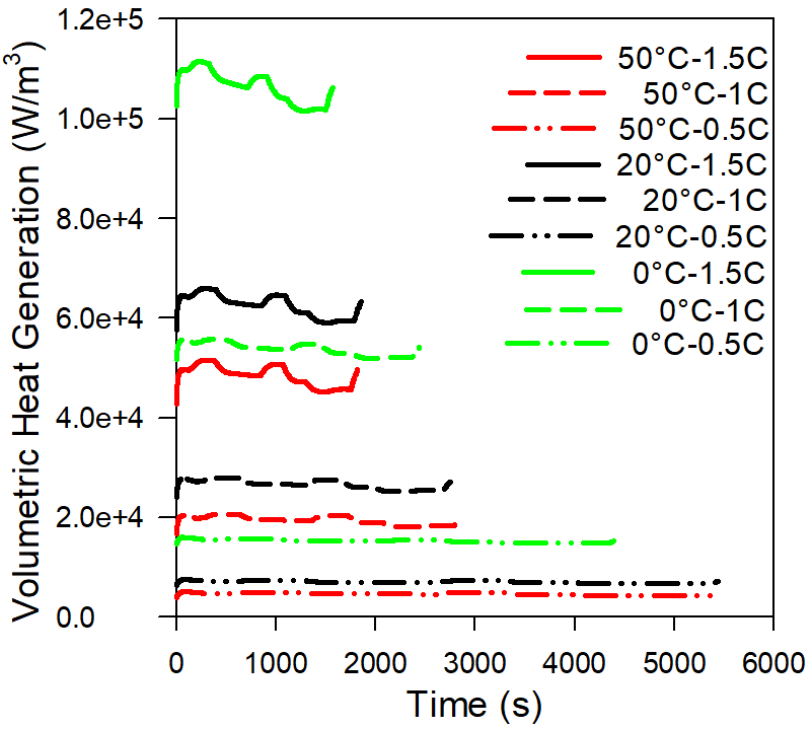

Figure 3.2. Volumetric heat generation rates during 0.5-1-1.5C rate discharging processes at various ambient temperatures in between 1-0.2 SoC interval.

Figure 3.3 shows the comparison of the model and experimental results within the range investigated. The simulation results at 0°C are slightly different from experimental results since the characteristics of the cell change at low temperatures. It is difficult to predict the thermal behavior of the cell with a constant internal resistance approach due to the fact that the internal resistance of the cell varies dramatically during the discharging processes especially at low temperatures.

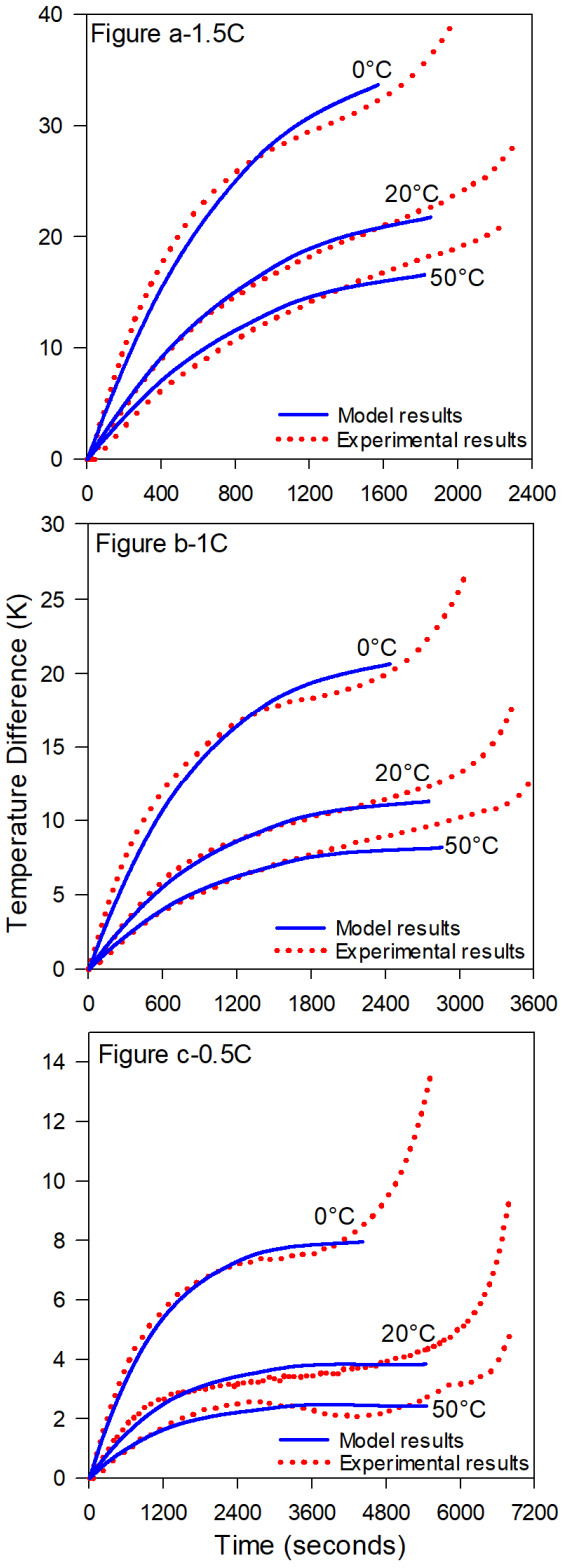

Figure 3.3. Comparison of the temperature variation of the surface of the cell at 0-20-50°C operating temperatures during a) 1.5C, b) 1C, c) 0.5C rate discharging processes using constant internal resistance approach.

The heat is dissipated from the cell by natural convection and radiation. Figure 3.4 compares the dissipated radiative heat rates with the convective heat rates during various discharge rates at 0, 20, and 50°C.

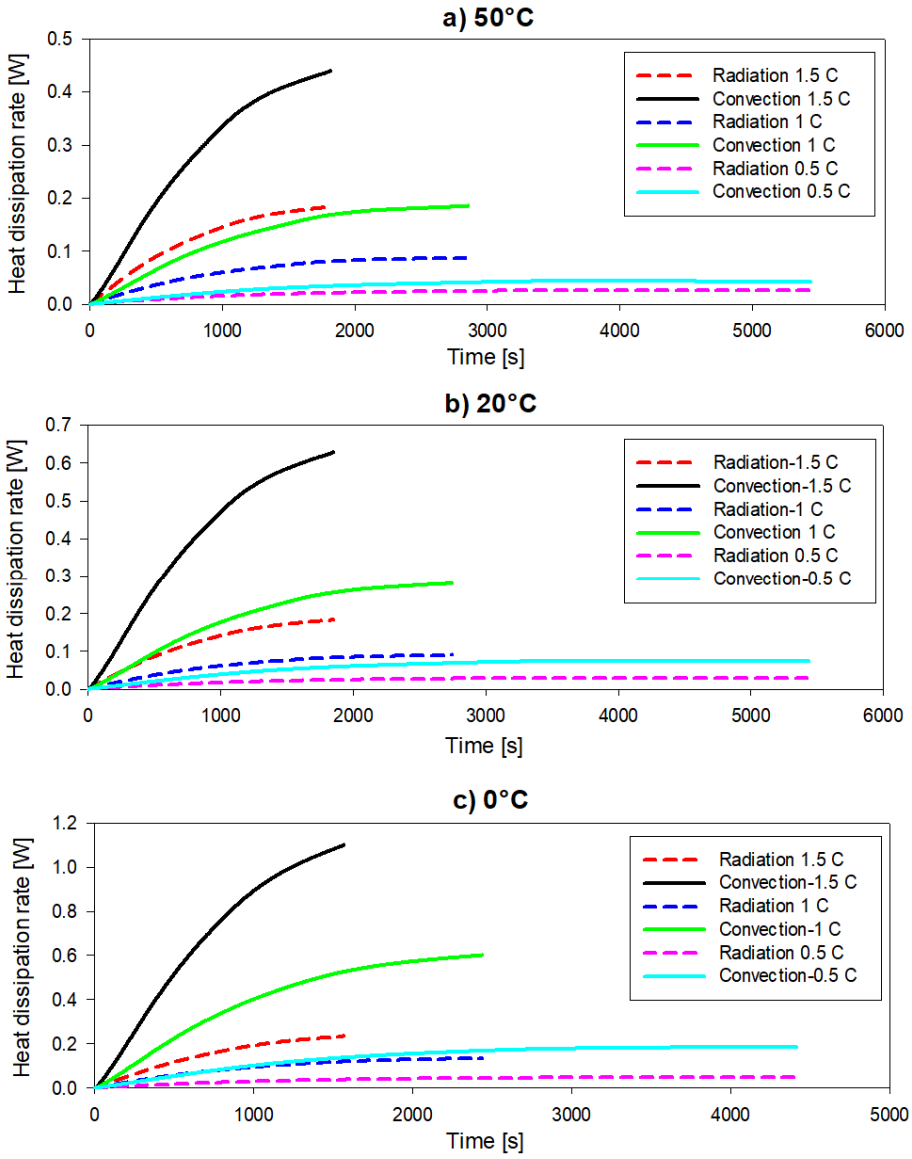

Figure 3.4. Heat dissipation rates by convection and radiation at different operating conditions.

The results denote that the effect of radiation cannot be disregarded. More heat is transferred to the ambient by radiation and natural convection as the temperature difference between the cell and the ambient increases. Besides, it can be concluded from the given plots that as the ambient temperature

decreases, more heat is dissipated by convection and radiation, as expected. Figure 3.5 indicates the variation of the convective heat transfer coefficient during 0.5-1-1.5C discharging processes at 0, 20, and 50°C.

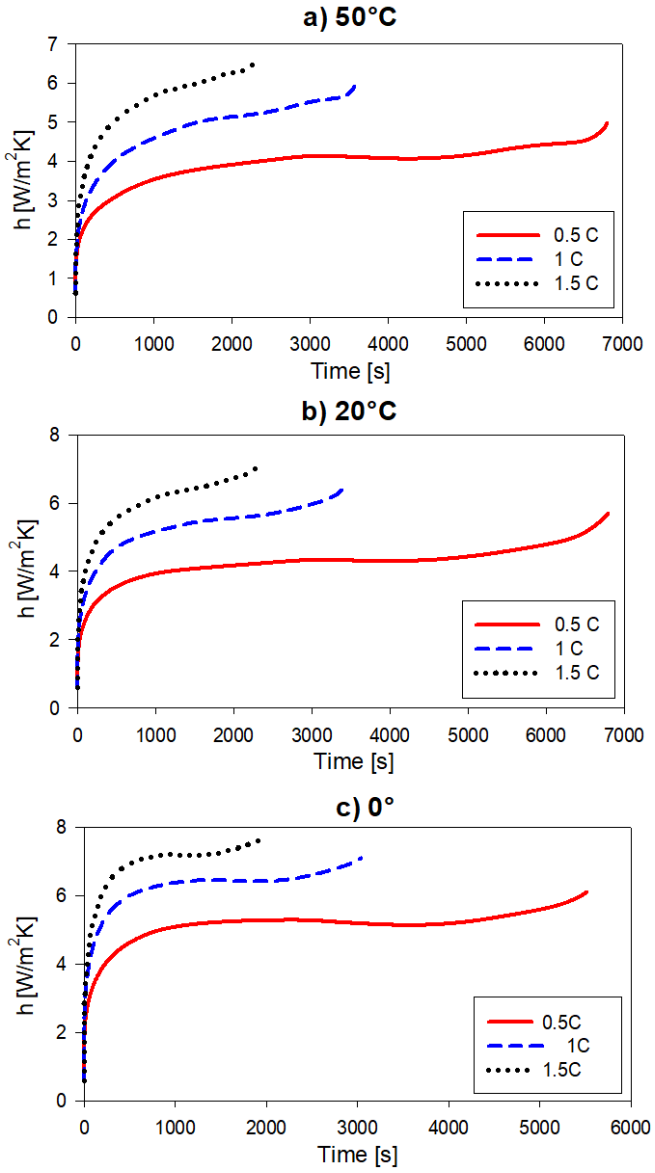

Figure 3.5. Variation of the convective heat transfer coefficients during various discharging processes and operating temperature.

The results show that a constant convective heat transfer coefficient approach is only justified at low discharge rates. However, it considerably changes at high

discharge rates, so the assumption of variable convective heat transfer coefficient is essential to predict the convective heat dissipation from the cell accurately.

3.2.2. Results of the Variable Internal Resistance Model

In this subsection, experimental results of the galvanostatic discharging Li-ion cell at different operating conditions are compared with the model results that use the variable internal resistance approach. Applying the variable internal resistances to the model gives more realistic results and enables the investigation of the thermal and electrical behaviors of the Li-ion cell in a more comprehensive way. In the lumped model, the voltage drops from the OCV values are provided by using the three overpotential terms defined earlier in Eq. (3.2). These terms cause voltage losses during the discharging so that the total voltage drop is achieved. Figure 3.6 displays the variation of these overpotential terms during the 1C rate discharging process at 20°C.

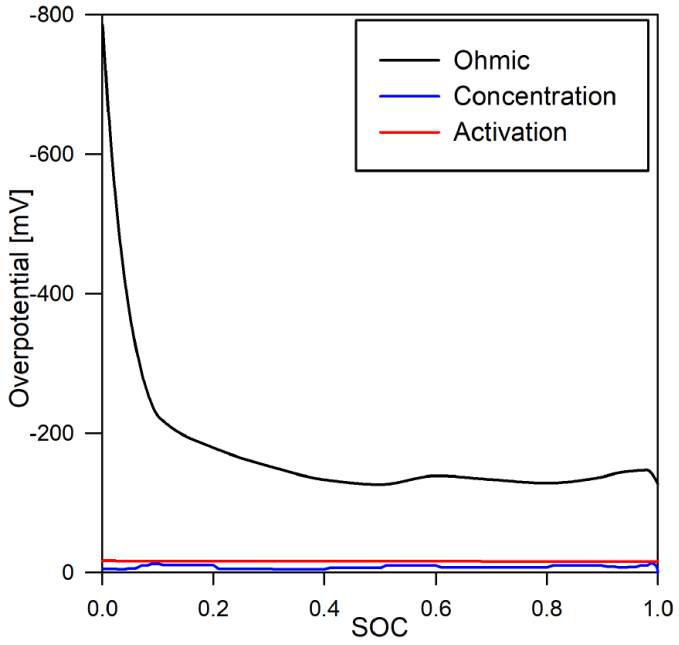

Figure 3.6. Overpotentials with respect to SOC during the 1C rate discharging at 20°C.

It can be concluded from the given plot that the ohmic cell resistance has the most significant contribution to the voltage losses during a discharge process. The total internal resistance of the cell can be calculated using the relation known as Ohm's law.

Overpotential terms were used to predict the terminal voltage values. Hence, the volumetric heat generations can be predicted using Eq. (3.12) and the constant entropic terms from Table 3.2. Figure 3.7 shows the volumetric heat generation within the cell during discharging processes at 0-20-50°C.

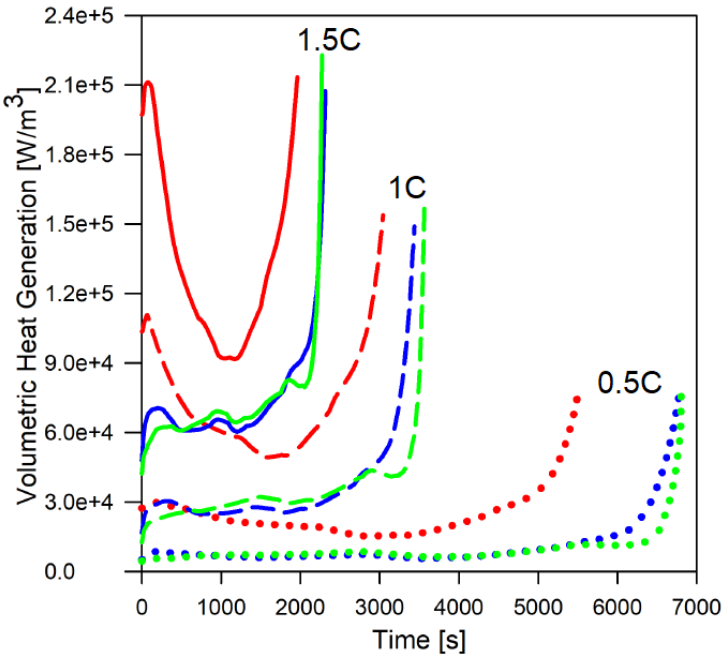

Figure 3.7. Total volumetric heat generation during 0.5-1-1.5C discharging processes at 0°C (Red), 20°C (Blue), 50°C (Green) ambient temperatures.

The area of these graphs indicates the energy generated from the cell. It can be seen from the figure that heat generation increases as the ambient temperature decreases. The main reason for this behavior is the increasing internal resistance within the cell at low temperatures. The figure also states that the discharging at higher currents causes more heat generation within the cell, as expected.

The convective and radiative heat dissipations were predicted during various discharge rates and presented in Figure 3.8.

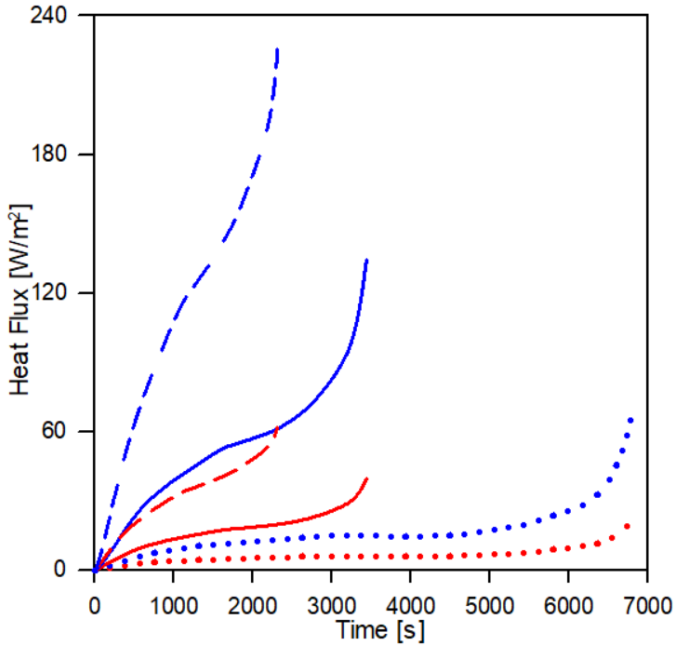

Figure 3.8. Comparison of the dissipated heat fluxes by natural convection (Blue) and radiation (Red) at 20°C. Dashed lines 1.5C, straight lines 1C, dotted lines 0.5C.

As the temperature difference between the cell and the ambient increases, radiation and natural convection transfer more heat to the ambient. The results show that the radiative effects cannot be neglected and should be taken into account along with the convective heat transfer for the variable internal resistance model as well. Although some of the generated heat is dissipated by natural convection and radiation, the heat also causes a temperature rise within the cell. Figure 3.9 compares the experimental and simulation temperature differences between the cell surface and the ambient during 0.5-1-1.5C rate discharging processes at 0-20-50°C operating conditions.

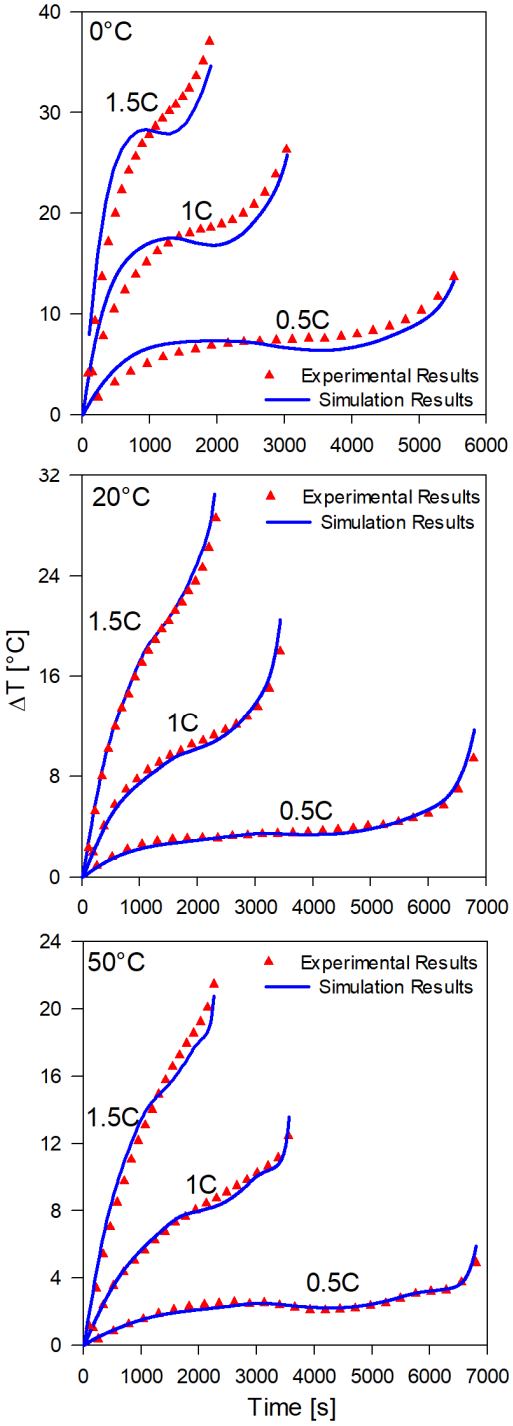

Figure 3.9. Comparison of the temperature differences between the ambient and the surface of the cell during various discharging processes at 0-20-50°C using variable internal resistance approach.

The results indicate that the operating temperature significantly influences the cell's thermal behavior. The temperature difference between the cell surface and

the ambient increases as the operating temperature decreases. It can be seen from Figure 3.9 that predicting the thermal behavior of a discharging cell is challenging in cold ambient. However, the model accurately predicts the thermal characteristics of the cell under normal operating conditions considering the root mean square error (RMSE) values and the true error percentages shown in Figure 3.10. The figure indicates that the model is more accurate at low C rates and higher operating temperatures. Since errors are evaluated regarding the temperature differences, the small temperature changes at the beginning of the discharging can cause huge true percentage errors, as obtained in almost every case.

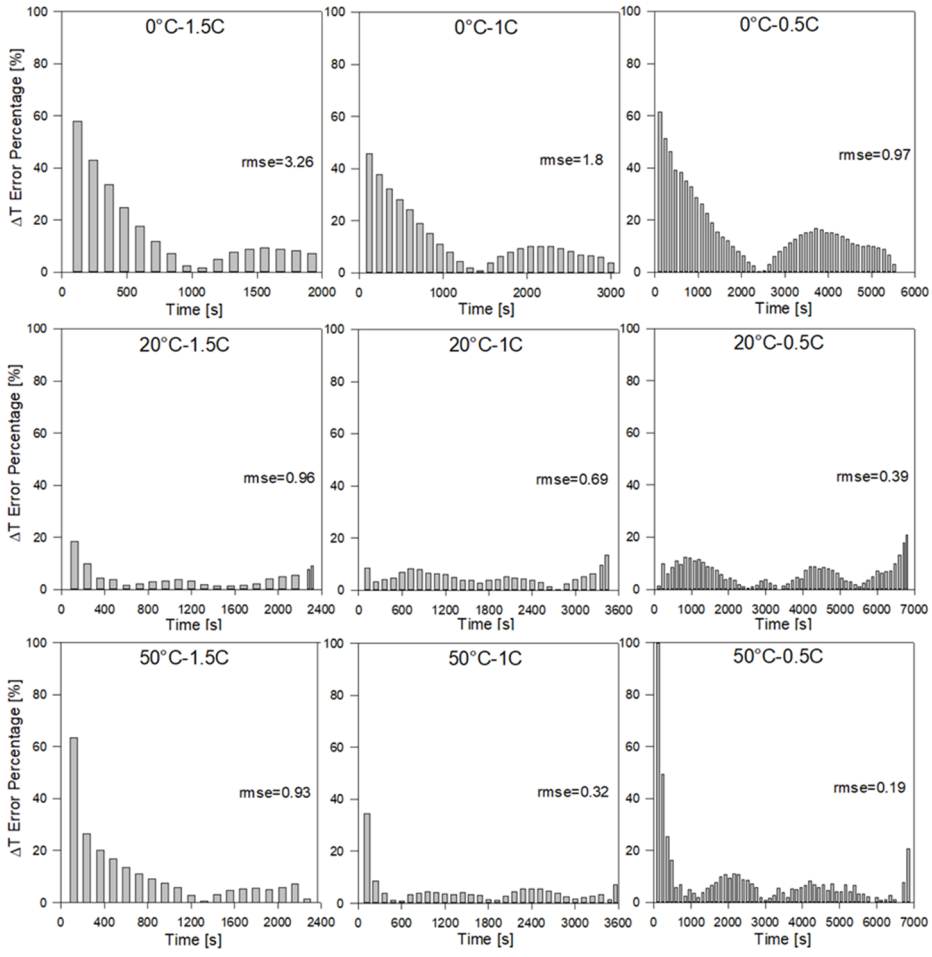

Figure 3.10. The model true percentage errors and the RMSE values of the temperature differences between the ambient and the surface of the cell during various discharging processes at 0-20-50°C.

4. ELECTROCHEMICAL-THERMAL COUPLED MODEL

4.1. Electrochemical-Thermal Model Parameters

This chapter presents the development of the 1-D electrochemical-3-D thermal coupled model in COMSOL. The electrochemical-thermal coupled model requires a large number of geometrical, electrochemical and thermal input parameters. These model parameters were evaluated with an extensive literature survey and presented in this chapter. The model parameters were selected according to a procedure summarized as follows: Priority was given to the studies that handle the same battery type, NCR18650b cylindrical Li-ion cell. Secondly, the specific type of material was considered, such as $LiNiCoAlO_2$ for cathode material or graphite for anode material, even if the battery type was not the same. Moreover, similar material properties were used in the cases when there was no available information about the original material.

4.1.1. Geometrical Parameters

In this study, a cylindrical Li-ion cell was used that consists of a graphite anode, a separator, Al and Cu current collectors, and NCA ($LiNiCoAlO_2$) cathode. The developed model involves both 3-D thermal and 1-D electrochemical model geometries. The thermal model geometry of the cell consists of a mandrel, an active battery material, and a shell, as displayed in Figure. 4.1.

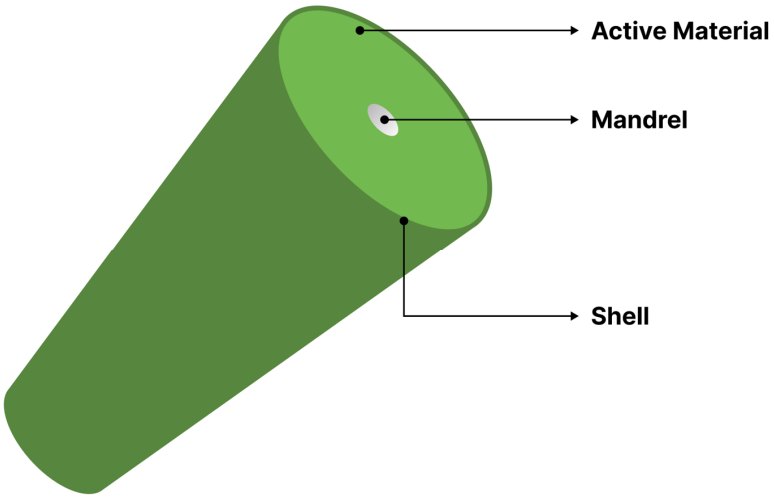

Figure 4.1. 3-D Thermal model geometry of the battery.

On the other hand, the electrochemical processes take place in the active material layer. The electrochemical model approximates the cell as a single layer in one dimension. The cell length involves a negative electrode, separator, and positive electrode. These layers within the cell were displayed in one-dimensional geometry, excluding the current collectors, as shown in Figure 4.2.

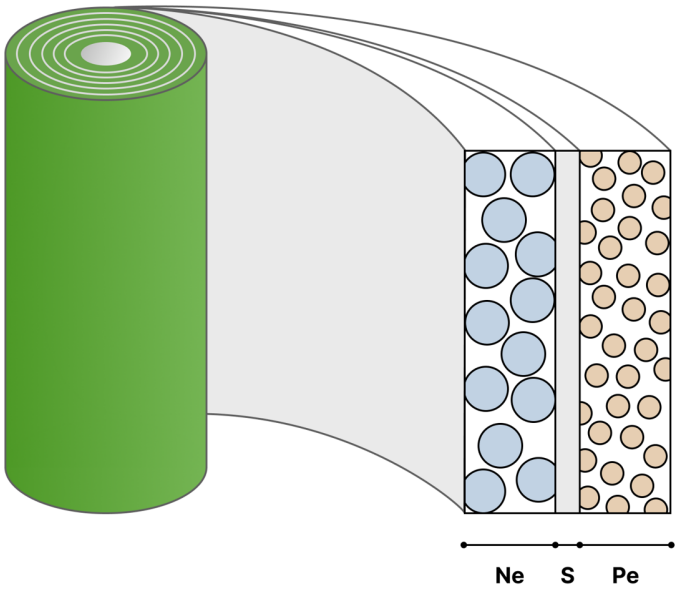

Figure 4.2. 1-D Electrochemical model geometry of the battery.

An extensive literature survey was conducted on the geometrical parameters of the Li-ion cell. These properties are presented in Table 4.1. In this table; L_{sep}, L_{necc}, L_{pecc}, L_{ne}, L_{pe}, and L_{shell} indicate the thickness of the separator, negative electrode current collector, positive electrode current collector, negative electrode, positive electrode, and shell, respectively. r_{ne}, r_{pe}, $r_{mandrel}$, and r_c are the radius of the negative electrode active particle, positive electrode active particle, mandrel, and the cell, respectively. Besides, y_c states for the height of the cylindrical cell.

Table 4.1. Geometrical parameters of NCA and other frequently used Li-ion cells.

Parameter	Value	Unit
L_{sep}	10 [96], 15 [97], 13 [98], 25 [99], 11.5 [100].	μm
L_{necc}	10 [87, 96, 97], 7.5 [100, 101], 18 [102].	μm
L_{pecc}	15 [87, 96], 14-16 [97], 30 [102].	μm
L_{ne}	110 [96], 190 [97], 205 [98], 88 [99], 61 [100], 42.6 [87], 35 [102], 73.5 [103], 243 [104].	μm
L_{pe}	125 [96], 165 [97], 158 [98], 80 [99], 55.4 [100], 32.8 [87], 35 [102], 70 [103], 50 [105].	μm
r_{ne}	2 [99], 11 [101, 106] , 12.5 [103, 107], 18 [104].	μm
r_{pe}	2 [99], 4 [100], 0.25 [58, 102], 8.5 [103], 2.5 [105, 107].	μm
$r_{mandrel}$	1.23*, 0.2 [97], 2 [92].	mm
y_c	65*.	mm
r_c	9*.	mm
L_{shell}	0.24 [96], 0.205 [97], 0.4 [43].	mm

* Measured parameters.

[99, 100, 103] $LiCoO_2$ is used as positive electrode.

[87] Mg-NCA is used as positive electrode.

[58] Prismatic cell is used.

Table 4.1 presents the geometrical parameters of NCA and other frequently used Li-ion cells in the literature. The separator thickness varies from 10 to 15 μm in the references that involve NCA electrodes [96-98]. Moreover, positive and

negative current collectors have a considerably narrow range, from 15 to 30 μm and 7.5 to 18 μm, respectively. On the other hand, the electrode lengths found in the literature are rather variable and need to be carefully selected for the model as they have significant impacts on the electrochemical modeling results. It changes from 35 to 243 μm for the negative electrode and 35 to 165 μm for the positive electrode [87, 96-100, 102-105].

The mandrel is located at the center of the cell. The material of the mandrel differs in two NCA battery applications, such as nylon and nickel foil, with a 2 and 0.2 mm radius, respectively [92, 97]. The measurements with a caliper showed that the mandrel radius of the NCR18650 cell is 1.23 mm.

The circles in Figure 1.1 display the active particles in the electrodes. Typically, these particles are not uniformly distributed and not in the shape of an exact sphere. However, the model assumes that particles are perfect spheres with an average radius value. These values range from 2 to 18 μm and 0.25 to 8.5 μm for negative and positive electrodes, respectively, from the literature [58, 99-107].

The shell consists of two parts: PVC and metal can. Since these parts are small compared to others, most of the studies use the average properties of the shell and consider these two parts as one piece. The average shell thickness values were 0.204, 0.25, and 0.4 mm from the literature for various NCA cells [43, 96, 97]. On the other hand, the effect of the shell length on the electrical and thermal characteristics of the Li-ion cell is expected as almost negligible.

4.1.2. Electrochemical Parameters

The electrochemical parameters have a significant role in electrochemical model behavior as they influence the voltage prediction of the cell during charge and discharge. Therefore, some related studies that mostly examine the NCA electrodes from the literature were investigated, the values of various parameters were presented in Table 4.2.

Table 4.2. Electrochemical parameters of NCA and other frequently used Li-on cells.

Parameters	Value	Unit
$\varepsilon_{s,ne}$	0.58 [100], 0.62 [58, 102].	-
$\varepsilon_{s,pe}$	0.5 [100], 0.482 [58, 102].	-
$\varepsilon_{l,ne}$	0.485 [99], 0.332 [100], 0.4382 [103], 0.31 [58].	-
$\varepsilon_{l,pe}$	0.385 [99], 0.330 [100], 0.29 [58, 102], 0.3 [103], 0.4 [105].	-
$\varepsilon_{l,sep}$	0.724 [99], 0.5 [100], 0.45 [103], 0.4 [58].	-
k_{ne}	5.037e-11 [99], 1.764e-11 [103], 2.334e-11 [107].	$m^{2.5}/(mol^{0.5}s)$
k_{pe}	2.334e-11 [99], 6.6667e-11 [103], 1e-10 [105, 107].	$m^{2.5}/(mol^{0.5}s)$
p_{sep}	4 [99], 1.5 [100], 2.3 [103], 3 [107].	-
p_{pe}	1.5 [100, 103], 1.928 [102], 2.89 [105].	-
p_{ne}	4.1 [103], 3.3 [100].	-
$\sigma_{s,ne}$	100 [100, 101, 103, 104, 106].	S/m
$\sigma_{s,pe}$	91 [58, 92, 102], 10 [100, 103, 105].	S/m
$D_{s,ne}$	3.9e-14 [99, 107], 5.5e-14 [100], 9e-14 [30, 101, 106], 3.17e-14 [102], Eq. (4.1)* [103], 5e-13 [104].	m^2/s
$D_{s,pe}$	1e-14 [99] , 1e-11 [100, 103], (1.11-1.63) e-15 [58, 102], Eq. (4.2)* [105, 107], (2-3)e-14 [108].	m^2/s
$c_{l,0}$	1000 [99, 103], 1200 [92, 100, 102].	mol/m^3
E_{ne}	Eq. (4.3)* [30, 109], Eq. (4.4)* [99], Eq. (4.5)* [107].	V
E_{pe}	Eq. (4.6)* [99], Eq. (4.7)* [107].	V
$c_{ref,pe}$	51554 [99], 49943 [103], 49459.2 [107].	mol/m^3
$c_{ref,ne}$	30555 [99], 31858 [103], 26389 [107].	mol/m^3

*See appendix 1 for Eqs. (4.1) to (4.7).

In Table 4.2., $\varepsilon_{s,ne}$ is the solid phase volume fraction in negative electrode, $\varepsilon_{s,pe}$ is the solid phase volume fraction in positive electrode, $\varepsilon_{l,ne}$ is the liquid phase

volume fraction in negative electrode, $\varepsilon_{l,pe}$ is the liquid phase volume fraction in positive electrode, $\varepsilon_{l,sep}$ is the liquid phase volume fraction in separator, k_{ne} and k_{pe} are the reaction rates for the negative and the positive electrode, p_{sep} and p_{pe} are the Bruggeman coefficients for the separator and the positive electrode. $\sigma_{s,ne}$ is the electrical conductivity of the negative electrode, $\sigma_{s,pe}$ is the electrical conductivity of the positive electrode, $D_{s,ne}$ is the diffusion coefficient of the negative electrode, $D_{s,pe}$ is the diffusion coefficient of the positive electrode, $c_{l,0}$ is the initial electrolyte salt concentration, E_{ne} and E_{pe} are the equilibrium potentials of the negative electrode and the positive electrode, $c_{ref,pe}$ and $c_{ref,ne}$ are the Li-ion amount within the positive and negative electrode in terms of mol/m^3, respectively.

The electrolyte appears in a liquid phase and fills the porous structure of the positive and negative electrodes. Therefore, both electrodes include liquid and solid phases. It is challenging to determine the solid and liquid phase volume fractions by experimental methods. However, the previous studies could be helpful. The investigated volume fractions vary in a very narrow range considering the NCA batteries [58, 102] and the other types of batteries [99, 100, 103].

An NCA battery's reaction rate coefficients were 1e-10 for the positive electrode and 2.334e-11 for the negative electrode [105, 107]. Some parameters are difficult to obtain since the literature lacks cylindrical NCA battery modeling applications. Therefore, it could be useful to take advantage of the exact parameters of the other type of batteries, such as $LiCoO_2$, as provided in the table above [99, 103].

The diffusion coefficients of negative and positive electrodes are mainly constant in the battery model applications [58, 99-104, 106-108]. In an application, the negative electrode diffusion coefficient is considered a function of temperature [103]. Besides, a few studies found that the diffusion coefficient of positive electrodes varies with SoC_{NCA} [105, 107]. On the other hand, the effective diffusion coefficients

can be calculated by using the Bruggeman coefficients [99, 100, 102, 103, 105, 107].

The electrical conductivity of the graphite electrode is 100 S/m in each presented research [100, 101, 103, 104, 106]. However, there are two different electrical conductivities of the NCA electrode 10 [100, 103, 105] and 91 S/m [58, 92, 102]. The equilibrium potentials of the electrodes were defined from studies [30, 107, 109]. Furthermore, similar equilibrium voltage plots used in other battery model applications can be found in studies [99] and [107].

4.1.3. Thermal Parameters

Thermal parameters of the mandrel, active material, and shell were obtained from the literature and presented in Table 4.3.

Table 4.3. Thermal parameters of NCA and other frequently used Li-ion cells.

Parameters	Value	Unit
$c_{p,mandrel}$	1700 [92, 110], 460 [111].	kJ/kgK
$c_{p,pe}$	1000 [58], 1249 [87].	kJ/kgK
$c_{p,ne}$	1000 [58], 1437.4 [112] , 881.7 [87].	kJ/kgK
$c_{p,pecc}$	897 [58], 903 [113], 896.9 [87].	kJ/kgK
$c_{p,necc}$	384 [58], 385 [113], 384.6 [87].	kJ/kgK
$c_{p,sep}$	1046 [58], 1978.16 [112], 1859.9 [87].	kJ/kgK
c_p	868.12 [114], 700 [115], 830 [116], 750*.	kJ/kgK
$c_{p,shell}$	875 [43].	kJ/kgK
$\rho_{mandrel}$	1150 [92, 110], 8890 [117].	kg/m^3
ρ_c	2782*.	kg/m^3

ρ_{shell}	2059 [43].	kg/m^3
$\lambda_{mandrel}$	0.26 [92, 110], 70 [117].	W/mK
λ_{pe}	3.4 [58], 1.58 [112], 5 [118].	W/mK
λ_{ne}	1 [30], 1.04 [112], 5 [118].	W/mK
λ_{pecc}	237 [30, 58, 87, 119], 238 [112, 113].	W/mK
λ_{necc}	401 [30, 58, 87, 119], 398 [112, 113].	W/mK
λ_{sep}	0.16 [103], 0.15 [58], 0.3344 [112].	W/mK
λ_{rad}	Eq. (4.8).	W/mK
λ_{ang}	Eq. (4.9).	W/mK
λ_{shell}	13.57 [96, 120], 0.638 [43].	W/mK
ε	0.6	-

* Measured parameters.

In this table; $c_{p,mandrel}$, $c_{p,pe}$, $c_{p,ne}$, $c_{p,pecc}$, $c_{p,necc}$, $c_{p,sep}$, c_p, $c_{p,shell}$ represents the specific heat value of the mandrel, positive electrode, negative electrode, positive electrode current collector, negative electrode current collector, separator, cell, and the shell, respectively. In addition; $\rho_{mandrel}$, ρ_c, and ρ_{shell} are the density values of the mandrel, cell, and the shell, respectively. Note that the cell's radial and angular thermal conductivity can be obtained using Eqs. (4.8-4.10),

$$\lambda_{rad} = \frac{L_{bat}}{\frac{L_{pe}}{\lambda_{pe}} + \frac{L_{ne}}{\lambda_{ne}} + \frac{L_{pecc}}{\lambda_{pecc}} + \frac{L_{necc}}{\lambda_{necc}} + \frac{L_{sep}}{\lambda_{sep}}} \tag{4.8}$$

$$\lambda_{ang} = \frac{\lambda_{pe}L_{pe} + \lambda_{ne}L_{ne} + \lambda_{pecc}L_{pecc} + \lambda_{necc}L_{necc} + \lambda_{sep}L_{sep}}{L_{bat}} \tag{4.9}$$

where λ_{ang} is the angular thermal conductivity and λ_{pe}, λ_{ne}, λ_{pecc}, λ_{necc}, λ_{sep} demonstrate the thermal conductivities of positive electrode, negative electrode, positive electrode current collector, negative electrode current collector, and separator, respectively. L_{bat} is the length of the cell and is equal to the summation of each thickness value as stated below.

$$L_{bat} = L_{pe} + L_{ne} + L_{pecc} + L_{necc} + L_{sep} \tag{4.10}$$

It is seen that the thermal parameters of the Li-ion cell are found to be consistent compared to the geometrical, electrical, and chemical parameters. Only a few discrepancies have been encountered in the literature. It was found that the mandrel material of an NCA battery is used differently in some applications [92, 110, 111, 117]. Table 4.4 compares the thermal properties of the mandrel.

Table 4.4. Thermal parameters of the nylon and nickel foil mandrel.

Property	**Nylon [92, 110]**	**Nickel Foil [111, 117]**
Heat Capacity	1700 J/kgK	460 J/kgK
Density	1150 kg/m^3	8890 kg/m^3
Thermal conductivity	0.26 W/(mK)	70 W/(mK)
Relative permittivity	4	110
Coefficient of thermal expansion	280e-6 (1/K)	13.3e-6 (1/K)
Young's modulus	2 GPa	207 GPa
Poisson's ratio	0.4	0.31

Most of the selected parameters are found in a wide range, which complicates the model input values selection. Therefore, a sensitivity analysis was performed to develop a more accurate and comprehensive model.

4.2. Sensitivity Analysis

Time step and mesh level selections have significant effects on the computational effort during the simulation of the electrochemical-thermal model. Therefore, before the sensitivity analysis, the model results were compared using different mesh levels and time step selections.

4.2.1. Effects of Meshing and Time Step Selection on the Results of the Sensitivity Analysis

Mesh types are divided into nine different levels. It indicates the cell size of electrical and thermal models. The below table shows the mesh type options and the corresponding domain elements for the models.

Table 4.5. Mesh types and the corresponding number of mesh elements according to the developed model.

Mesh level	Electrochemical Model Domain Element Number	Thermal Model Domain Element Number
1	12	3152
2	14	4701
3	17	8873
4	24	22488
5	41	60412
6	56	214236
7	100	335491
8	100	579411
9	101	1181240

Different mesh levels were compared to investigate the effects of mesh types on the results. The comparison was conducted for the cell's temperature, and voltage predictions during the 1.5C rate discharging process since this case provides the most distinguished temperature and voltage variations. First, the cell's voltage and temperature variations were predicted with the 5^{th} level meshed electrochemical-thermal model. Then four different models were developed with

various mesh levels. Finally, the voltage and temperature predictions of these four models were compared with the 5th level meshed model. The differences between these model results are presented in Figure 4.3. Note that ECM means electrochemical model, and TM indicates the thermal model in the figure.

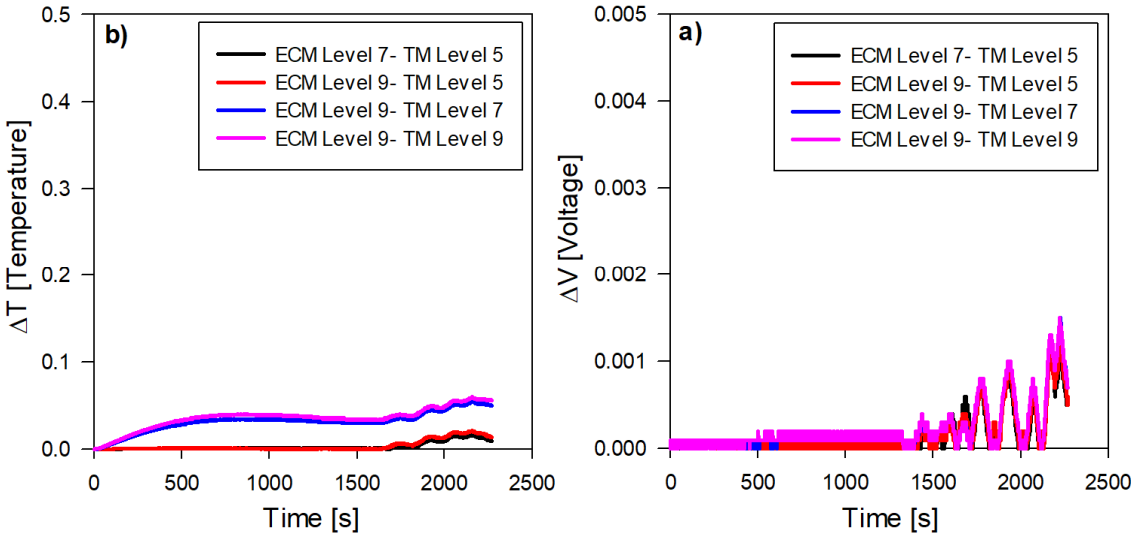

Figure 4.3. The voltage (a) and temperature (b) differences between the various meshed and the 5th level meshed models during a 1.5C rate discharging operation.

The results show that the voltage and temperature differences during the discharging process did not exceed 2 mV and 0.1°C, respectively. This indicates that the model can be developed with 41 to 101 domain elements for the electrochemical model and 60412 to 1181240 domain elements for the thermal model. Hence, the electrochemical model was developed with 100 domain elements, whereas the thermal model consists of 335491 domain elements while performing the sensitivity analysis of the electrochemical-thermal model.

Another significant factor affecting the model results is the time step selection. The temperature and voltage variations were obtained with 1-second and 10 second time steps, and the temperature and voltage differences between the two models are presented in Figure 4.4.

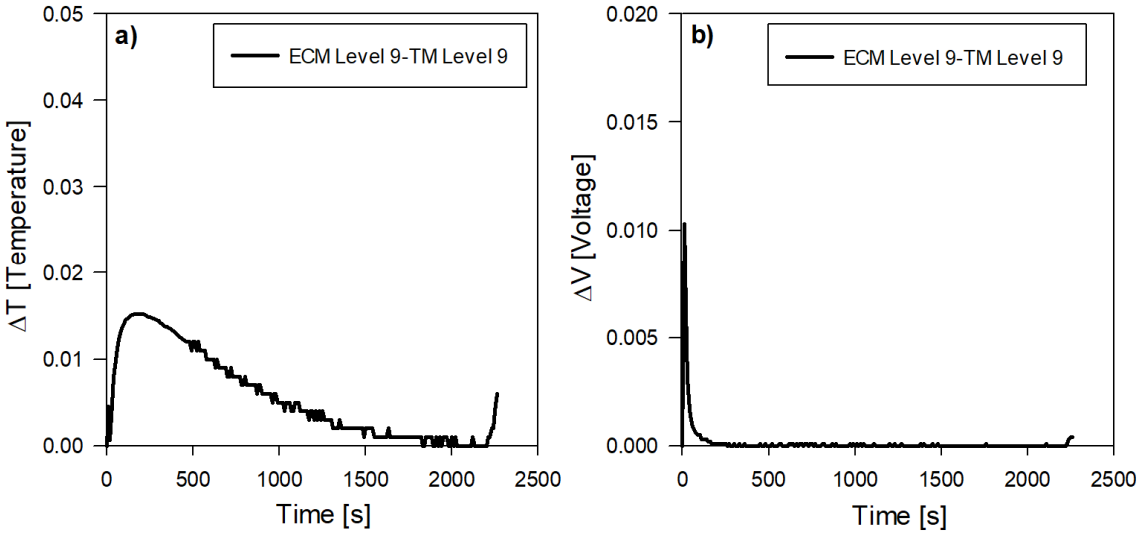

Figure 4.4. Differences in the temperature (a) and voltage (b) values that predicted using 1-second and 10 second time step conditions during a 1.5C rate discharging operation.

Figures 4.4a and 4.4b show that the results are almost identical for each operating condition. The maximum difference in temperature and voltage predictions were calculated as 0.0152°C and 10.3 mV, respectively. Thus, the model was developed with 10 seconds time step while performing the sensitivity analysis of the electrochemical-thermal model.

The following subsections present the sensitivity analysis results for each geometrical, electrochemical, and thermal parameter.

4.2.2. Trends and Results

Initial model input values (MIVs) presented in Table 4.6 were selected considering the parameters in Chapter 4.1. During the analysis, MIVs were kept constant except the investigated parameter. The investigated parameter is selected as the maximum and minimum value within the presented range. The simulations were carried out and predicted cell voltage values and surface temperatures were compared with the experimental data at different C rates. The results were compared and discussed by plots. The comparison was also

performed considering both the RMS error and the maximum true error presented in tables.

Table 4.6. The Initial MIV and the maximum and minimum values from literature.

Parameter	Initial MIV	Min. Value	Max. Value	Unit
L_{sep}	10	10	25	μm
L_{necc}	10	7.5	18	μm
L_{pecc}	15	14	30	μm
L_{ne}	205	42.6	243	μm
L_{pe}	158	32.8	165	μm
r_{ne}	11	2	18	μm
r_{pe}	2.5	0.25	8.5	μm
$\varepsilon_{s,ne}$	0.62	0.58	0.62	-
$\varepsilon_{s,pe}$	0.482	0.482	0.5	-
$\varepsilon_{l,ne}$	0.332	0.31	0.485	-
$\varepsilon_{l,pe}$	0.29	0.29	0.4	-
$\varepsilon_{l,sep}$	0.45	0.4	0.724	-
k_{ne}	1.76e-11	1.76e-11	5.04e-11	$m^{2.5}/(mol^{0.5}s)$
k_{pe}	1.00e-10	2.33e-11	1.00e-10	$m^{2.5}/(mol^{0.5}s)$
p_{sep}	3	1.5	4	-
p_{pe}	2.89	1.5	2.89	-
$c_{l,0}$	1200	1000	1200	mol/m^3

c_p	750	700	868.1	kJ/kgK
λ_{pe}	5	1.58	5	W/mK
λ_{ne}	1.04	1	5	W/mK
λ_{sep}	0.3344	0.15	0.3344	W/mK
λ_{shell}	0.638	0.638	13.57	W/mK

4.2.2.1. Analysis of the Geometrical Parameters

Figure 4.5 shows the effects of negative electrode thickness on voltage and temperature predictions during a 1C rate discharging process. It can be revealed that the decrease in negative electrode thickness from 243 µm to 42.6 µm causes an early and sudden voltage drop which leads to an instant temperature increment. On the other hand, decreasing the negative electrode thickness by 38 µm from 243 µm affects only the temperature profile and slightly increases the temperature variation during the discharging process.

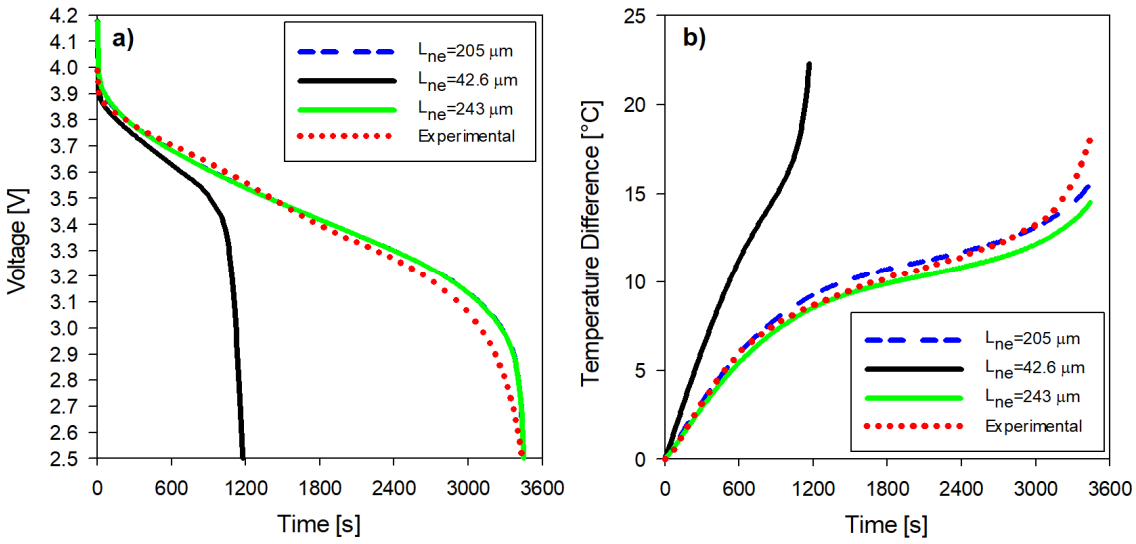

Figure 4.5. Effects of negative electrode thickness on voltage (a) and temperature (b) predictions of a discharging cell at 1C rate.

Figure 4.6 shows the effects of positive electrode thickness on voltage and temperature profiles of a 1-C rate discharging cell.

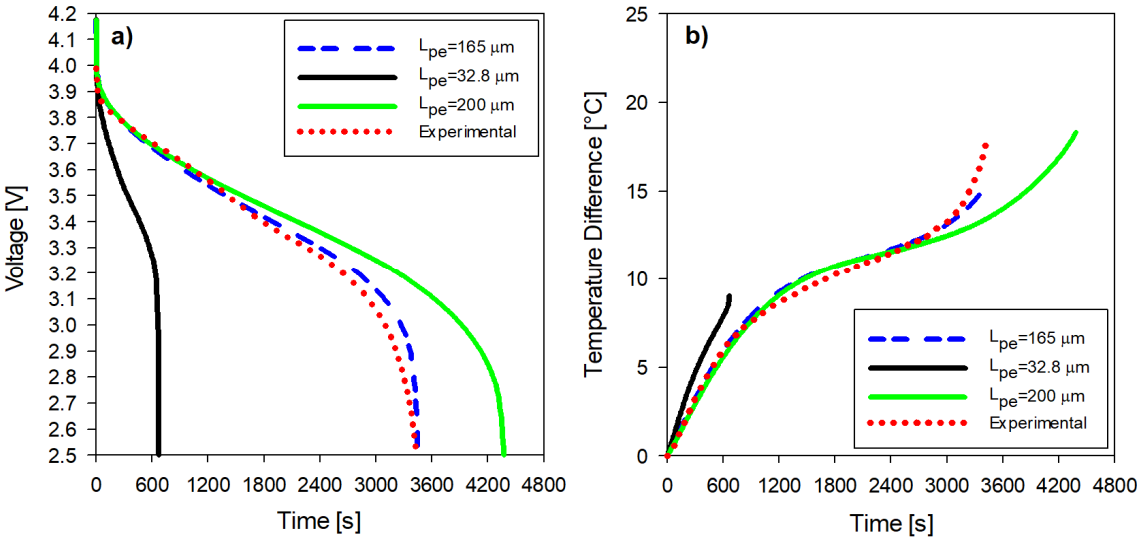

Figure 4.6. Effects of positive electrode thickness on voltage (a) and temperature (b) predictions of a discharging cell at 1C rate.

The model input value of the positive electrode thickness is 165 µm. Increasing this value ended up with a discharging process that remains longer than expected. On the other hand, decreasing this value finishes the discharging too early, so the cell reaches low-temperature values compared to the experimental conditions.

Figure 4.7 shows the effects of negative electrode radius on voltage and temperature predictions during a 1C rate discharging process.

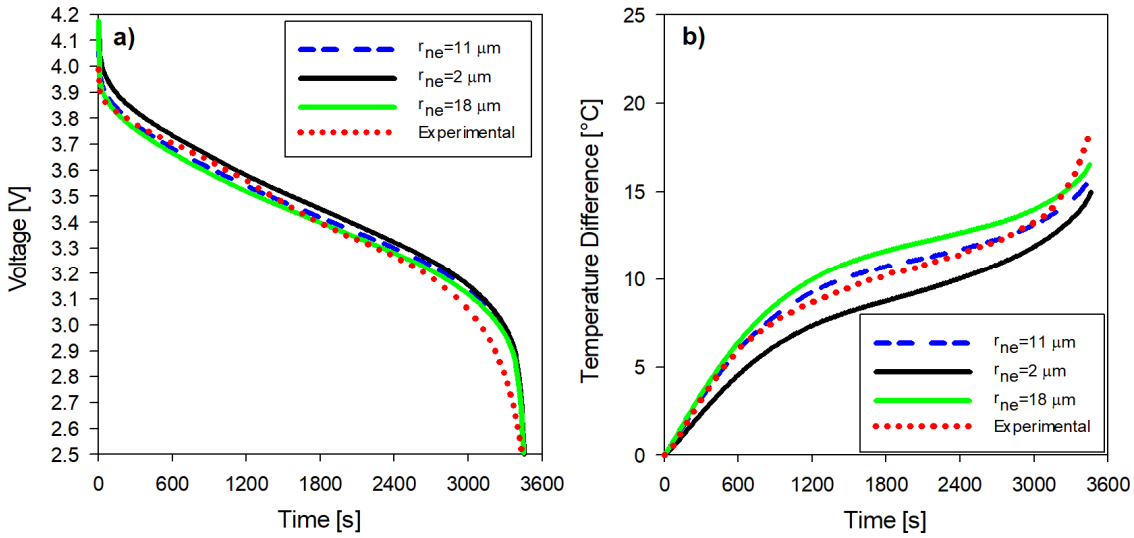

Figure 4.7. Effects of negative electrode radius on voltage (a) and temperature (b) profiles of a cell during a 1C rate discharging process.

Active particles in both electrodes are assumed to be a perfect sphere with an average radius, which in this case is 11 µm for the negative electrode. The voltage predictions are tolerable even though the slight changes in voltage profiles for 2, and 18 µm negative electrode radius values. Figure 4.7b denotes that the temperature predictions are more affected by the particle size of the negative electrode. The results show that the temperature variation in the model is directly proportional to the negative electrode size.

Figure 4.8 displays the effects of positive electrode radius on voltage and temperature predictions of a 1C rate discharging cell. The model uses 2.5 µm as the average radius of the positive electrode. Increasing this radius up to 8.5 µm decreases the predicted voltage values and increases the cell's surface temperature due to an increase in overpotentials during the discharging. Meanwhile, decreasing the positive electrode radius by up to 10 times did not significantly alter the temperature and voltage predictions, as can be followed in Figure 4.8b.

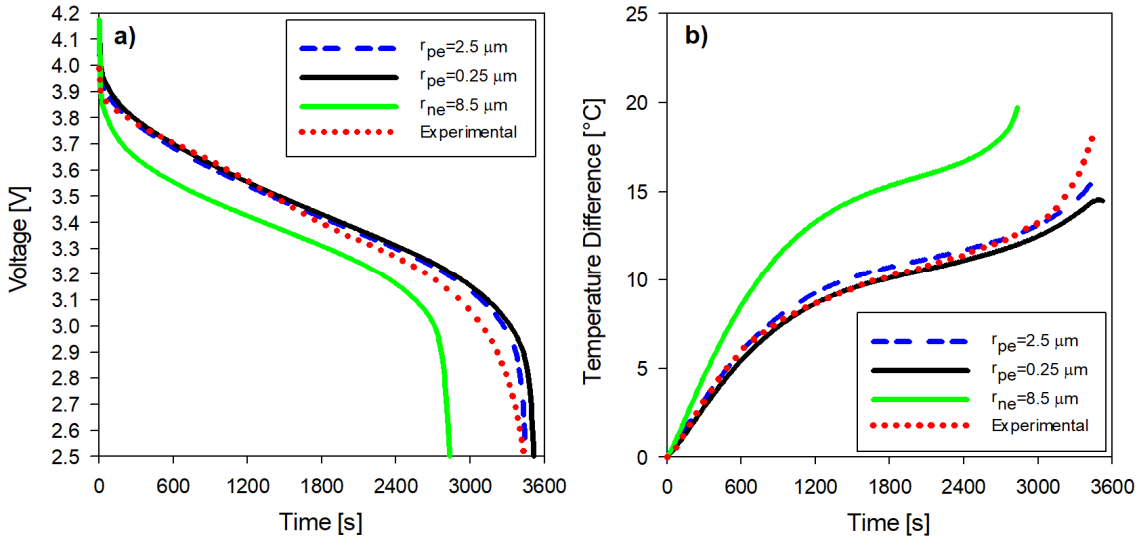

Figure 4.8. Effects of positive electrode radius on voltage (a) and temperature (b) profiles of a cell during a 1C rate discharging process.

Table 4.7 presents the voltage and temperature prediction errors for different geometrical input parameters during the 0.5, 1, and 1.5C rate discharging processes. Note that shaded areas denote approximately twice or more of a change in these tables.

Table 4.7. Voltage and temperature prediction errors of various geometrical parameters for 0.5-1-1.5C rate discharging processes.

Parameter	Voltage RMS Error			Voltage Max. True Error			Temperature RMS Error			Temperature Max. True Error		
	0.5C	1C	1.5C	0.5C	1C	1.5C	0.5C	1C	1.5C	0.5C	1C	1.5C
MIV	0.11	0.06	0.03	0.56	0.22	0.16	0.93	0.53	0.50	5.03	2.42	1.53
L_{sep}= 25	0.10	0.05	0.06	0.55	0.19	0.21	0.88	0.86	1.63	4.84	1.71	3.28
L_{necc}= 7.5	0.11	0.06	0.03	0.56	0.22	0.16	0.93	0.54	0.56	5.00	2.34	1.65
L_{necc}= 18	0.11	0.06	0.03	0.56	0.22	0.16	0.96	0.54	0.37	5.10	2.66	1.29
L_{pecc}= 14	0.11	0.06	0.03	0.56	0.22	0.16	0.93	0.54	0.52	5.02	2.39	1.58
L_{pecc}= 30	0.11	0.06	0.03	0.56	0.22	0.17	0.98	0.58	0.42	5.17	2.86	0.81

L_{ne}= 42.6*	0.24	0.22	0.19	1.16	1.02	0.90	3.19	6.06	8.10	9.63	13.79	16.32
L_{ne}= 243	0.11	0.06	0.03	0.57	0.22	0.18	1.08	0.88	0.94	5.40	3.51	1.41
L_{pe}= 32.8*	0.35	0.32	0.29	1.09	1.04	0.68	0.47	1.51	2.48	1.08	2.60	3.72
L_{pe}= 200	0.17	0.15	0.08	0.84	0.65	0.31	1.01	0.93	0.72	5.39	4.56	2.27
r_{ne}= 2	0.12	0.08	0.05	0.58	0.24	0.17	1.23	1.45	2.13	5.36	3.40	2.93
r_{ne}= 18	0.10	0.06	0.04	0.55	0.21	0.18	0.87	1.03	1.37	4.66	1.64	2.49
r_{pe}= 0.25	0.18	0.08	0.03	0.62	0.38	0.14	1.02	0.75	0.87	5.35	3.62	1.37
r_{pe}= 8.5	0.09	0.14	0.21	0.79	0.60	0.69	1.46	4.41	6.69	2.22	7.16	11.95

*Discharging finishes too early.

The results show that the electrode thickness values are the most dominant geometrical parameters in voltage and temperature estimations. Besides, it was observed that the discharging process finishes too early at lower electrode thicknesses. The separator thickness has no significant effect on voltage prediction, but it may alter the temperature profile, especially at high C rates. The impacts of the current collector thicknesses on a cell's thermal and electrical performance can be assumed as negligible. The average particle radius of both electrodes alters the thermal behavior of the cell at high discharge rates. The positive electrode particle radius can change the cell's voltage variation. However, the negative electrode particle radius is not effective on voltage predictions.

As a result of an analysis regarding the geometrical parameters, shaded areas also denote that the geometrical properties are much more effective at higher current processes. Besides, the thicknesses of the negative and positive electrodes should be carefully selected as they have remarkable impacts on the voltage and temperature profiles of the cell.

4.2.2.2. Analysis of the Electrochemical Parameters

Figure 4.9 compares the effects of electrolyte phase volume fractions on voltage and temperature predictions of a 1C rate discharging cell.

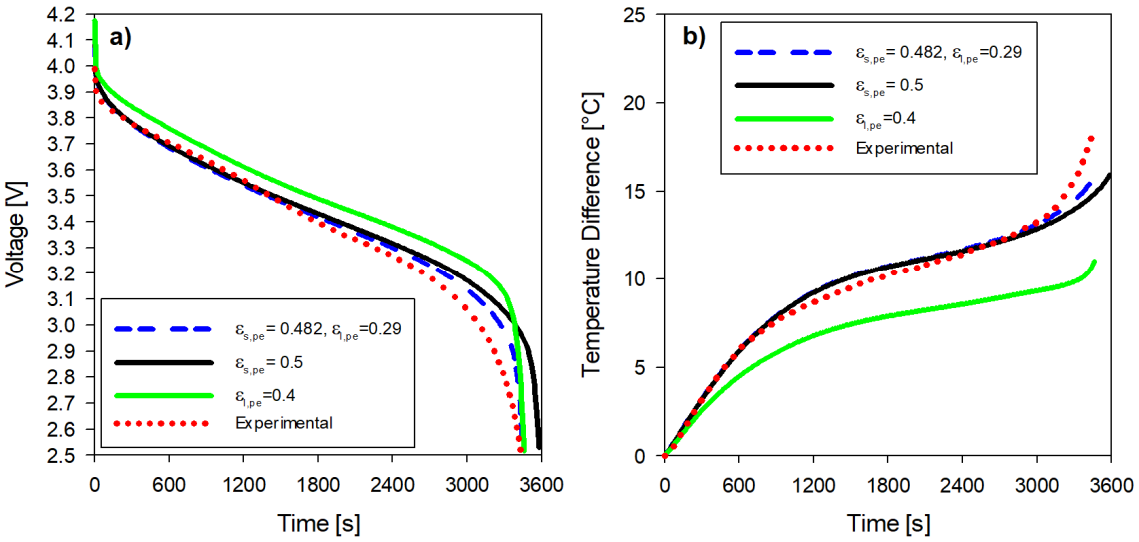

Figure 4.9. Effects of the electrolyte and solid phase volume fractions in positive electrode on voltage (a) and temperature (b) profiles of a cell during a 1C rate discharging process.

The change from 0.482 to 0.5 for the solid phase volume fraction in positive electrode has no noticeable effect on the temperature and voltage predictions. However, the liquid phase volume fraction in positive electrode significantly alters the predicted temperature and voltage profiles within the investigated range.

Figure 4.10 compares the effects of the Bruggeman coefficient and salt concentration values on voltage and temperature predictions of a 1C rate discharging cell. The Bruggeman coefficient of the positive electrode affects the predicted voltage curve, hence the irreversible heat generation and the temperature of the cell. On the other hand, the initial electrolyte salt concentration has no noticeable effect during 1C rate discharging but may alter the cell's thermal behavior at higher current rates according to the error calculations that is presented in Table 4.8.

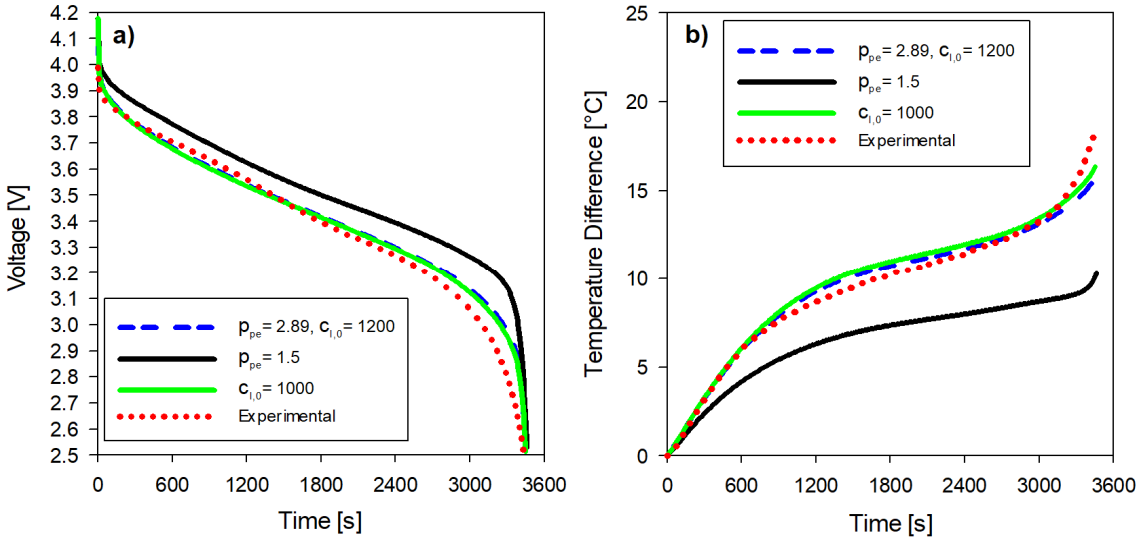

Figure 4.10. Effects of the Bruggeman coefficient and the initial electrolyte salt concentration on voltage (a) and temperature (b) profiles of a discharging cell at 1C rate.

The voltage and temperature prediction errors were presented in Table 4.8 for different electrochemical input parameters during the 0.5, 1, and 1.5C rate discharging processes.

Table 4.8. Voltage and temperature prediction errors of various electrochemical parameters for 0.5-1-1.5C rate discharging processes.

Parameters	Voltage RMS Error			Voltage Max. True Error			Temperature RMS Error			Temperature Max. True Error		
	0.5C	1C	1.5C	0.5C	1C	1.5C	0.5C	1C	1.5C	0.5C	1C	1.5C
MIV	0.11	0.06	0.03	0.56	0.22	0.16	0.93	0.53	0.50	5.03	2.42	1.53
$\varepsilon_{s,ne}$ = 0.58	0.11	0.06	0.03	0.56	0.21	0.17	0.91	0.54	0.67	4.96	2.18	1.92
$\varepsilon_{s,pe}$ = 0.50	0.13	0.10	0.03	0.69	0.46	0.12	0.97	0.67	0.23	5.26	3.34	0.51
$\varepsilon_{l,ne}$ = 0.485	0.11	0.08	0.03	0.58	0.26	0.11	1.07	0.84	0.76	5.43	3.60	1.30
$\varepsilon_{l,ne}$ = 0.31	0.11	0.06	0.03	0.56	0.21	0.18	0.90	0.55	0.74	4.92	2.11	2.08

$\varepsilon_{l,pe}$ = 0.40	0.14	0.13	0.12	0.62	0.35	0.20	1.65	2.89	4.72	6.51	7.36	8.13
$\varepsilon_{l,sep}$ = 0.40	0.11	0.06	0.03	0.56	0.21	0.17	0.90	0.63	0.91	4.93	2.09	2.22
$\varepsilon_{l,sep}$ = 0.724	0.11	0.07	0.03	0.57	0.24	0.14	1.00	0.64	0.66	5.20	2.99	1.05
k_{ne}= 5.04 e-11	0.11	0.07	0.04	0.57	0.24	0.15	1.11	1.03	1.41	5.27	3.17	2.02
k_{pe}= 2.33 e-11	0.11	0.05	0.04	0.55	0.19	0.20	0.88	0.66	1.10	4.84	1.75	2.68
p_{sep}= 1.5	0.11	0.07	0.03	0.57	0.24	0.14	0.99	0.62	0.60	5.18	2.96	0.97
p_{sep}= 4	0.10	0.05	0.05	0.55	0.20	0.20	0.87	1.00	1.86	4.75	1.49	3.58
p_{pe}= 1.5	0.14	0.14	0.14	0.63	0.37	0.23	1.80	3.39	5.55	6.74	8.10	9.41
$c_{l,0}$ =1000	0.11	0.05	0.04	0.56	0.20	0.20	0.93	0.58	1.20	5.01	1.86	3.34

4.2.2.3. Analysis of the Thermal Parameters

The simulations were conducted with various thermal parameters for a discharging cell, and the errors were presented in Table 4.9.

Table 4.9. Voltage and temperature prediction errors of various thermal parameters for 0.5-1-1.5C rate discharging processes.

Parameters	Voltage RMSE			Voltage Maximum Error			Temperature RMSE			Temperature Maximum Error		
	0.5C	**1C**	**1.5C**	**0.5C**	**1C**	**1.5C**	**0.5C**	**1C**	**1.5C**	**0.5C**	**1C**	**1.5C**
MIV	0.11	0.06	0.03	0.56	0.22	0.16	0.93	0.53	0.50	5.03	2.42	1.53
c_p = 700	0.11	0.06	0.03	0.56	0.22	0.16	0.93	0.61	0.75	5.00	2.25	1.88
c_p = 868.12	0.11	0.06	0.03	0.56	0.22	0.17	0.95	0.56	0.74	5.08	2.79	1.29
λ_{pe} = 1.58	0.11	0.06	0.03	0.56	0.22	0.16	0.93	0.53	0.48	5.03	2.43	1.49
λ_{ne} = 1	0.11	0.06	0.03	0.56	0.22	0.16	0.93	0.54	0.50	5.03	2.42	1.52
λ_{ne} = 5	0.11	0.06	0.03	0.56	0.22	0.16	0.93	0.54	0.54	5.02	2.38	1.62

λ_{sep} = 0.15	0.11	0.06	0.03	0.56	0.22	0.16	0.93	0.53	0.49	5.03	2.43	1.51
λ_{shell} = 13.57	0.11	0.06	0.03	0.56	0.22	0.16	0.93	0.54	0.53	5.02	2.39	1.60

The results show that none of the thermal parameters affect the voltage predictions. The voltage RMSE and maximum true errors were obtained same compared to the simulation results with the initial MIVs. On the other hand, within the investigated range, the average heat capacity of the cell has a minor impact on the cell's thermal performance during the discharging processes. Figure 4.11 presents the effects of the cell average specific heat capacity on voltage and temperature profiles of a discharging cell at 1C rate.

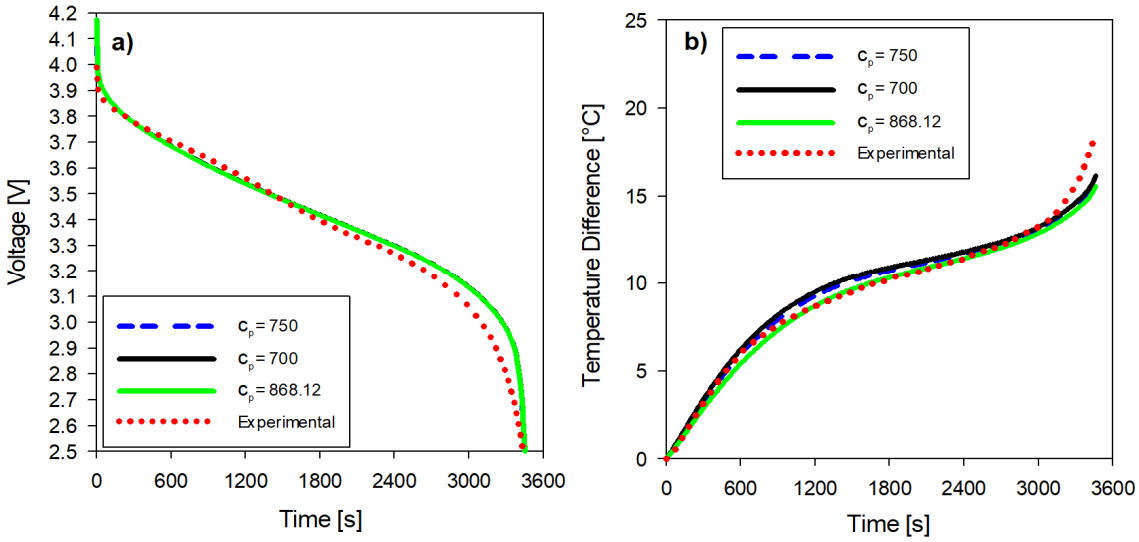

Figure 4.11. Effects of the cell average specific heat capacity on voltage (a) and temperature (b) profiles of a discharging cell at 1C rate.

Thermal conductivity values of the positive electrode, negative electrode, separator, and shell can be assumed electrically and thermally ineffective considering Table 4.9. Note that the thermal conductivity values in the positive electrode, negative electrode, and separator alter the angular and radial thermal conductivities, as indicated in Eq. (4.8) and Eq. (4.9). Therefore, simulations were

performed with minor changes in thermal conductivities, which results in no significant alterations in terms of thermal characteristics.

As a result of the sensitivity analysis, the electrical and thermal impacts of the model parameters were investigated during various discharging processes in detail. The results emphasize that the input parameters can considerably alter the model results in the range presented in the literature. On the other hand, considering the presented RMS and maximum true errors, initial MIVs are the most appropriate parameters for a comprehensive electrochemical-thermal model that is valid for different discharging conditions. In addition, the model can be adapted to be performed under a specific discharging condition in order to obtain more accurate results.

4.3. Electrochemical Thermal Coupled Model

In Chapter 3, the two-dimensional axisymmetric lumped model was examined in which the electrical and thermal characteristics of the cell were predicted without considering any electrochemical reaction. In this section, the effects of charge and mass transfers of solids and liquids within the cell can be represented within the electrochemical-thermal coupled model. The electrochemical model is used in one dimension to predict the voltage variation and the heat generation within the cell accurately. Subsequently, a thermal model in three dimensions was coupled with this model and used to predict the thermal behavior of the cell during the charging and discharging processes. The comparison of the electrochemical-thermal and lumped model is presented in Table 4.10.

Table 4.10. The comparison of the electrochemical-thermal and lumped model.

Method	Advantages	Disadvantages
Electrochemical and Thermal Model	• Electrochemical interactions are considered for voltage predictions.	• More parameters needed • More computational effort

	• More realistic approach	
Lumped Model	• Internal resistance value is considered for voltage prediction • Fewer parameters needed • Lower computational effort	• Less realistic approach • Valid for specific cases • Less repeatable

4.3.1 Electrochemical Model

The electrochemical process inside the battery takes place in two different phases, the liquid phase (electrolyte) and the solid phase (electrodes). The effects of the gas phase on the thermal and electrical performance of the Li-ion battery are neglected in this study. The electrolyte phase includes the mass and charge transfer via migration, diffusion, or convection between the electrodes through an electrolyte solution accompanied by interfacial reactions at the surface of the electrodes. On the other hand, the solid phase copes with charge transfer frequently by conduction within the solid phase of the electrode, such as current collectors [121].

In the electrochemical model, the charge and mass conservation equations are employed to predict the electrical responses of the cell. The model geometry, materials, and chemical properties are defined in different model interfaces. Material properties are determined considering the NCR18650b battery cell. Table 4.11 presents the required input parameters for each material.

Table 4.11. Required properties to define the Electrolyte (ELE), negative electrode (NE), and positive electrode (PE) materials.

Properties	ELE	NE	PE
Electrical conductivity	X	X	X

Diffusion coefficient	X	X	X
Transport number	X	X	X
Activity dependence	X		
Heat capacity at constant pressure		X	X
Equilibrium potential		X	X
Temperature derivative of equilibrium potential		X	X
Reference concentration		X	X
Operational State of Charge interval		X	X

These properties can be employed either as constant or variable. As an example, the electrical conductivity of an anode Li_xC_6 is 100 S/m, but the equilibrium potential of the anode should be represented by a function of both temperature and the SoC.

The charge condition of the Li-ion batteries can be represented with the dimensionless SoC values as described in Chapter 1. Apart from the lumped battery model, the electrochemical-thermal model uses different SoC values for both negative and positive electrodes. The following equation can be used to calculate these values.

$$SoC_{electrode} = \frac{c_e}{c_{ref,e}} \tag{4.11}$$

In this equation, c_e denotes the Li-ion concentration of the electrode, and $c_{ref,e}$ is the maximum Li-ion concentration value. Total SoC= 1 indicates that all the available Li-ions are placed on the negative electrode side. Considering the previous studies [99, 103, 107], the maximum and minimum SoC values for negative and positive electrodes are indicated in Table 4.12.

Table 4.12. Reference SoC values for negative and positive electrodes.

Properties	SoC	Concentration (mol/m^3)
Maximum negative electrode SoC	0.98	29943.9
Minimum negative electrode SoC	0	0
Maximum positive electrode SoC	0.98	48944.1
Minimum positive electrode SoC	0.36	17979.5

The OCV value of the fully charged NCR18650b cell should be between 4.1-4.2 V, depending on its storage duration and current capacity. Thus, to adjust the battery as fully charged, the concentration values for the positive and negative electrodes are defined as 20000 and 29900, respectively.

The equilibrium potentials are defined by two plots for each electrode, as shown in Figure 4.12. Furthermore, the similar equilibrium voltage plots that are used in other battery model applications can be found in Eq. (4.4), Eq. (4.5), and Eq. (4.6) [99, 107].

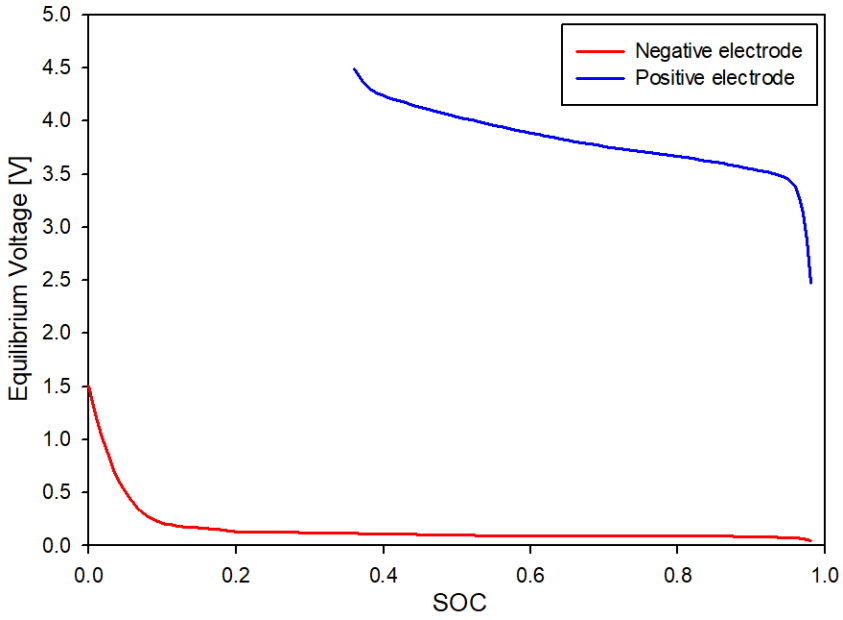

Figure 4.12. Equilibrium potentials for negative and positive electrodes [30, 107, 109].

Therefore, the equilibrium voltage value of the cell can be evaluated from the Eqs. (4.12) to (4.14).

$$E_{pe} = f\left(\frac{c_{pe}}{c_{ref,pe}}\right) \tag{4.12}$$

$$E_{ne} = g\left(\frac{c_{ne}}{c_{ref,ne}}\right) \tag{4.13}$$

$$E_c = E_{pe} - E_{ne} \tag{4.14}$$

In these equations, E_{pe} and E_{ne} represent the equilibrium potential of the positive and negative electrodes, respectively. c_{pe} shows the Lithium concentration and $c_{ref,pe}$ is the maximum available Li-ion concentration in the positive electrode, whereas c_{ne} is the Lithium concentration and $c_{ref,ne}$ the maximum available Li-ion concentration in the negative electrode. The equilibrium potential of the cell is represented by E_c. The model also considers the effects of temperature variation on equilibrium potential. Thermal coupled electrochemical models use a relation that shows the temperature derivative of the equilibrium potential at various SoC values. Thus, the equilibrium potential evolves in Eq. (4.15).

$$E_c = \left[f\left(\frac{c_{pe}}{c_{ref,pe}}\right) + \frac{dE_{pe}}{dT}(T - T_{ref})\right] - \left[g\left(\frac{c_{ne}}{c_{ref,ne}}\right) + \frac{dE_{ne}}{dT}(T - T_{ref})\right] \tag{4.15}$$

4.3.1.1 Electrochemical Reactions within the Cell

In this part, mass and charge balances for liquid and solid phases will be investigated in one dimension considering the porous electrode theory by Newman et al. [122, 123].

4.3.1.1.1 Li-ion concentration in the solid phase

Fick's law of diffusion defines the conservation of Li-ions in a solid spherical particle as,

$$r\frac{\partial c_s}{\partial t} = \frac{D_s}{r^2}\frac{\partial}{\partial r}\left(r^2\frac{\partial c_s}{\partial r}\right) \tag{4.16}$$

where c_s is the Li-ion concentration in the solid phase, D_s is the solid phase diffusion coefficient, t is the time, and r represents the radial direction in the solid spherical particle. No flux at the center of the spherical particle is assumed:

$$\left.\frac{\partial c_s}{\partial r}\right|_{r=0} = 0 \tag{4.17}$$

In the meantime, the molar flux of lithium at the solid-liquid interface can be described by Eq. (4.18)

$$-D_s\left.\frac{\partial c_s}{\partial r}\right|_{r=r_{sphere}} = \frac{J_{Li}}{a_{surf}F} \tag{4.18}$$

where r_{sphere} is the radius of the spherical particle, J_{Li} denotes the volumetric rate of electrochemical reaction at the particle surface, F is the Faraday's constant, and a_{surf} is the electrode specific surface area.

4.3.1.1.2 Li-ion concentration in the liquid phase

The mass balance for the Li-ions in the liquid phase can be described by Eq. (4.19)

$$\frac{\partial(\varepsilon_l c_l)}{\partial t} = \frac{\partial}{\partial x}\left(D_{l,eff}\frac{\partial c_l}{\partial x}\right) + (1-t_+)\frac{J_{Li}}{F} \tag{4.19}$$

where ε_l denotes the electrolyte phase volume fraction, c_l is the Li-ion concentration in the liquid phase, $D_{l,eff}$ is the effective electrolyte diffusion coefficient, and t_+ is the transference number of Li-ions. Eqs. (4.20) and (4.21) indicate that no fluxes can be observed at the x=0 and x=L since the current collectors do not pass the Li-ions. However, the flux is continuous at each interface, as seen from Eqs. (4.22) and (4.23).

$$-D_{l,eff}^{ne} \left.\frac{\partial c}{\partial x}\right|_{x=0} = 0 \tag{4.20}$$

$$-D_{l,eff}^{pe} \left.\frac{\partial c}{\partial x}\right|_{x=L} = 0 \tag{4.21}$$

$$-D_{l,eff}^{ne} \left.\frac{\partial c}{\partial x}\right|_{x=L_{ne}^-} = -D_{l,eff}^{sep} \left.\frac{\partial c}{\partial x}\right|_{x=L_{ne}^+} \tag{4.22}$$

$$-D_{l,eff}^{sep} \left.\frac{\partial c}{\partial x}\right|_{x=(L_{ne}+L_{sep})^-} = -D_{l,eff}^{pe} \left.\frac{\partial c}{\partial x}\right|_{x=(L_{ne}+L_{sep})+} \tag{4.23}$$

On the other hand, the separator allows the Li-ions to move continuously at the interfaces between the electrodes in Eq. (4.24) and the separator in Eq. (4.25).

$$c_l\big|_{x=L_{ne}^-} = c_l\big|_{x=L_{ne}^+} \tag{4.24}$$

$$c_l\big|_{x=(L_{ne}+L_{sep})^-} = c_l\big|_{x=(L_{ne}+L_{sep})^+} \tag{4.25}$$

4.3.1.1.3 Charge conservation in the solid phase

Ohm's law defines the charge conservation in the solid phase,

$$\frac{\partial}{\partial x}\left(\sigma_{s,eff}\frac{\partial \phi_s}{\partial x}\right) = J_{Li} \tag{4.26}$$

where ϕ_s is the solid phase potential, $\sigma_{s,eff}$ denotes the effective electrical conductivity, and can be evaluated by the following equation.

$$\sigma_{s,eff} = \sigma_s.\varepsilon_s^{\,p} \tag{4.27}$$

In Eq. (4.27), σ_s is the electrical conductivity, ε_s is the solid phase volume fraction, and p denotes the Bruggeman coefficient. Eq. (4.28) denotes that the charge flux is equal to the current density at the end of the cell,

$$-\sigma_{s,eff}^{\,pe}\frac{\partial \phi_s}{\partial x}\bigg|_{x=L} = I_{app} = \frac{I}{A_e} \tag{4.28}$$

where I_{app} is the applied current density, I is the applied current and A_e is the electrode plate area. Charge flux is not allowed at each interface, so the Eqs. (4.29) and (4.30) should be equal to zero.

$$-\sigma_{s,eff}^{\,ne}\frac{\partial \phi_s}{\partial x}\bigg|_{x=L_{ne}} = 0 \tag{4.29}$$

$$-\sigma_{s,eff}^{\,pe}\frac{\partial \phi_s}{\partial x}\bigg|_{x=L_{ne}+L_{sep}} = 0 \tag{4.30}$$

4.3.1.1.4 Charge conservation in the liquid phase

The charge conservation in the liquid phase is defined by Eq. (4.31),

$$\frac{\partial}{\partial x}\left(-\sigma_{l,eff}\frac{\partial \phi_l}{\partial x}+2R_uT\sigma_{l,eff}\frac{(1-t_+)}{F}\frac{\partial \ln c_l}{\partial x}\left(1+\frac{\partial \ln f}{\partial \ln c_l}\right)\right)=J_{Li} \tag{4.31}$$

where ϕ_l is the electrolyte phase potential, f is the electrolyte activity coefficient, and $\sigma_{l,eff}$ is the effective electrolyte conductivity which can be expressed by Eq. (4.32),

$$\sigma_{l,eff} = \sigma_l.\varepsilon_l^{\,p} \tag{4.32}$$

Where σ_l shows the electrolyte conductivity. Eqs. (4.33) and (4.34) show that no charge flux is allowed at x=0, and x=L in the electrolyte phase, respectively.

$$-\sigma_{l,eff}^{\,ne}\left.\frac{\partial \phi_l}{\partial x}\right|_{x=0} = 0 \tag{4.33}$$

$$-\sigma_{l,eff}^{\,pe}\left.\frac{\partial \phi_l}{\partial x}\right|_{x=L} = 0 \tag{4.34}$$

On the other hand, Eqs. (4.35-4.38) indicate that the potentials and their fluxes are continuous at the interfaces.

$$\left.\phi_l\right|_{x=L_{ne}^{-}} = \left.\phi_l\right|_{x=L_{ne}^{+}} \tag{4.35}$$

$$\left.\phi_l\right|_{x=(L_{ne}+L_{sep})^{-}} = \left.\phi_l\right|_{x=(L_{ne}+L_{sep})^{+}} \tag{4.36}$$

$$-\sigma_{l,eff}^{\,ne}\left.\frac{\partial \phi_l}{\partial x}\right|_{x=L_{ne}^{-}} = -\sigma_{l,eff}^{\,sep}\left.\frac{\partial \phi_l}{\partial x}\right|_{x=L_{ne}^{+}} \tag{4.37}$$

$$-\sigma_{l,eff}^{\,sep}\left.\frac{\partial \phi_l}{\partial x}\right|_{x=(L_{ne}+L_{sep})^{-}} = -\sigma_{l,eff}^{\,pe}\left.\frac{\partial \phi_l}{\partial x}\right|_{x=(L_{ne}+L_{sep})^{+}} \tag{4.38}$$

4.3.1.1.5 Electrode Kinetics

The charge transfer reactions can be expressed by Butler- Volmer equation,

$$J_{Li} = i_0 a_{surf} \left[\exp\left(\frac{\alpha_{an} F}{R_u T} \eta \right) - \exp\left(\frac{\alpha_{ca} F}{R_u T} \eta \right) \right] \tag{4.39}$$

where, α_{an} is the anodic; α_{ca} is the cathodic charge transfer coefficient, η denotes the overpotential, and i_0 represents the exchange current density as,

$$i_0 = F k_{ca}^{\alpha_{an}} k_{an}^{\alpha_{ca}} c_s^{\alpha_{ca}} c_l^{\alpha_{an}} (c_{s,ref} - c_s)^{\alpha_{an}} \tag{4.40}$$

In this equation, k_{an} denotes the anodic rate constant whereas k_{ca} indicates the cathodic rate constant. The overpotential term can be evaluated from Eq. (4.41),

$$\eta = \phi_s - \phi_l - E \tag{4.41}$$

where E defines the equilibrium potential of the cell.

4.3.2 Thermal Modeling

The thermal model uses the general heat diffusion equation (Eq. 3.9) and can predict the temperature variation of the cell during the discharging processes once the heat generation within the cell is specified. In Li-ion batteries, the generated heat is mainly composed of Joule heating, overpotential heating, and entropic heating within the cell. Hence, the volumetric heat generations due to these factors are evaluated and added to the heat diffusion equation.

The model geometry is created with three main parts; a mandrel, active battery material, and a shell. The electrical, chemical, and thermal properties of these components are separately added to the model. The convective and radiative heat transfers are defined on the cell's surface. The convective heat transfer is

calculated using the Churchill-Chu correlation, as stated in Eq. (3.11). Eventually, the heat source within the battery is calculated by using Eqs. (4.42) - (4.45) below.

In the thermal model, the volumetric Joule heating rate due to the charge transfer relations is defined in Eq. (4.42).

$$\dot{Q}_J = \sigma_{s,eff}\frac{\partial^2\phi_s}{\partial x^2} + \left[\sigma_{l,eff}\frac{\partial\phi_l}{\partial x} + 2R_u T\sigma_{l,eff}\frac{1-t_+}{F}\frac{\partial \ln c_l}{\partial x}\left(1+\frac{\partial \ln f}{\partial \ln c_l}\right)\right]\frac{\partial\phi_l}{\partial x} = 0 \tag{4.42}$$

The irreversible volumetric heat generation rate is related to the overpotential term and can be determined with the following equation [12],

$$\dot{Q}_{IR} = J_{Li}\eta \tag{4.43}$$

whereas the reversible volumetric heat generation rate is the function of temperature derivative of the equilibrium potential and expressed in Eq. (4.44) [12].

$$\dot{Q}_{REV} = J_{Li}T\frac{\partial E}{\partial T} \tag{4.44}$$

Therefore, the volumetric electrochemical heat generation rate can be evaluated by Eq. (4.45).

$$\dot{Q}_{ec} = \dot{Q}_J + \dot{Q}_{IR} + \dot{Q}_{REV} \tag{4.45}$$

4.3.3. Electrochemical-Thermal Model and Experimental Results

4.3.3.1. Test and Simulation Results of a Discharging Cell at 20°C

An NCR18650b cylindrical Li-ion cell was fully charged as an initial condition, and the thermal and electrical behavior of the cell was observed during 0.5, 1, and 1.5C rate discharging processes at 20°C temperature.

The voltage predictions are presented with the experimental results in Figure 4.13. The coupled model can predict the voltage variation of the cell within a narrow margin of error for each discharging process.

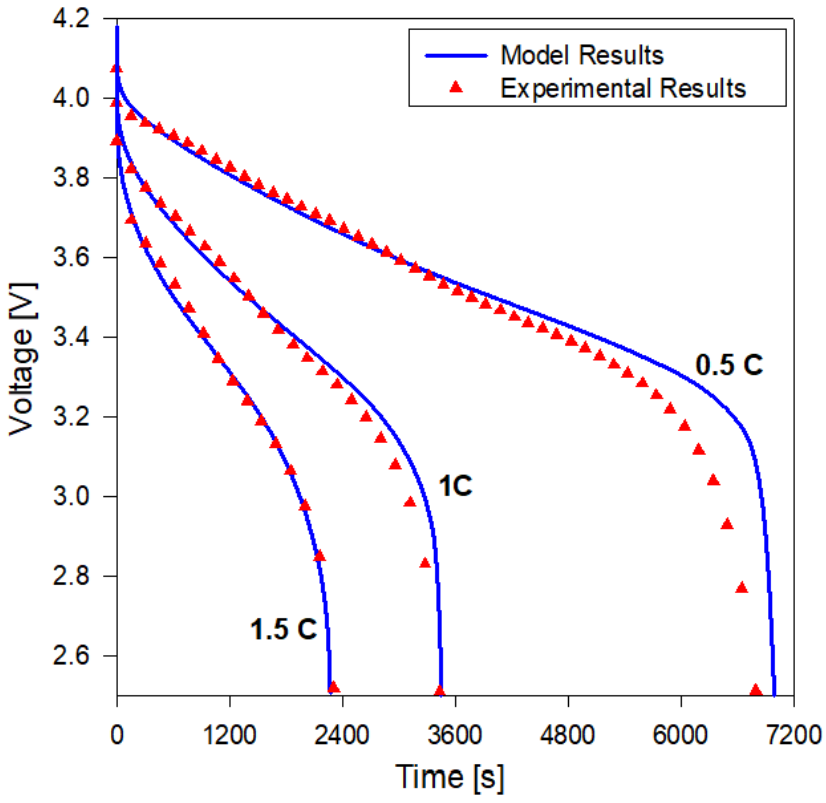

Figure 4.13. Model and experimental voltage variations of the Li-ion cell during discharging processes at 20°C.

The maximum errors for the voltage predictions were obtained as 0.56 V, 0.22 V, and 0.12 V during the 0.5, 1, and 1.5C rate discharging processes, respectively.

The model predictions mostly follow the experimental data until the last stages of the discharge where a sharp voltage decrement occurs as a result of the concentration overpotential losses within the Li-ion cell. Nevertheless, the model results are reasonable considering the entire process since the maximum RMS error is 0.11 V for the 0.5C rate discharging.

The temperature differences between the ambient and the cell surface were acquired during the 0.5, 1, and 1.5C rate discharging processes. The model results were compared with the experimental results, as presented in Figure 4.14.

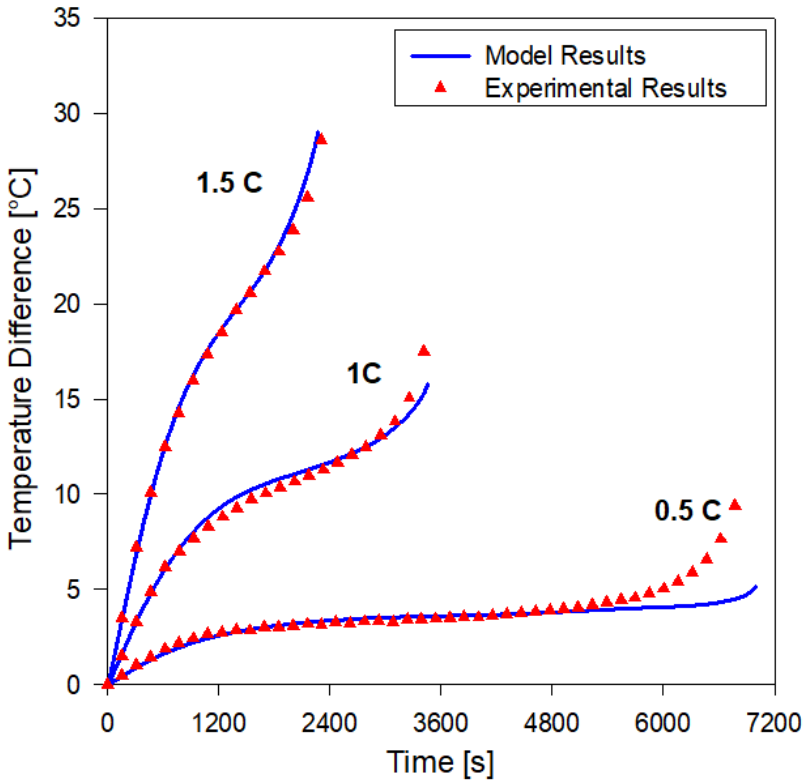

Figure 4.14. Surface temperature change of the Li-ion cell during various discharging processes at 20°C.

The model results follow the same trend for 1, and 1.5C rate discharging processes. The temperature predictions are also reasonable for 0.5C discharging up to the point where the cell voltage drops sharper. The difference in voltage predictions adversely affects the simulated temperature profile of the 0.5C rate

discharging cell. In this case, slight voltage difference towards the end of the discharging process causes a relatively large temperature deviation. On the other hand, the RMS errors were obtained as 0.92, 0.57, and 0.50°C for the 0.5, 1, and 0.5C rate discharging processes, respectively.

Figures 4.15, 4.16, and 4.17 present the temperature distribution within the cell after the 0.5, 1, and 1.5C rate discharging processes, respectively. The multi-slice geometry of the cell is also displayed in the figures so that the temperature variation within the cell can be observed in detail.

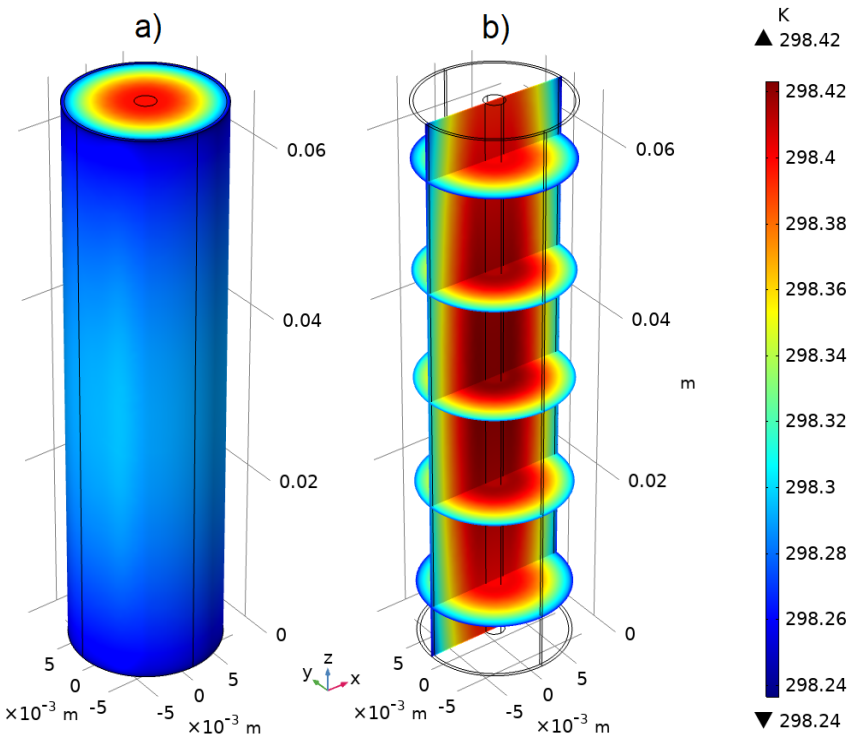

Figure 4.15. 3-D Temperature distributions a) on the surface of the cell, b) within the cell, after it is completely discharged at 0.5C rate.

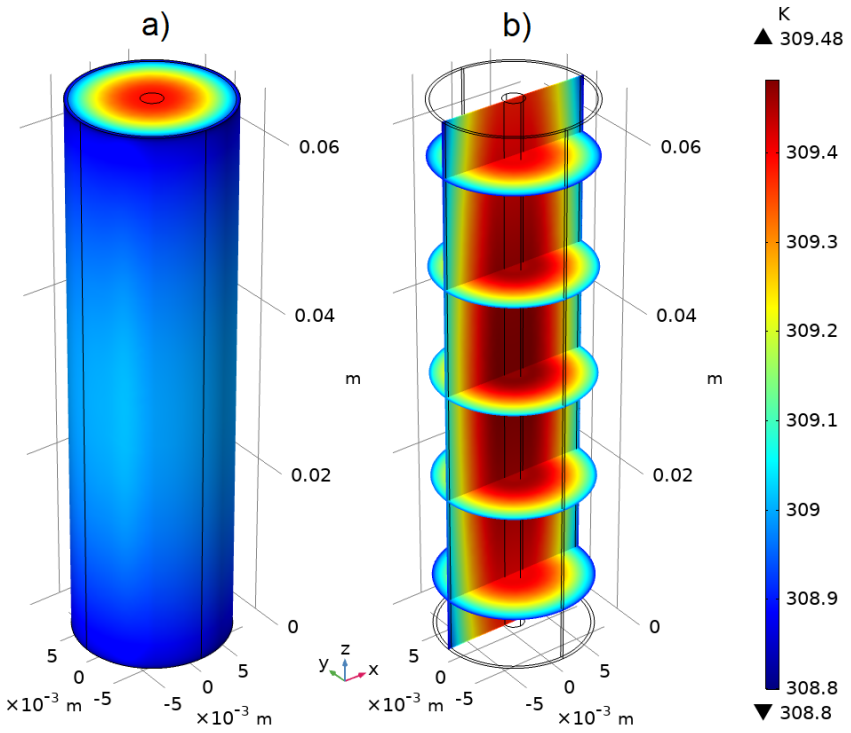

Figure 4.16. 3-D Temperature distributions, a) on the surface of the cell, b) within the cell, after it is completely discharged at 1C rate.

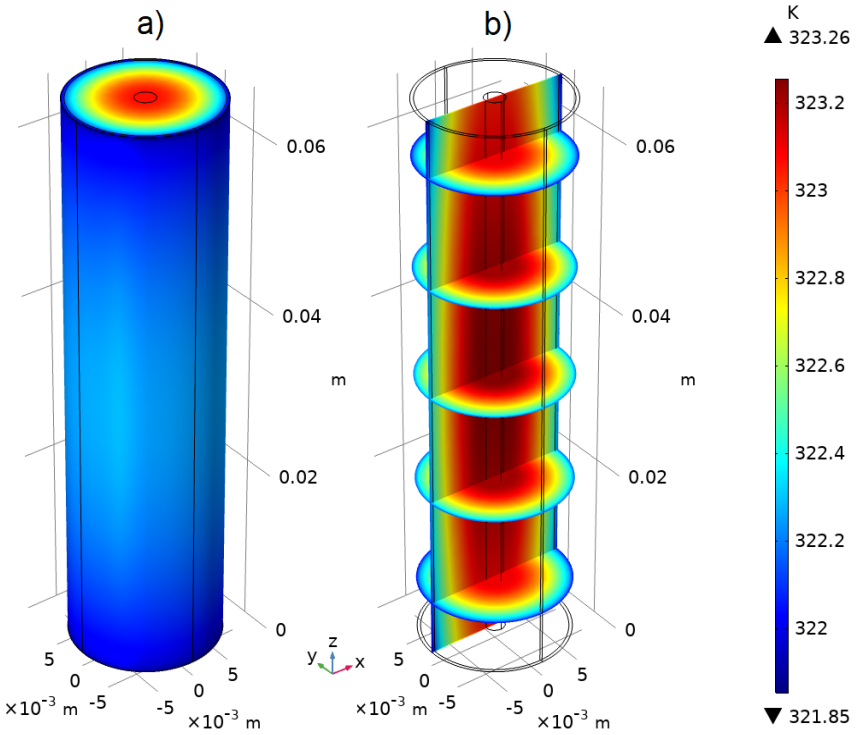

Figure 4.17. 3-D Temperature distributions a) on the surface of the cell, b) within the cell, after it is completely discharged at 1.5C rate.

The maximum temperature difference within the cell was obtained as 0.18, 0.68, and 1.41°C after discharging at 0.5, 1, and 1.5C rates, respectively. The temperature difference increases as the applied current increases, as expected. The maximum temperature is observed inside the Nickel mandrel in each case. The 3-D model results indicate that the lumped modeling method could apply to cases with relatively low discharge currents to the cell.

Nylon is also used as a mandrel in the electrochemical-thermal model in order to investigate the effects of the mandrel material on the thermal behavior of the Li-ion cell. The results with a Nylon mandrel after a 1.5C rate discharging process were presented in Figure 4.18 for the cylindrical and multi-slice geometry of the cell.

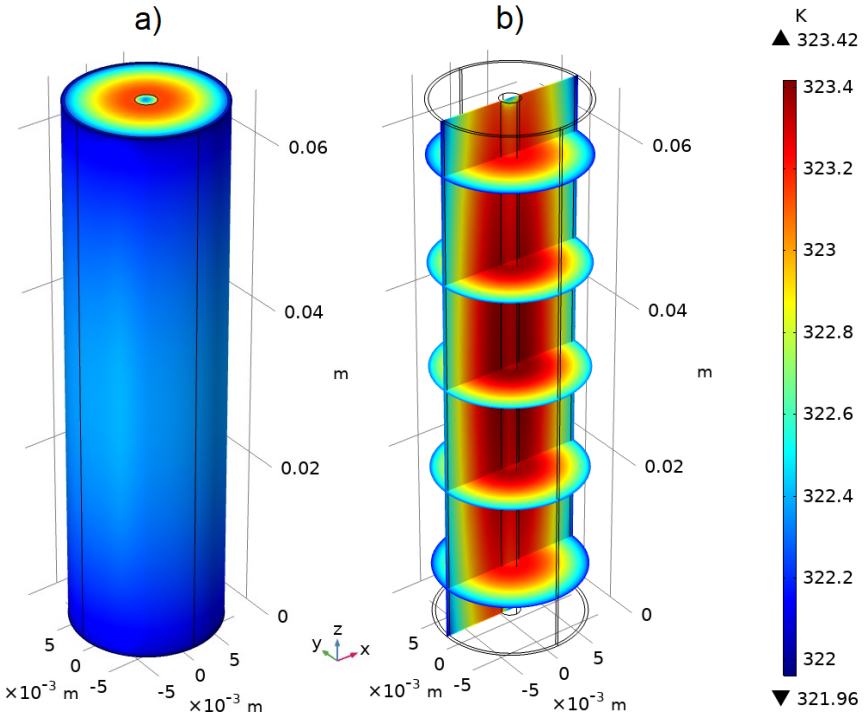

Figure 4.18. 3-D Temperature distributions for the a) cylindrical and b) multi-slice cell geometries after a 1.5C rate discharging of a Nylon mandrel cell.

Comparison of Figures 4.17 and 4.18 show that changing the material of the mandrel alters the temperature variation within the cell. The maximum temperature within the cell can now be observed in the active material around the mandrel in the latter case. Furthermore, as can be seen in Figure 4.19, there is a small cold region at the top of the mandrel. The maximum temperature of the cell is increased by 0.16°C using nylon as a mandrel. Consequently, a comparable cell average surface temperature was obtained, 322.3 K for the nylon and 321.87 K for the nickel foil mandrel cell.

4.3.3.2. Test and Simulation Results of a Discharging Cell at 50°C

The discharge experiments were also performed inside the pre-heated oven at 50°C operating temperatures. Simulations were carried out and the voltage and temperature variations during the 0.5, 1, and 1.5C rate discharging processes were predicted using the electrochemical-thermal model and presented with the experimental results in Figure 4.19 and 4.20.

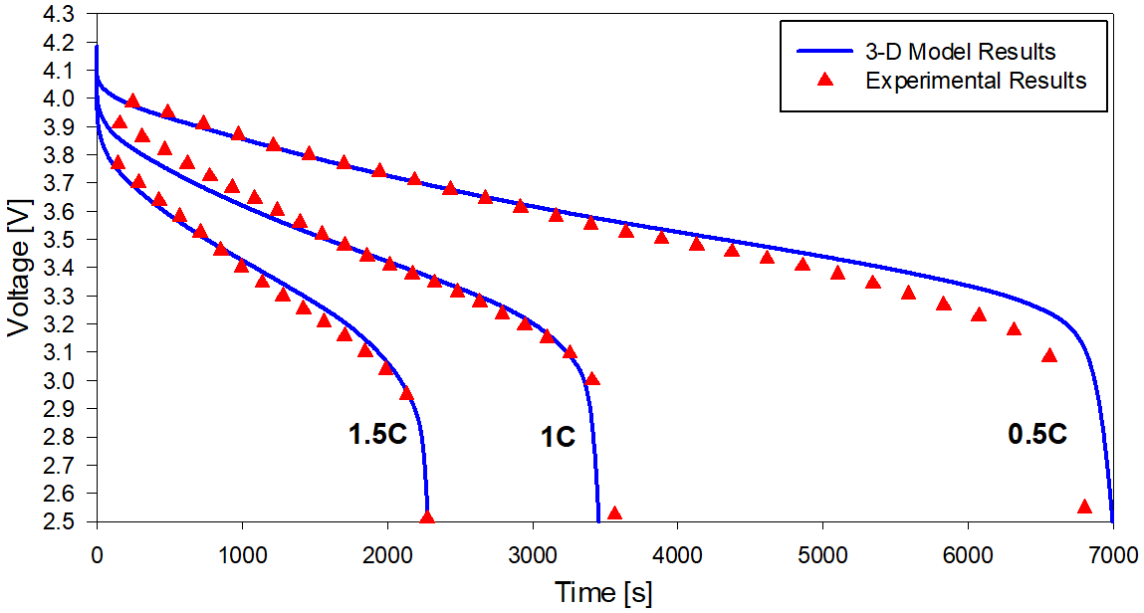

Figure 4.19. Voltage variation of the cell during 0.5, 1 and 1.5C rate discharging processes at 50°C operating temperature.

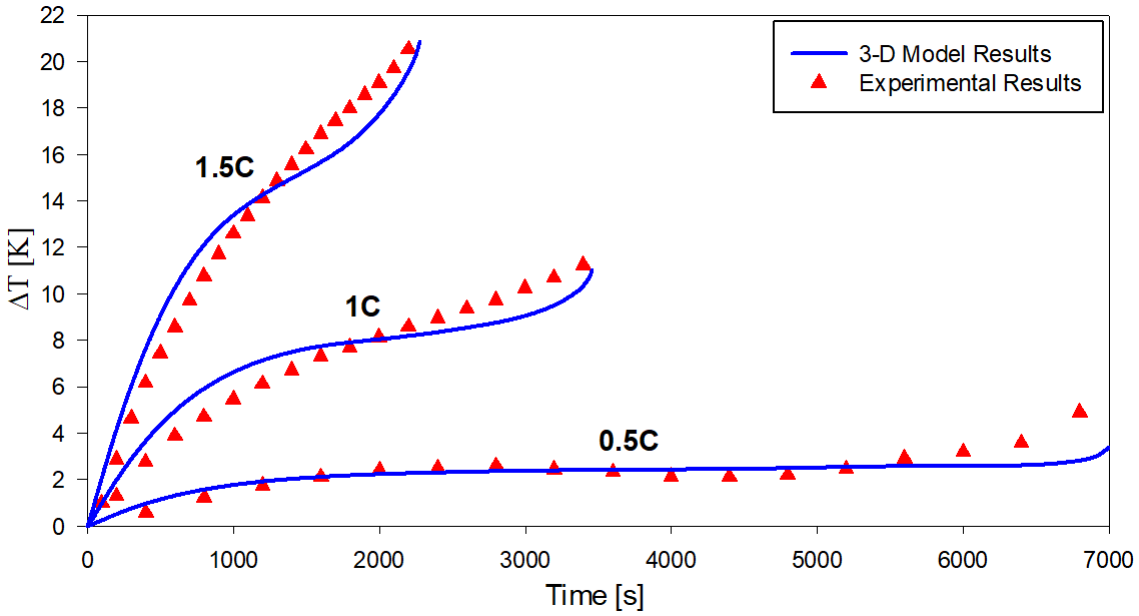

Figure 4.20. Temperature difference between the ambient and the surface of the cell during 0.5, 1 and 1.5C rate discharging processes at 50°C operating temperature.

The results show that the model is acceptable for predicting the voltage and temperature variations within the cell at 50°C. The voltage and temperature profiles follow similar trends during 20 and 50°C discharge. However, the cell temperature measured lower compared to the 20°C cases during each discharging process at 50°C. High ambient temperature also decreases the sharpness of the temperature increase towards the end of the discharging processes. However, it should be considered that the SoH and the capacity of the cell significantly decrease as the cell is exposed to elevated temperatures.

5. MODELING THE THERMAL ABUSE OF THE LI-ION BATTERIES

Li-ion batteries generate heat during normal operating conditions. Bernardi et al. [12] developed a method to evaluate the produced heat due to electrochemical reactions within the battery. On the other hand, various exothermic side reactions may be triggered inside a cell as the temperature rises during abusive operating conditions such as heating, overcharging, overdischarging, nail penetration, and external or internal short circuits. These reactions also continue to increase the temperature further if the heat dissipation rate is less than the heat generation rate and may lead to dangerous circumstances that possibly end up with the explosion of the cells [21].

An extensive thermal model should be useful to predict the thermal characteristics of the batteries under both normal and abusive operating conditions. Therefore, we can re-arrange the volumetric heat generation rates for the battery exposed to abusive behavior,

$$\dot{Q}_c = \dot{Q}_{ec} + \dot{Q}_{abuse} \tag{5.1}$$

where the first term on the right-hand side gives the volumetric electrochemical heat generation rate from Bernardi's equation and the second term is the abusive volumetric heat generation rate that can be represented by temperature-dependent Arrhenius-type equations. The components that constitute the battery can decompose at elevated temperatures. The battery releases heat during the decomposition reactions. In the following section, their contributions to total heat generation will be expressed in detail.

5.1. Heat Generation During the Abuse Condition

The main exothermic side reactions should be specified to represent the cell's TR behavior. In simulations, four main exothermic side reactions are usually described as [72],

- SEI layer decomposition.
- Positive electrode solvent reaction.
- Negative electrode solvent reaction.
- Electrolyte decomposition.

Therefore, the total volumetric heat generation during these exothermic reactions can be evaluated by adding the heat released during SEI ($\dot{Q}_{sei}$) decomposition, positive electrode solvent reaction ($\dot{Q}_{pe}$), negative electrode solvent reaction ($\dot{Q}_{ne}$), and electrolyte decomposition ($\dot{Q}_{ele}$), as stated in Eq. (5.2).

$$\dot{Q}_{abuse} = \dot{Q}_{sei} + \dot{Q}_{pe} + \dot{Q}_{ne} + \dot{Q}_{ele} \tag{5.2}$$

Each heat source within the cell is modeled using the Arrhenius-type temperature-dependent equations. Abuse model parameters were obtained from various studies and are presented in Table 5.1. In this table, A represents the frequency factor, E is the activation energy, H is the reaction heat, c is the reacting species content, a is the conversion degree of the positive active material, m is the reaction order, t is the SEI layer thickness, and W is the specific mass of carbon in the component.

Table 5.1. Abuse model parameters.

Parameter	Unit	Value	Reference
A_{sei}	1/s	1.667e15	[82, 124]

$E_{a,sei}$	J/mol	1.3508e5	[82, 124]
H_{sei}	J/kg	2.57e5	[82, 124, 125]
c_{sei0}	-	0.15	[82, 124]
m_{sei}	-	1	[82, 124]
t_{sei0}	-	0.15	[82, 124]
A_{ne}	1/s	2.5e13	[82, 124]
$E_{a,ne}$	J/mol	1.3508e5	[82, 124]
H_{ne}	J/kg	1.714e6	[82, 124, 125]
c_{ne0}	-	0.75	[82, 124]
m_{ne}	-	1	[82, 124]
W_{ne}	kg/m^3	1.39e3	[82]
A_{pe}	1/s	6.667e13	[82, 124]
$E_{a,pe}$	J/mol	1.396e5	[82]
H_{pe}	J/kg	3.14e5	[82, 124, 125]
a_0	-	0.04	[82, 124]
m_{pe}	-	1	[82, 124]
W_{pe}	kg/m^3	1.39e3	[82]
A_{ele}	1/s	5.14e25	[82, 125]
$E_{a,ele}$	J/mol	2.74e5	[82, 125]
H_{ele}	J/kg	1.55e5	[82, 125]
c_{ele0}	-	1	[82, 124]

m_{ele}	-	1	[82]
W_{ele}	kg/m^3	5e2	[82]

5.1.1 Volumetric Heat Generation due to the Decomposition of the SEI Layer

As reported in many studies, the SEI layer has various metastable components, and its integrity starts to decompose around 90°C. On the other hand, the decomposition temperature may vary according to the cell type. The reaction rate of the decomposition is defined as;

$$R_{sei} = A_{sei} \exp\left[-\frac{E_{a,sei}}{R_u T}\right] c_{sei}^{\,m_{sei}} \tag{5.3}$$

where R_{sei} (1/s) is the rate constant of the decomposition of the SEI layer, A_{sei} (1/s) is the frequency factor for the SEI decomposition, $E_{a,sei}$ (J/mol) is the reaction activation energy, R_u (J/mol.K) is the universal gas constant, T (K) is the cell temperature, c_{sei} is the dimensionless concentration of the reacting species in the SEI layer, and m_{sei} is the reaction order. During the reaction, the rate of change of the dimensionless concentration can be expressed using Eq. (5.4).

$$\frac{dc_{sei}}{dt} = -R_{sei} \tag{5.4}$$

Therefore, the volumetric heat generation rate during the reaction can be evaluated by using,

$$\dot{Q}_{sei} = H_{sei} R_{sei} W_{ne} \tag{5.5}$$

where H_{sei} (J/kg) is the released specific heat during the reaction, and W_{ne} (kg/m^3) is the specific mass of the carbon content in negative electrode.

5.1.2 Volumetric Heat Generation due to the Reactions Between the Negative Electrode and Solvent

The exothermic side reaction between the intercalated lithium in the negative electrode and the solvent starts when the cell temperature exceeds approximately 120°C. The rate of this reaction can be defined as,

$$R_{ne} = A_{ne} \exp\left[-\frac{t_{sei}}{t_{sei,ref}}\right] \exp\left[-\frac{E_{a,ne}}{R_u T}\right] c_{ne}^{\ m_{ne}} \tag{5.6}$$

where R_{ne} (1/s) is the rate constant of the reaction between the negative electrode and solvent, A_{ne} (1/s) is the frequency factor for the negative electrode-solvent reaction, $E_{a,ne}$ (J/mol) is the reaction activation energy, c_{ne} is the dimensionless concentration of the Li-ion in negative electrode, and m_{ne} is the reaction order. During the reaction, the rate of change of the dimensionless lithium concentration in negative electrode can be expressed in Eq. (5.7).

$$-\frac{dt_{sei}}{dt} = \frac{dc_{ne}}{dt} = -R_{ne} \tag{5.7}$$

Therefore, the volumetric heat generation rate during the reaction can be evaluated by using,

$$\dot{Q}_{ne} = H_{ne} R_{ne} W_{ne} \tag{5.8}$$

where H_{ne} (J/kg) is the released specific heat during the negative electrode-solvent reaction, and W_{ne} (kg/m^3) is the specific mass of the carbon content in negative electrode.

5.1.3 Volumetric Heat Generation due to the Reaction Between the Positive Electrode and Solvent

The exothermic side reaction between the positive active material and the solvent lead to the decomposition of the active material that emits oxygen during the reaction. The reaction starts above 170°C, and the rate of the reaction can be defined as,

$$R_{pe} = A_{pe} a^{m_{pe}} (1-a)^{m_{pe}} \exp\left[-\frac{E_{a,pe}}{R_u T}\right] \tag{5.9}$$

where R_{pe} (1/s) is the rate constant of the reaction between the positive electrode and solvent, A_{pe} (1/s) is the frequency factor for the positive electrode-solvent reaction, $E_{a,pe}$ (J/mol) is the reaction activation energy, a is the conversion degree of the positive active material, and m_{pe} is the reaction order. During the reaction, the rate of change of the degree of conversion can be expressed in Eq. (5.10).

$$\frac{da}{dt} = R_{pe} \tag{5.10}$$

Therefore, the volumetric heat generation rate during the reaction can be evaluated by using,

$$\dot{Q}_{pe} = H_{pe} R_{pe} W_p \tag{5.11}$$

where H_{pe} (J/kg) is the released specific heat during the positive electrode-solvent reaction, and W_p (kg/m^3) is the specific mass of the carbon content in positive electrode.

5.1.4. Volumetric Heat Generation due to the Electrolyte Decomposition

Consequently, the electrolyte decomposes above 200°C, and the rate of this reaction can be defined as,

$$R_{ele} = A_{ele} \exp\left[-\frac{E_{a,ele}}{R_u T}\right] c_{ele}^{\,m_{ele}} \tag{5.12}$$

where R_{ele} (1/s) is the rate constant of the electrolyte decomposition reaction, A_{ele} (1/s) is the frequency factor, $E_{a,ele}$ (J/mol) is the reaction activation energy, c_{ele} is the dimensionless concentration of the reacting species during the electrolyte decomposition reaction, and m_{ele} is the reaction order. During the reaction, the rate of change of the dimensionless concentration of the electrolyte can be expressed in Eq. (5.13).

$$\frac{dc_{ele}}{dt} = -R_{ele} \tag{5.13}$$

Therefore, the volumetric heat generation rate during the reaction can be evaluated by using,

$$\dot{Q}_{ele} = H_{ele} R_{ele} W_{ele} \tag{5.14}$$

where H_{ele} (J/kg) is the released specific heat during the electrolyte decomposition reaction, and W_{ele} (kg/m^3) is the specific mass of the carbon content in electrolyte.

5.2. Modeling Procedure of Thermal Abuse

The amount of heat generation due to exothermic reactions resulting from thermal abuse can be implemented in 1-D electrochemical and 3-D thermal coupled

model. The ordinary differential Arrhenius equations are used in a domain or global form for modeling the abuse behavior of the battery. In domain form, the equations are used in the electrochemical or thermal model interfaces, whereas in global form, the equations are independent of the models. All abuse modeling approaches can be followed in Figure 5.1.

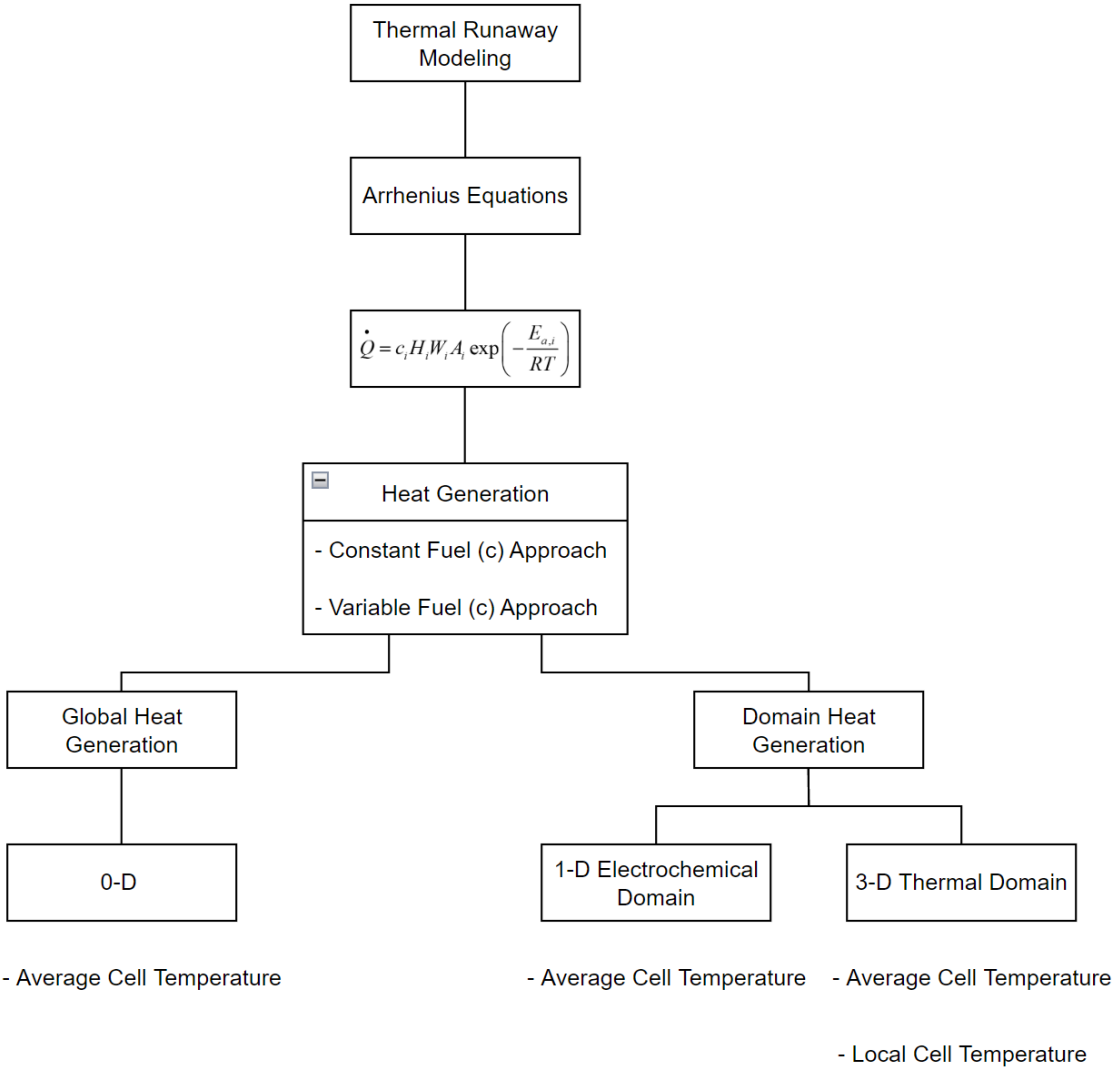

Figure 5.1. Modeling procedures of the thermal abuse of Li-ion battery.

The Arrhenius equations involve the dimensionless concentration terms which normally vary with respect to the reaction rate of that component. On the other hand, Melcher et al. [72, 84] developed a method called constant fuel assumption and assumed the dimensionless concentration terms as constant during the reactions, which simplifies the simulations and eliminates the solution of the

ODEs. Both constant and variable fuel approaches can be used in global or domain form.

In domain form, two approaches can be followed; ODEs can be applied to the 1-D electrochemical domain or 3-D thermal domain. In the first method, Arrhenius equations should be used considering the average cell temperature since the electrochemical model is in one direction. In the second approach, local and average cell temperatures can be implemented into the abuse model. However, note that the model predicts the volumetric heat generation in one dimension, so the 3-D modeling does not apply to this approach.

In other respects, in global form, the abuse model is assumed to be 0-D, and the Arrhenius equations should be solved using the average cell temperature. Apart from other presented methods, this approach uses the ODEs and Arrhenius equations independent from any domain.

5.3. Abuse Tests and Simulation Results

In this part of the study, film heater and oven experiments were performed to investigate the Li-ion cell's thermal behavior under elevated ambient temperatures. Tested cells are listed in Table 5.2 also shows the test conditions and the initial capacity values of the Li-ion cells. Note that each cell was exposed to at least 3 standard charge and discharge tests before the abusive experiments in order to form the SEI layer on the anode side, which affects the thermal behavior of the cell according to the previous studies in the literature. The initial capacity of the tested cells varies from 2947 to 3263 mAh stating the very first available discharged power until the cell cut-off voltage.

Table 5.2. Film heater and oven test conditions.

Film Heater Tests			
Initial Capacity (mAh)	Film Heater Power (W)	SoC	Applied Current
3082	30 W	0	-
3139	30 W	0	-
3122	30 W	0.5	-
3087	30 W	1	-
3146	30 W	1	-
3096	30 W	1	1.5C
3118	30 W	1	1.5C
Oven Tests			
Initial Capacity (mAh)	Oven Temperature (°C)	SoC	Applied Current
2947	185°C	0	-
3247	185°C	0	-
2986	190°C	0	-
3263	200°C	0	-
3001	200°C	0	-
3155	90°C	1	1C
3224	95°C	1	-
3174	110°C	1	-
3215	115°C	1	-
3171	155°C	1	-
3203	155°C	1	-
3215	155°C	1	-
3218	175°C	1	-
3082	180°C	1	-
3131	185°C	1	-
3112	185°C	1	-

5.3.1. Film Heater Tests and Simulation Results

In this part of the study, the heating of the Li-ion batteries was sustained by the film heaters. Film heater tests were conducted for the Li-ion batteries at various SoC values such as 0, 0.5, and 1. In these tests, a T-type thermocouple was located at the mid-height of the cell with heat-resistant tape. Unlike oven tests, the heat-resistant tape covered the entire cell in order to stick the film heater to the battery's lateral area. The numerical and experimental film heater tests were conducted under abnormal thermal operating conditions are summarized in Table 5.3.

Table 5.3. The performed film heater studies under thermal abnormal operating conditions.

Study	C-Rate	Initial SoC	Experimental	Model
Heating by a film heater at 30W	-	0	+	+
Heating by a film heater at 30W	-	0.5	+	-
Heating by a film heater at 30W	-	1	+	+
Heating by a film heater at 30W	1.5C	1	+	+

5.3.1.1. Film Heater Test Results of the Li-ion Batteries at Various SoC Values

The film heater tests were conducted to investigate the thermal behavior of the Li-ion cell at 0, 0.5, and 1 initial SoC values. No current was allowed to flow through the Li-ion battery during these tests. The experiments at SoC=0.5 and SoC=1 resulted in a vast explosion and local fire around the Li-ion cell. Thus, the results in these cases were shown until the TR. The experimental results of the film heater tests were compared at various SoC values in Figure 5.2.

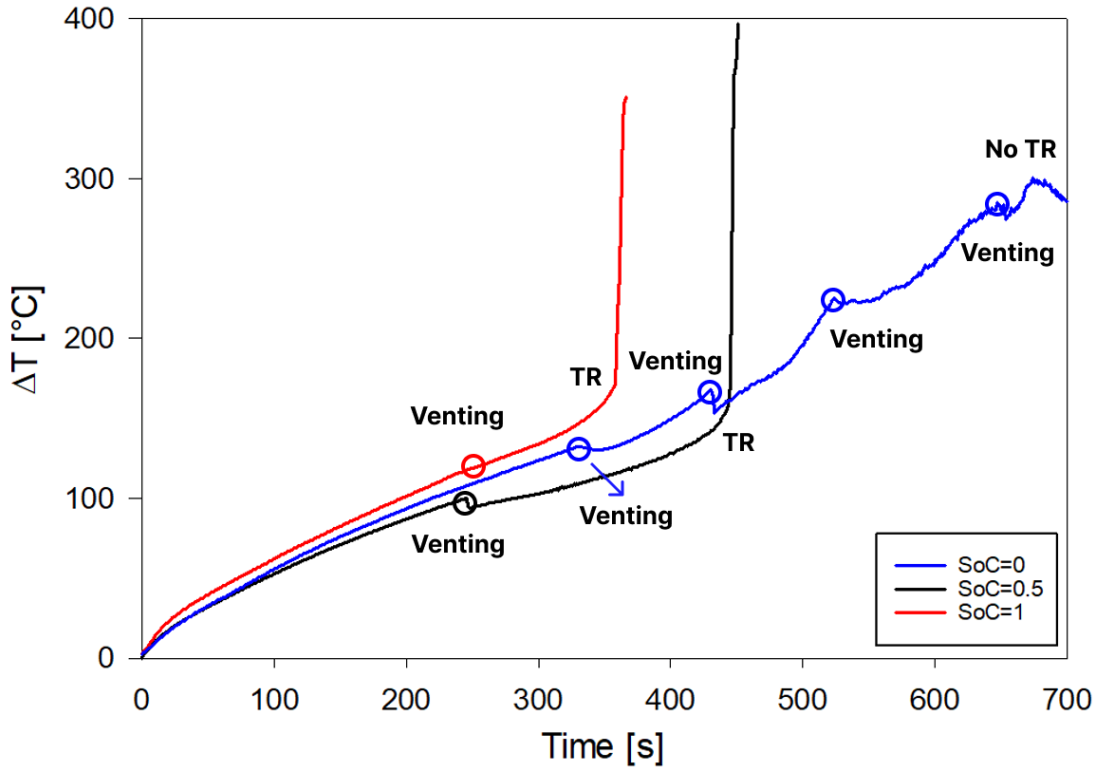

Figure 5.2. Variation of the temperature differences between the ambient and the surface of the cell during the film heater tests of a Li-ion cell at SoC= 0, 0.5, and 1.

The results of the film heater experiments indicate that the cell's SoC value significantly affects the thermal, hence the TR behavior of the Li-ion batteries during the heating process. The cells at 0.5 and 1 SoC went into a TR after experiencing a venting process. The venting process is defined as the release of gasses due to exothermic side reactions to reduce the possibility of the thermal runaway. The ventilation process did not decrease the surface temperature of the cell at 1 SoC apart from the other cases. In addition, multiple venting processes appeared during the heating of a fully discharged cell. In this case, the cell's surface temperature increased more than 1°C/s during the heating, but the venting processes possibly prevented the cell against the TR. Therefore, the temperature difference between the ambient and the cell's surface did not exceed 300°C at 0 SoC. However, higher surface temperatures were reached in other presented cases due to explosion and fire around the Li-ion cell after TR. The

film heater test of the fully charged Li-ion cell was recorded, and the frames of critical moments are presented in Figure 5.3.

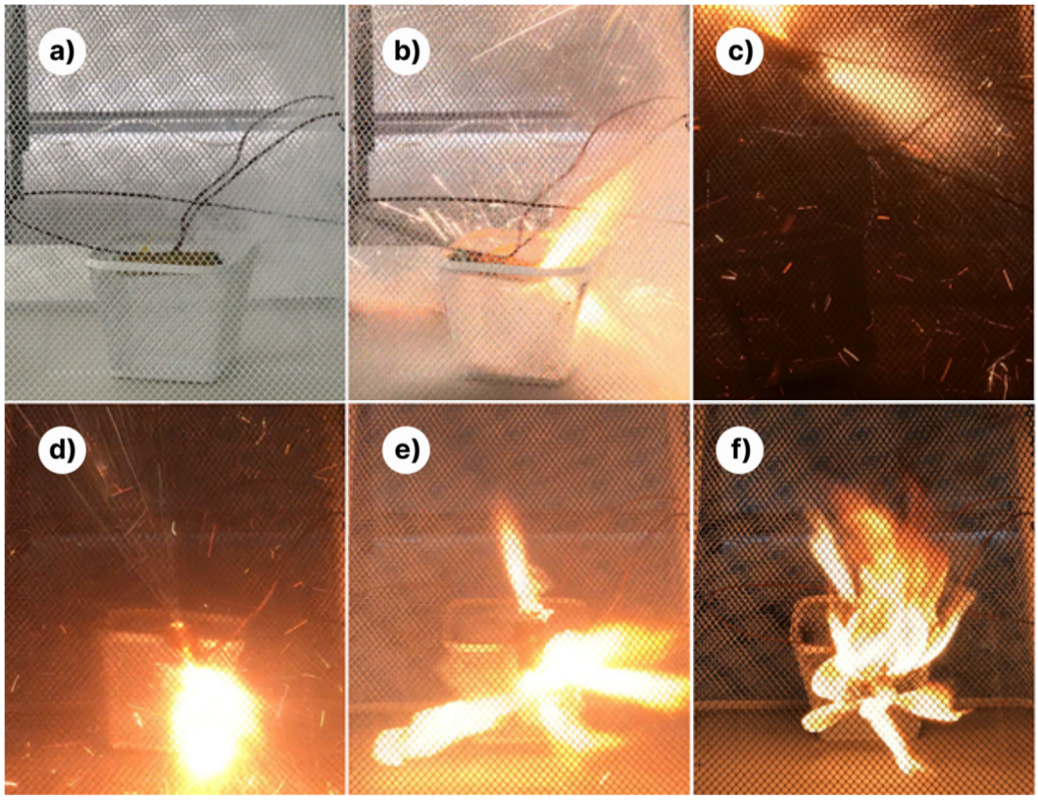

Figure 5.3. The physical condition of the Li-ion battery during the heating procedure by the film heater at 30 W.

Figure 5.3a shows the ventilation of the gasses from the top of the cell; Figure 5.3b illustrates the ignition condition, which started from the top part of the cell; Figure 5.3c and Figure 5.3d display that the battery was moved after the explosion, and finally Figure 5.3e and Figure 5.3f demonstrate that the fire has spread to the bottom part and surrounded the entire cell, respectively.

5.3.1.2. Film Heater Simulation Results

In this part, the simulations were performed for the film heater tests at 0 and 1 SoC cases. The abuse model parameters referenced from the previous studies [82, 124, 125] are given for the Li-ion batteries at 1 SoC value but were still utilized for both 0 and 1 SoC conditions for investigation purposes.

During the film heater tests, the voltage and current values of the power supply were adjusted to get 30 W of power. However, there are some issues regarding transmitting the entire 30 W to the cell. There are losses to the environment since the system is not isolated. Besides, these losses can be influenced by the tightness of the film heater. Therefore, the net heater power applied on the battery for the simulations is set such that the resulting surface temperature variation with time matches that of the experimental surface temperatures. The numerical and experimental results of the film heater tests are presented in Figure 5.4.

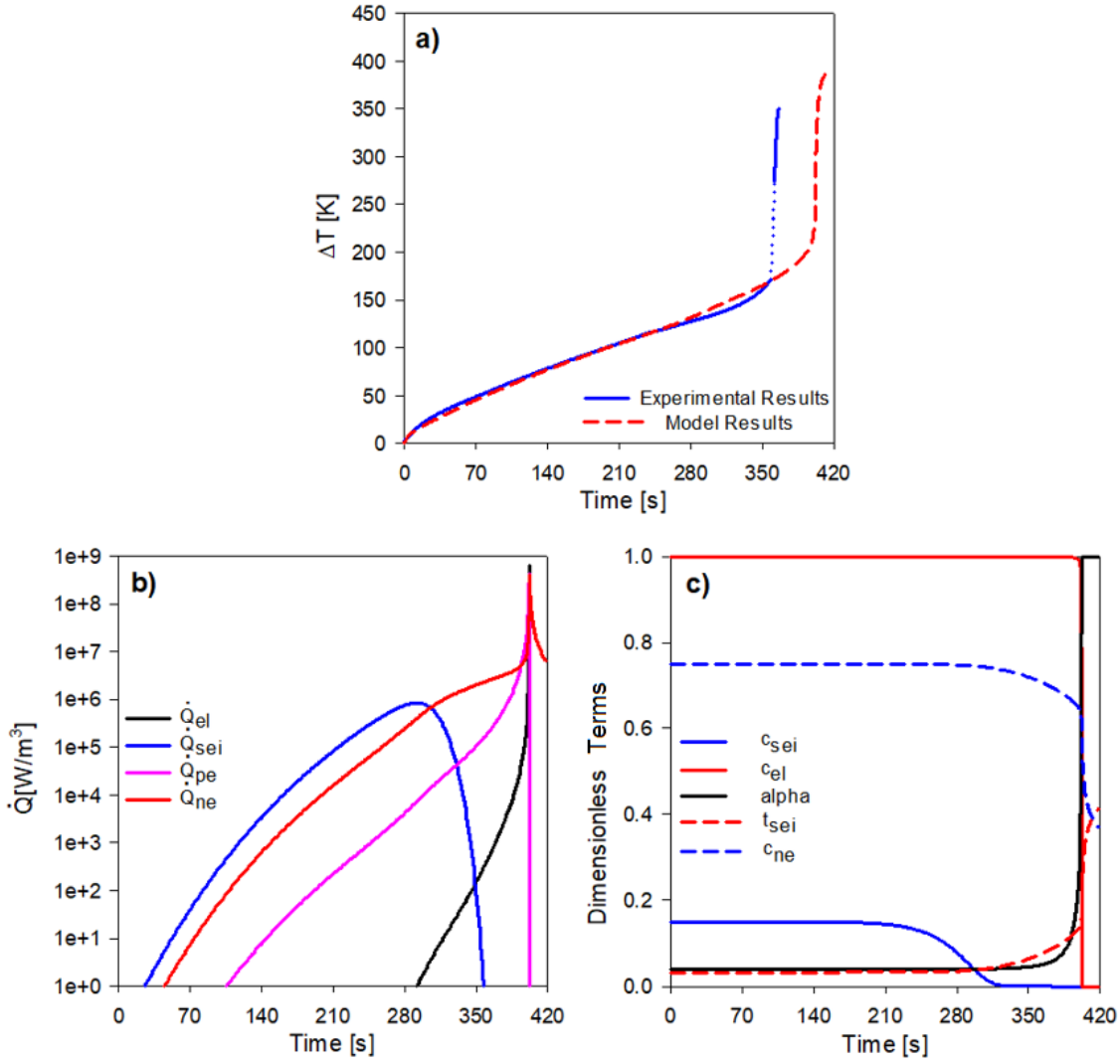

Figure 5.4. Variation of the a) surface temperature difference, b) volumetric heat generation rates, and c) dimensionless concentration terms during the 30 W heating process of a Li-ion cell at 1 SoC.

The thermal abuse model can predict the TR initiation time within the approximate 10% margin of error, as can be followed in Figure 5.4a. Figure 5.4b presents different volumetric heat generation terms due to the decomposition reactions within the Li-ion battery. The order of these reactions can be followed from the figure as the SEI layer, the negative electrode, the positive electrode, and the electrolyte. The SEI layer decomposes first but contributes less to heat generation than the other components.

On the other hand, other exothermic reactions increase the heat generation within the cell till the TR condition. The most effective reaction in terms of the generated heat is observed as the decomposition reaction between the negative electrode and the solvent. The variation of the dimensionless concentration terms is also presented in Figure 5.4c. The figure indicates that the concentrations in the SEI layer and the electrolyte are consumed during the heating process. In addition, the dimensionless concentration of the Li-ion in the negative electrode decreases as the conversion degree of the positive active material and the SEI layer thickness increases towards the end of the experiment.

The simulations were also carried out for the film heater test of a Li-ion battery at 0 SoC condition and the model results were compared with the experimental results in Figure 5.5.

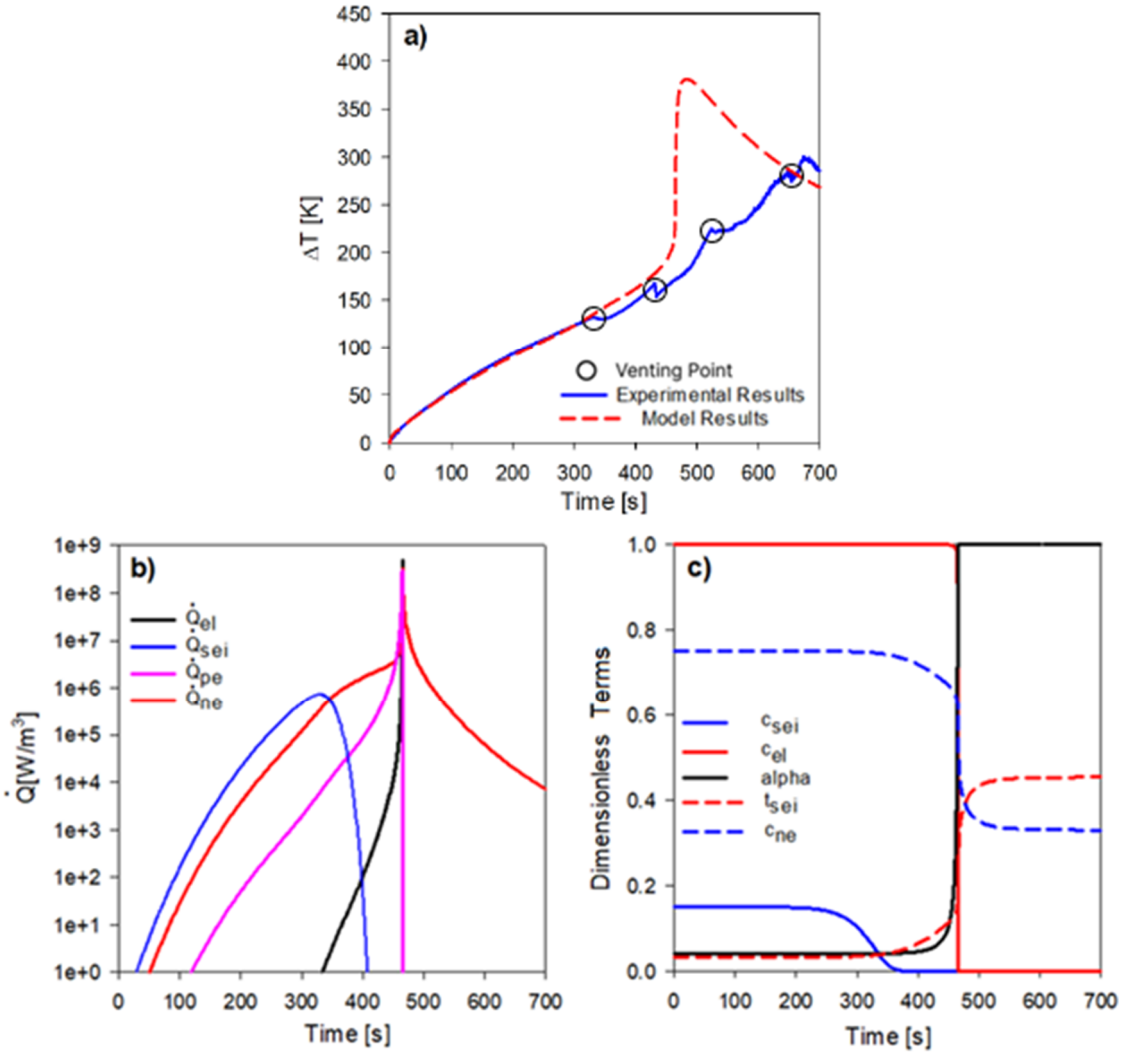

Figure 5.5. Variation of the a) surface temperature difference, b) volumetric heat generation rates, and c) dimensionless concentration terms during the 30 W heating process of a Li-ion cell at 0 SoC.

The thermal abuse model can accurately predict the surface temperature variation until the first ventilation point, which can be seen in Figure 5.5a. However, the simulated surface temperature continues to rise to the TR since the model cannot predict the venting behavior of the cell. The TR initiation time was predicted with less than a 2.5% error in simulation, but multiple venting processes possibly prevented the cell against the TR condition in the experiment. Figures 5.5b and 5.5c present the variations of the volumetric heat generation and the dimensionless terms, respectively. The simulation results in these follow the same trend as previously presented in Figure 5.4.

Subsequently, the film heater test was conducted during a 1.5C rate discharging process. The experiment ended with an explosion and local fire around the Li-ion cell. Besides, the explosion affects the thermocouple, so the results are shown until the TR. Temperature and voltage variations of the Li-ion cell are presented in Figure 5.6.

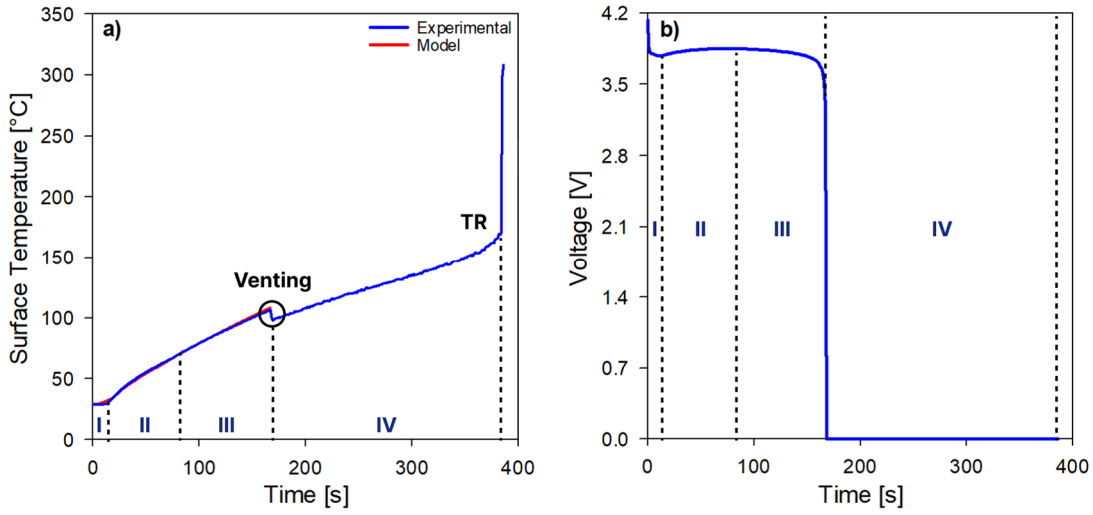

Figure 5.6. Surface temperature (a), and voltage (b) variation of the Li-ion cell during the 1.5C rate discharging process at 30W.

The effect of discharging on the thermal behavior of a heated cell is presented in Figure 5.6. The temperature variation of the cell was observed similar compared to the SoC=1 case since the discharge ended at the ventilation point. The abuse model accurately predicted the surface temperature until the venting process.

The heating experiment was divided into four different regions. The first region indicates the condition before the heating process. Therefore, the voltage value of the cell decreases during the discharging process in this region. The surface temperature of the cell starts to increase in the second region, and the voltage value of the cell slowly increases despite the discharging process. The discharging behavior returns after the cell surface reaches 71°C, and the voltage decreases again until the ventilation point in region 3. After the venting process,

the discharge finishes, and the cell voltage drops to zero. The battery continues to heat up until it goes into TR in the fourth region.

5.3.2. Oven Test Results

Oven tests were performed for both fully charged and discharged cells. In these tests, a thermocouple was located at the cell mid-height with heat-resistant tape. In addition, another thermocouple was swinging in the oven to measure the inside temperature. Both thermocouples were placed through a tiny hole so that the oven could be assumed as a closed system. The oven and the cell were heated simultaneously during the experiments. Figure 5.7 shows the position of the T-type thermocouples and the cell inside the oven.

Figure 5.7. Thermal abuse testing system of a Li-ion cell that was placed in an oven.

The oven tests were conducted under abnormal thermal operating conditions as summarized in Table 5.4.

Table 5.4. The performed oven tests under abnormal thermal operating conditions.

Temperature	C-Rate	Initial SoC	Experimental
90, 95, 110, 115, 155, 185°C	-	1	+
95, 120, 130, 150, 170, 185, 190, 200°C	-	0	+

5.3.2.1. Effects of the Elevated Temperatures on the Voltage Value of the Cell

The electrical and thermal performances of the Li-ion cells are investigated at 90, 95, 110, and 115°C ambient temperatures. Test durations lasted more than 2 hours, including the heating process of the cell, in order to provide a uniform temperature distribution within the cell. Each cell is fully charged before the experiment and had approximately 4.15 V initially. Besides, no current was applied to the cells during the experiments. Figure 5.8 presents the voltage and temperature profiles of the Li-ion cells at various ambient temperatures between 90 to 115°C.

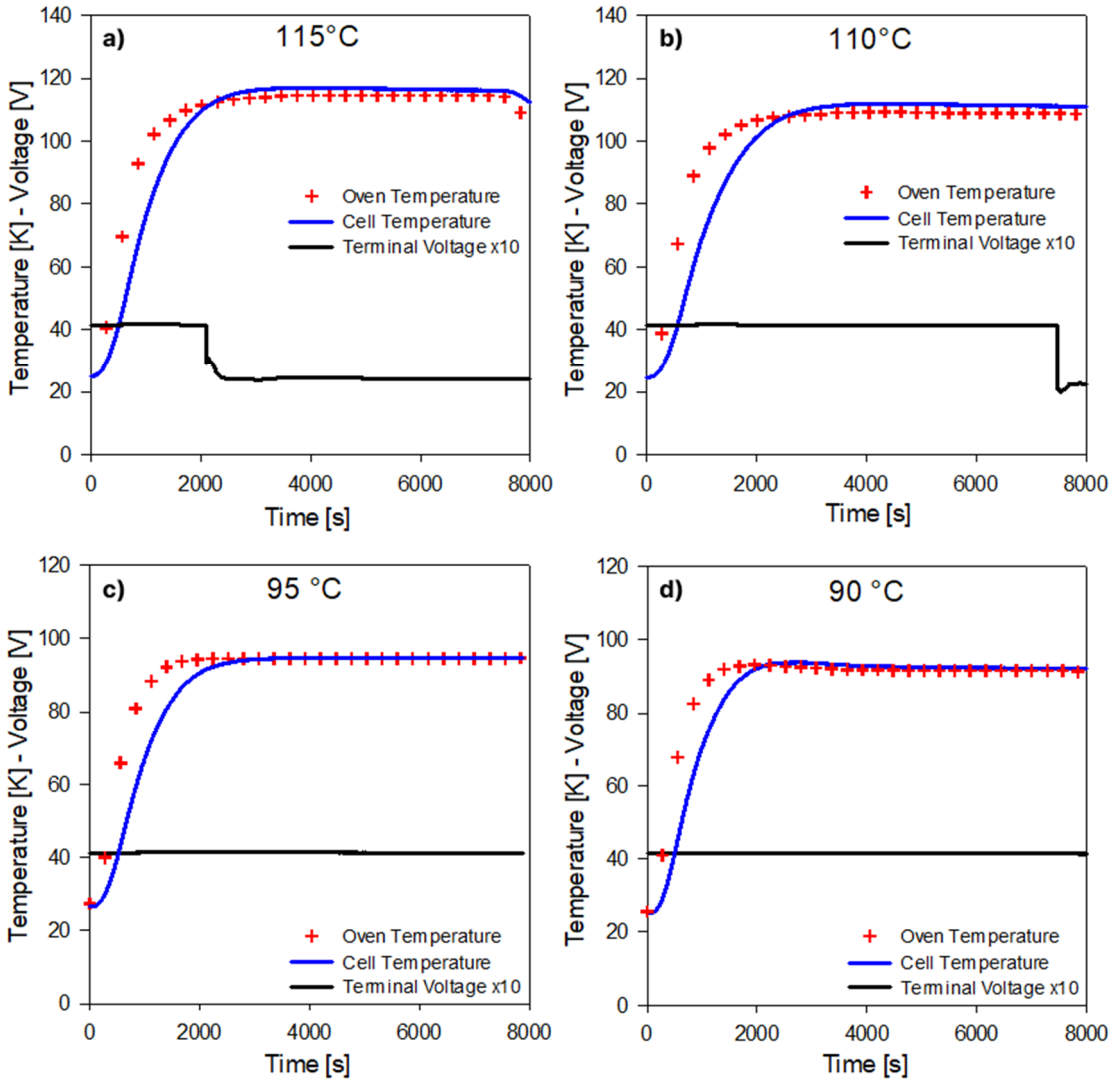

Figure 5.8. Temperature and voltage variations of the cell during the a) 115°C, b) 110°C, c) 95°C, and d) 90°C tests in an oven.

It can be seen from Figure 5.8a that the terminal voltage value of the cell suddenly dropped to 2.9 V when the cell's surface temperature exceeded 110°C. This condition was unexpected, considering there was no applied current to the cell. Therefore, in order to observe the electrical behavior of the cell in detail, an oven test was performed at 110°C, as can be partly followed in Figure 5.8b. The entire process can be observed in Figure 5.9. In this experiment, the oven temperature was kept at around 110°C for five hours, and the cell voltage value suddenly dropped. In this instance, the cooling process of the cell was maintained until the surface temperature of the cell stabilized. Although the cooling process increased

the cell's terminal voltage by approximately 0.7 V, it is still much lower than the initial value. Therefore, it can be deduced that the voltage decrement is not due to the inaccuracy in temperature measurements at high temperatures; but it is the consequence of the high-temperature conditions.

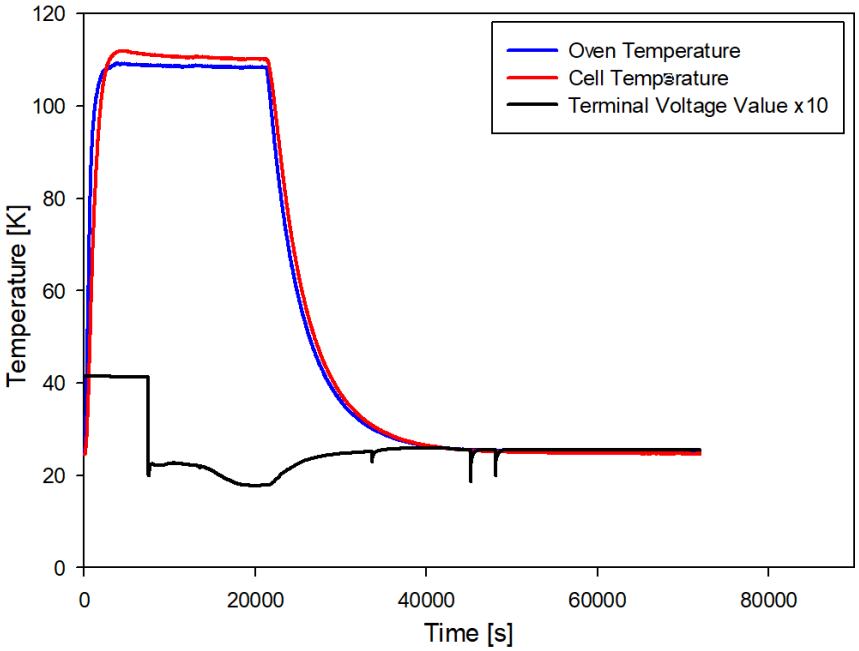

Figure 5.9. Temperature and voltage variations of the cell during the 110°C oven test.

Lastly, 95°C (Figure 5.8c) and 90°C (Figure 5.8d) oven tests were performed to investigate the voltage variation of the cell at elevated temperatures. The voltage value of the cell was decreased only by 25mV during the 95°C oven test. No significant voltage drop was observed during each experiment.

Table 5.5 indicates essential cell characteristics regarding the voltage drop conditions. It shows that the critical surface temperature for the voltage drop is 110°C, and after this point, the battery can be presumed dead.

Table 5.5. Essential cell characteristics regarding the voltage drop conditions at 90, 95, 110, and 115°C.

Cell	Maximum Oven Temperature (°C)	Voltage Drop Starting Time (s)	Voltage Drop Starting Temperature Cell/Oven (°C)
Figure 5.8a	111.7*	2102	110.8/111.7
Figure 5.8b	112*	7471	108.92/111.1
Figure 5.8c	94.7	-	-
Figure 5.8d	93.3	-	-

* Before the voltage drop.

5.3.2.2. Oven Test Results of the Li-ion Batteries at 0 SoC

In this subsection, fully charged Li-ion cells were heated in the oven. No current was applied to the batteries during the experiments. Li-ion cells were exposed to various operating temperatures from 95°C to 200°C, and the results are presented in the given figure below. Note that in these figures, TR implies the TR condition.

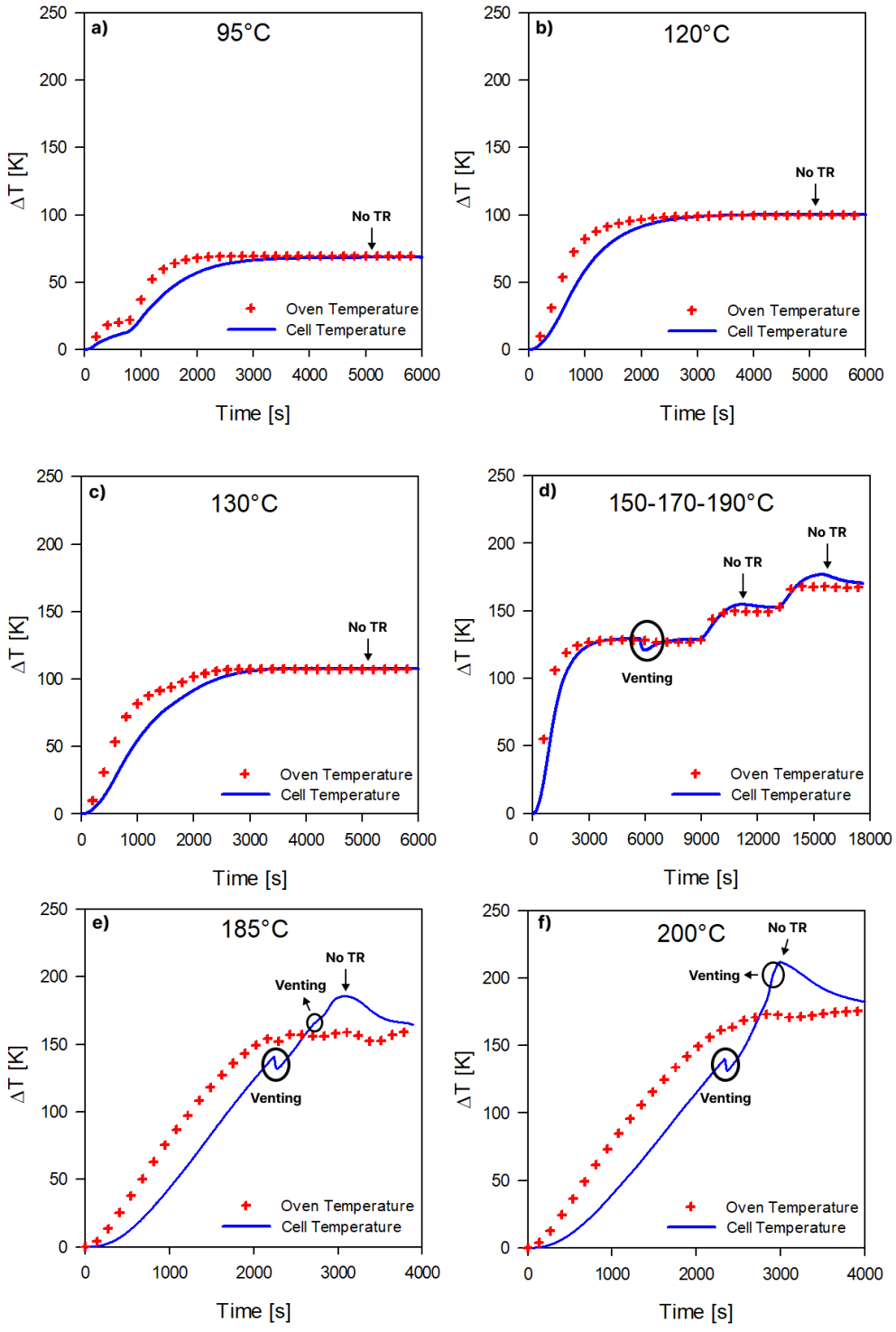

Figure 5.10. Oven and cell surface temperature differences during the a) 95°C, b) 120°C, c) 130°C, d) 150, 170, and 190°C, e) 185°C, and f) 200°C oven tests.

Figures 5.10a, 5.10b, and 5.10c state that neither TR nor battery venting was observed during these thermal abuse conditions up to 130°C operating temperature. On the other hand, Figure 5.10d shows the oven test results at varying temperatures. The cell venting was observed approximately 6000 seconds later during the 150°C test. The venting process instantly decreased the cell temperature by nearly 8.5°C, but then the cell reached the oven temperature again. Later, the oven temperature was set to 170 and 190°C after 9000 and 13000 seconds, respectively. It is important to note that in these tests, the cell temperature is always higher than the oven temperature due to electrochemical reactions. However, no TR was observed after a total of 5 hours of oven test at various operating temperatures. Figures 5.10e and 5.10f investigate the thermal behavior of the Li-ion battery at 185 and 200°C, respectively. Both cells were exposed to the venting process, which caused an approximately 9°C decrease in cell surface temperature. The second ventilation process affected the temperature curve trend so that both experiments did not end up with a TR.

Subsequently, two different cells were exposed to 185°C and 200°C oven tests. The thermal behavior of these cells is compared in Figure 5.11.

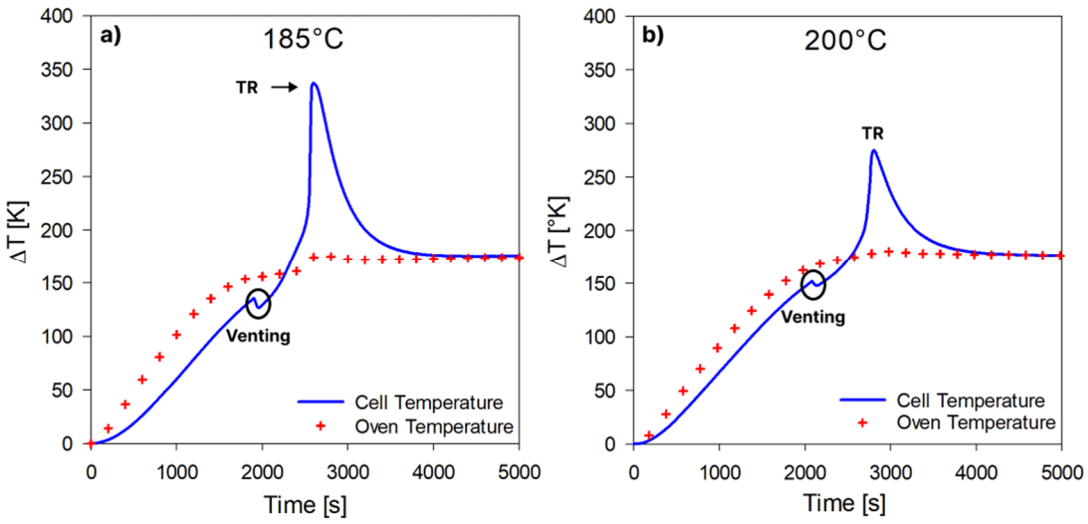

Figure 5.11. Oven and cell surface temperature differences during the a) 185°C, and b) 200°C oven tests.

TR and venting processes were observed during both oven tests. In Figure 5.11a, the venting process caused an approximately 9°C decrease in cell surface temperature, but the TR was inevitable. It was observed that the surface temperature of the cell increased at 4.8°C/sec rates during the TR and exceeded 359°C. On the other hand, in the second case, the venting process decreased the cell's surface temperature only by 3.9°C. Besides, the surface temperature increased with a maximum 1.52°C/sec rate up to 298°C. Note that the second cell was exposed to a high temperature experiment before. Therefore, it is interesting to observe that the cell used in oven tests was exposed to the TR later than the regular cell. In addition, the second cell's maximum surface temperature was observed at 61°C lower compared to that of the other cells. These conditions indicate that the previous heating tests may have strengthened the cell against thermal abuse conditions. The most possible reason is related to the SEI layer decomposition. The SEI layer possibly decomposed during the previous oven tests and may positively affect the cell's TR behavior. Essential cell characteristics are summarized in Table 5.6 for the oven tests performed at 185 and 200°C.

Table 5.6. Essential cell characteristics regarding the conducted oven tests at 185 and 200°C.

Cell Figure Number	Initial Oven Temperature (°C)	Maximum Oven/Cell Temperature (°C)	First Venting Time (sec)	Venting Temperature (°C)	TR Initiation Time* (sec)	TR Initiation Temperature* (°C)
5.10e	28.37	187.4/214.1	2237	169.4	-	-
5.11a	22.77	188.2**/359.7	1897	158.2	2543	248.5
5.10f	28.76	202.2/240.6	2336	169.1	-	-
5.11b***	23.14	201.1**/298.1	2076	174.9	2754	263

* when °C/s exceeds 1°C. ** Before TR. *** Used in the oven tests before

According to the table, two cases did not end with a TR and both had venting for the second time. In these cases, the maximum cell temperature did not exceed

240.64°C. Besides, the first venting processes occurred later than expected at high temperatures of around 170°C. For the cases presented in Figure 5.11, the cell temperature exceeded 298°C during the TR. These cells had only one venting process that took place before the TR.

Eventually, after the SoC=0 tests, it can be said that the venting behavior strongly influences the thermal behavior of the fully discharged cell at elevated temperatures. The second venting process affects the thermal cell profile and may protect the cell from TR. On the other hand, the results showed that there was no specific time or surface temperature for the first venting process to have occurred, but all helped to decrease the battery's surface temperature between 3.9 to 9°C.

Although the surface cell temperature of 360°C was reached in the SoC=0 test, there was no explosion or fire, which also shows the importance of taking precautions against the TR condition as well as possible. Additionally, considering the test results, it can be deduced that the repeatability of the experiments conducted at SoC=0 is quite low.

5.3.2.3. Oven Test Results of the Li-ion Batteries at 1 SoC

Fully charged Li-ion cells were exposed to oven tests at elevated operating temperatures without applying any current. Each experiment resulted in a colossal explosion and local fire around the Li-ion cell. The explosion also forced the oven door to open so that the temperature decreased after the TR. Therefore, the results are shown until the TR. After the explosion, the dry chemical powder was sprayed on the Li-ion cell to prevent fire propagation. Figure 5.12 shows the oven and cell temperature differences during the 155 and 185°C oven tests. During these tests, the oven temperature was tried to be kept constant at the adjusted value, but the ventilated gasses and the heat generation within the cell affected the temperature control in the oven resulting in a relatively low temperature difference up to 4°C.

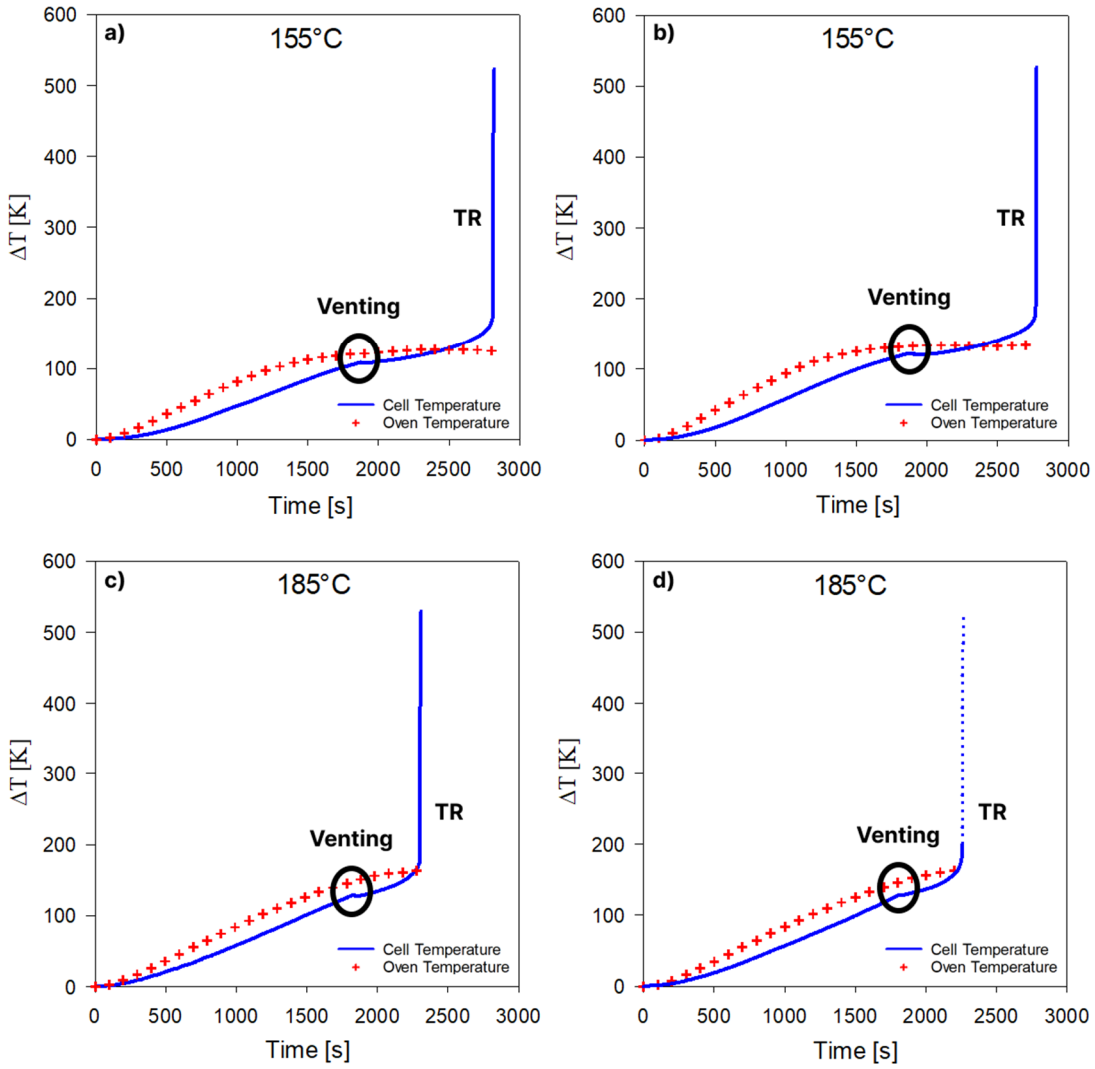

Figure 5.12. Oven and cell surface temperature differences during the 155°C (a, b), and 185°C (c, d) oven tests.

The results indicate that the venting process decreases the increase of in surface temperature in each cell, but the TR was still inevitable. The venting caused an instant and tiny temperature drop, which is noticeable but not as effective as the zero SoC case in battery protection. Besides, no second venting process was observed during each experiment. Since all the tests ended up with an explosion and fire, it is not reasonable to rely on the data of the maximum surface temperature. However, one can compare some essential characteristics, such as

the venting time and temperature, and TR initiation time and temperature, in Table 5.7.

Table 5.7. Essential cell characteristics regarding the conducted oven tests at 155 and 185°C.

Cell Figure Number	Initial Oven Temperature (°C)	Maximum Oven Temperature** (°C)	Venting Time (sec)	Venting Temperature (°C)	TR Initiation Time* (sec)	TR Initiation Temperature* (°C)
5.12a	21.2	156.3	1858	153.8	2771	199.4
5.12b	28.5	155.4	1871	136.8	2810	200.7
5.12c	23	188.9	1816	150.9	2299	198.9
5.12d	21	189.1	1806	148.6	2254	200.8

* when °C/s exceeds 1°C.

** Before TR.

The results show that the cell's thermal characteristics at elevated temperatures are compatible except for the venting temperature at 155°C test in Figure 5.12b. As expected, venting appeared slightly earlier during the 185°C tests compared to the 155°C tests. Besides, it can be conducted from the given results that as the oven temperature increases, the TR occurs earlier. In addition, the TR initiates after similar surface temperatures in 155 and 185°C conditions.

Consequently, the oven test results of the fully charged and discharged cells can be compared. First, it can be clearly said that the discharged battery is safer than the charged battery when comparing the thermal behaviors under the same operating conditions. It should also be stated that all the thermal abuse tests of the completely charged cells ended with a massive explosion and fire. Additionally, the TR characteristics are different in each case. At the same oven temperature, 185°C, the completely charged Li-ion cell went into the TR earlier than the completely discharged cell, followed by Figures 5.11a, 5.12c, and 5.12d.

Besides, fully charged cells had experienced the TR and exploded at 155°C, but fully discharged cells may not even go into a TR at 200°C in some situations.

5.4. Physical Conditions of the Batteries After the Abuse Tests

The final physical conditions of the batteries that were exposed to the different thermal abuse conditions are presented in Figure 5.13. On the other hand, Table 5.8 indicates the battery's final venting and TR conditions during the heating tests.

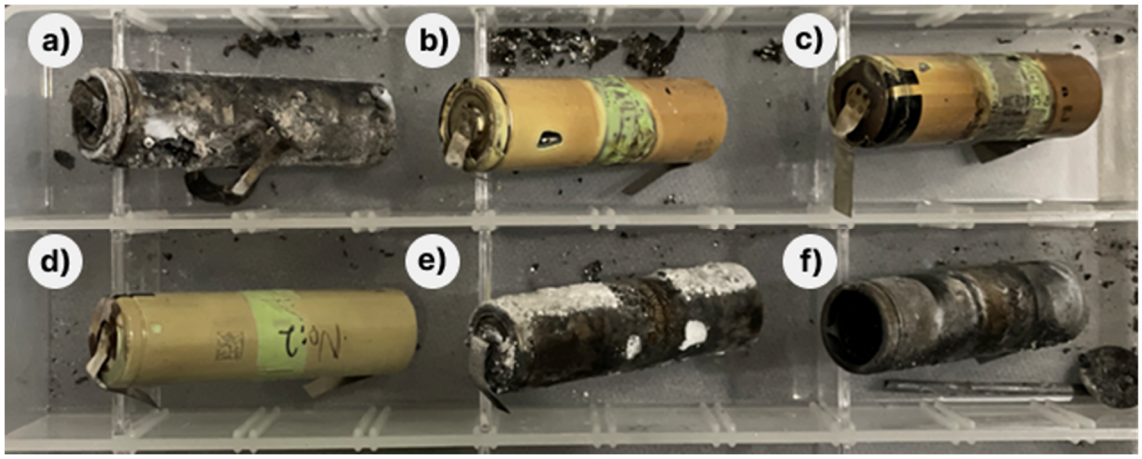

Figure 5.13. Li-ion batteries that were exposed to thermal abuse condition.

Table 5.8. Venting and TR conditions of the heated Li-ion batteries at 0 and 1 SoC.

Cell	Initial Capacity (mAh)	Test	SoC	Venting	TR
a	3174	Film Heater	1	+	+
b	3001	Oven	0	+	+
c	2947	Oven	0	+	+
d	2986	Oven	0	+	-
e	3215	Oven	1	+	+
f	3218	Oven	1	+	+

6. CONCLUSIONS

This doctoral thesis investigates the thermal and electrical behaviors of Li-ion batteries under normal and abuse operating conditions. This study involves both experimental and modeling parts. In the simulation part, first, an axisymmetric 2-D Lumped model was developed. In this model, constant and variable internal resistance approaches were used to estimate a cylindrical Li-ion battery's thermal and electrical characteristics during various discharge rates at different operating temperatures. Then, a 1-D electrochemical model was coupled with a 3-D thermal model to predict the electrical and thermal behaviors of a Li-ion cell. In this model, charge and mass transfers of solids and liquids within the cell were investigated. The 1-D electrochemical model was used to accurately predict the voltage variation and the heat generation within the cell. A thermal model was then coupled with this model and used to predict the cell's thermal behavior during discharging processes. In addition, the developed model was modified to include the effects of heat generation due to increasing temperature using related Arrhenius equations and the simulations were carried out for the film heater tests at 0 and 1 SoC conditions.

The electrochemical-thermal coupled model includes a large number of electrochemical, and thermal parameters. A comprehensive study was done to obtain these parameters for the NCR18650b Li-ion cells. Moreover, a sensitivity analysis was done to observe the electrical and thermal effects of some parameters. First, the simulations were conducted with various input parameters to investigate their effects on the cell’s voltage and temperature predictions during 0.5, 1, and 1.5C rate discharging processes. Then, the model and test results were compared on the basis of RMS and maximum errors. Finally, the sensitivity analysis of the geometrical, thermal, electrochemical parameters was performed and the effective parameters that can alter the cell’s electrical and thermal behavior during the discharging were determined.

In the experimental part of this thesis study, a battery testing system was used to define related electrical and thermal parameters such as specific heat, density, and OCV. On the other hand, the testing system was used to charge or discharge the battery at different C rates under various operating temperatures. Besides, TR tests were performed in an oven at different operating temperatures. These tests were conducted for both completely charged and discharged cells. In addition, the voltage variation of the cell was observed at elevated ambient temperatures. Lastly, a film heater covered around the cell was used to observe the TR behavior of the cell during heating.

The following conclusions can be drawn from the experimental and numerical studies that were conducted in the scope of this thesis study.

Conclusions of the 2-D axisymmetric lumped model using constant internal resistance approach.

- The model and experimental results at various discharging processes and ambient conditions were found in good agreement.

- The simulation results were more accurate at 20°C operating condition due to the stability of the cell resistance in a SOC range between 1-0.2. This shows that applying the constant internal resistance approach cannot be reasonable at extreme operating conditions. On the other hand, it was found that the cell temperature is greatly influenced by the operating temperature as it affects heat production.

- The results show that the cell capacity significantly decreases at cold ambient. Moreover, the increment in cell resistance causes higher heat generation which also leads to a higher temperature increment within the cell during the discharging processes at cold ambient. Besides, it can be suggested from the given results that the batteries should be discharged at low C rates in order to provide a better voltage variation at cold operating conditions.

Conclusions of the 2-D axisymmetric lumped model using variable internal resistance approach.

- The voltage and temperature predictions of the lumped model were compared with the test results and found reasonable in each case.

- The results show that the both concentration and activation overpotentials can be neglected for simplicity since their contributions to the voltage losses are relatively small.

- The results state that the operating temperature inversely influences the battery resistance during a discharging process. On the other hand, the movement of Li-ions becomes more difficult towards the end of the discharging process so that the cell resistance increases. Therefore, it is recommended that the batteries should not be fully discharged to provide a uniform internal resistance within the cell.

- The temperature predictions were compared with the experimental data and found consistent. The estimations at low temperatures are a little bit deviating around the experimental results since the deterioration within the cell characteristics.

- It can be deduced from the presented model results that the heat dissipation by radiation should not be neglected, especially at high discharge rates even though the natural convection affects the heat dissipation rate further.

Conclusions of the electrochemical and thermal model.

- Careful and judicial selection of geometric, electrochemical and thermal parameters is absolutely necessary for successful modeling Li-ion cells.

- For low discharge rates, the temperature distribution within the cell is almost uniform. The temperature differences within the cell were obtained as 0.18°C and 0.68°C, after the 0.5C and 1C rate discharging processes, respectively.

- Mandrel material affects the temperature distribution inside the battery. The maximum temperature difference was found to be 1.41°C and 1.46°C after a 1.5C rate discharging process for the nickel and the nylon mandrel cell, respectively. Nylon material causes a small cold temperature region at the surface of the mandrel. Besides, the low conductive nylon mandrel also changes the maximum temperature region to the outside of the mandrel.

- The predicted temperature and voltage profiles follow the same trend as the experimental data and are consistent at each discharging condition. The maximum calculated root mean square errors were obtained as 0.11 V for the voltage predictions, and 0.92°C for the temperature predictions. Therefore, the developed model can predict the thermal and electrical performances of the Li-ion cell successfully.

Conclusions of the sensitivity analysis.

- The simulation results reveal that each geometrical, electrochemical parameter somehow alters the predicted voltage and temperature profiles of a discharging cell. On the other hand, none of the thermal parameters affects the model results, except the heat capacity which has a minor impact, within the range investigated.

- The most dominant parameters in terms of the cell's thermal and electrical characteristics can be listed as electrode thicknesses, electrolyte phase volume fractions, particle radius of electrodes, and the Bruggeman coefficient considering each discharging condition. Therefore, these

parameters should be carefully selected during modelling of Li-ion batteries.

Conclusions of the thermal abuse tests and simulations,

- The oven experiments ended up with an explosion and fire for the charged Li-ion batteries on the contrary to the fully discharged cells. Besides, it can be conducted from the given results that as the oven temperature increases, the TR occurs earlier.

- The abusive oven and film heater experiments also denoted that the venting behavior strongly influences the thermal behavior of the Li-ion cells at high temperatures. Although there is only one venting process for the charged Li-ion cells, multiple venting processes are observed in the SoC=0 experiments which affect the battery's thermal profile and may protect the battery from TR. The results also showed that there is no specific time or surface temperature for the first venting process to have appeared, but all noticeably decrease the surface temperature of the battery.

- It can be denoted that the repeatability of the experiments conducted at SoC=0 is quite low based on the presented test results.

- The order of the decomposition reactions is obtained as SEI layer, the negative and positive electrode, and electrolyte, respectively. The SEI layer decomposes first but contributes less to heat generation than the other components. Besides, the most effective reaction in terms of the generated heat is observed as the decomposition reaction within the negative electrode.

6.1. Future Work

The experimental and numerical studies regarding Li-ion batteries can be improved based on the results of this thesis. The OCV value of the cell can be measured for both electrodes to enhance the accuracy of the electrochemical-thermal model. In addition, various effective parameters found by the sensitivity analysis can be measured and implemented into the electrochemical-thermal model. On the other hand, the amount of heat generation can be obtained by the appropriate calorimetry-based measurement devices so that the accuracy of the simulation results can be enhanced.

The calorimetric methods can also be an option to obtain the abuse model parameters for various SoC conditions. The heat source within the cell is usually modeled considering the Arrhenius-type temperature-dependent equations. However, the abuse model can be modified to include the effects of the venting process to accurately predict the entire discharging process during the heating.

Finally, the thermal and electrical behaviors of the Li-ion battery packages can be investigated under normal and abuse operating conditions. The effect of using packages, and different pack configurations, can be observed by numerical and experimental methods.

REFERENCES

[1] Y. Nishi, Lithium ion secondary batteries; past 10 years and the future, Journal of Power Sources, 100 (2001) 101-106.

[2] A.A. Pesaran, Battery thermal models for hybrid vehicle simulations, Journal of Power Sources, 110 (2002) 377-382.

[3] R. Bubbico, V. Greco, C. Menale, Hazardous scenarios identification for Li-ion secondary batteries, Safety Science, 108 (2018) 72-88.

[4] H. Liu, Z. Wei, W. He, J. Zhao, Thermal issues about Li-ion batteries and recent progress in battery thermal management systems: A review, Energy conversion and management, 150 (2017) 304-330.

[5] J.-M. Tarascon, M. Armand, Issues and challenges facing rechargeable lithium batteries, Materials for sustainable energy: a collection of peer-reviewed research and review articles from Nature Publishing Group, World Scientific (2011), pp. 171-179.

[6] D. Li, D.L. Danilov, H.J. Bergveld, R.-A. Eichel, P.H. Notten, Understanding battery aging mechanisms, Future lithium-ion batteries (2019), pp. 220-250.

[7] A. Aktaş, Y. Kirçiçek, Chapter 5 - Solar Hybrid Systems and Energy Storage Systems, in: A. Aktaş, Y. Kirçiçek (Eds.) Solar Hybrid Systems, Academic Press (2021), pp. 87-125.

[8] M.H. Shamsi, Analysis of an electric Equivalent Circuit Model of a Li-Ion battery to develop algorithms for battery states estimation, 2016.

[9] K. Ramalingam, C. Indulkar, Chapter 3 - Solar Energy and Photovoltaic Technology, in: G.B. Gharehpetian, S.M. Mousavi Agah (Eds.) Distributed Generation Systems, Butterworth-Heinemann (2017), pp. 69-147.

[10] C. Bommier, X. Ji, Electrolytes, SEI formation, and binders: a review of nonelectrode factors for sodium-ion battery anodes, Small, 14 (2018) 1703576.

[11] S.K. Heiskanen, J. Kim, B.L. Lucht, Generation and evolution of the solid electrolyte interphase of lithium-ion batteries, Joule, 3 (2019) 2322-2333.

[12] D. Bernardi, E. Pawlikowski, J. Newman, A general energy balance for battery systems, Journal of the Electrochemical Society, 132 (1985) 5.

[13] W.-c. LI, S.-g. LU, Thermal behavior of C/LiFePC> 4 power secondary battery, The Chinese Journal of Nonferrous Metals, 22 (2012) 1156-1162.

[14] V.V. Viswanathan, D. Choi, D. Wang, W. Xu, S. Towne, R.E. Williford, J.-G. Zhang, J. Liu, Z. Yang, Effect of entropy change of lithium intercalation in cathodes and anodes on Li-ion battery thermal management, Journal of Power Sources, 195 (2010) 3720-3729.

[15] S. Bazinski, X. Wang, The influence of cell temperature on the entropic coefficient of a lithium iron phosphate (LFP) pouch cell, Journal of The Electrochemical Society, 161 (2013) A168.

[16] G.G. Botte, B.A. Johnson, R.E. White, Influence of some design variables on the thermal behavior of a lithium-ion cell, Journal of the Electrochemical Society, 146 (1999) 914.

[17] S. Al Hallaj, H. Maleki, J.-S. Hong, J.R. Selman, Thermal modeling and design considerations of lithium-ion batteries, Journal of Power Sources, 83 (1999) 1-8.

[18] V. Srinivasan, C. Wang, Analysis of electrochemical and thermal behavior of Li-ion cells, Journal of The Electrochemical Society, 150 (2002) A98.

[19] K. Smith, C.-Y. Wang, Power and thermal characterization of a lithium-ion battery pack for hybrid-electric vehicles, Journal of Power Sources, 160 (2006) 662-673.

[20] Y. Chen, J.W. Evans, Heat transfer phenomena in lithium/polymer-electrolyte batteries for electric vehicle application, Journal of the Electrochemical Society, 140 (1993) 1833.

[21] T.M. Bandhauer, S. Garimella, T.F. Fuller, A critical review of thermal issues in lithium-ion batteries, Journal of the Electrochemical Society, 158 (2011) R1.

[22] C.G. Motloch, J.P. Christophersen, J.R. Belt, R.B. Wright, G.L. Hunt, R.A. Sutula, T. Duong, T.J. Tartamella, H.J. Haskins, T.J. Miller, High-power battery testing procedures and analytical methodologies for HEV's, SAE Transactions, (2002) 797-802.

[23] A. Väyrynen, J. Salminen, Lithium ion battery production, The Journal of Chemical Thermodynamics, 46 (2012) 80-85.

[24] A. Pesaran, S. Santhanagopalan, G. Kim, Addressing the impact of temperature extremes on large format li-ion batteries for vehicle applications (presentation), National Renewable Energy Lab.(NREL), Golden, CO (United States), 2013.

[25] J. Jaguemont, L. Boulon, Y. Dubé, A comprehensive review of lithium-ion batteries used in hybrid and electric vehicles at cold temperatures, Applied Energy, 164 (2016) 99-114.

[26] M. Petzl, M. Kasper, M.A. Danzer, Lithium plating in a commercial lithium-ion battery–A low-temperature aging study, Journal of Power Sources, 275 (2015) 799-807.

[27] G. Nagasubramanian, Electrical characteristics of 18650 Li-ion cells at low temperatures, Journal of Applied Electrochemistry, 31 (2001) 99-104.

[28] S. Nejad, D. Gladwin, D. Stone, A systematic review of lumped-parameter equivalent circuit models for real-time estimation of lithium-ion battery states, Journal of Power Sources, 316 (2016) 183-196.

[29] M. Chen, G.A. Rincon-Mora, Accurate electrical battery model capable of predicting runtime and IV performance, IEEE transactions on energy conversion, 21 (2006) 504-511.

[30] R.E. Gerver, J.P. Meyers, Three-dimensional modeling of electrochemical performance and heat generation of lithium-ion batteries in tabbed planar configurations, Journal of The Electrochemical Society, 158 (2011) A835.

[31] A. Tourani, P. White, P. Ivey, The estimation of electric vehicle battery cell temperatures in driving cycles based onNEDC1, Vehicle Thermal Management Systems Conference Proceedings (VTMS11): 15-16 May 2013, Coventry Technocentre, UK, Elsevier, 2013, pp. 279.

[32] W. Huo, H. He, F. Sun, Electrochemical–thermal modeling for a ternary lithium ion battery during discharging and driving cycle testing, RSC Advances, 5 (2015) 57599-57607.

[33] S. Basu, K.S. Hariharan, S.M. Kolake, T. Song, D.K. Sohn, T. Yeo, Coupled electrochemical thermal modelling of a novel Li-ion battery pack thermal management system, Applied Energy, 181 (2016) 1-13.

[34] B. Mortazavi, H. Yang, F. Mohebbi, G. Cuniberti, T. Rabczuk, Graphene or h-BN paraffin composite structures for the thermal management of Li-ion batteries: a multiscale investigation, Applied Energy, 202 (2017) 323-334.

[35] Y. Chen, W. Huo, M. Lin, L. Zhao, Simulation of electrochemical behavior in Lithium ion battery during discharge process, Plos one, 13 (2018) e0189757.

[36] K. Darcovich, D. MacNeil, S. Recoskie, B. Kenney, Coupled electrochemical and thermal battery models for thermal management of prismatic automotive cells, Applied Thermal Engineering, 133 (2018) 566-575.

[37] S. Kosch, Y. Zhao, J. Sturm, J. Schuster, G. Mulder, E. Ayerbe, A. Jossen, A Computationally Efficient Multi-Scale Model for Lithium-Ion Cells, Journal of The Electrochemical Society, 165 (2018) A2374-A2388.

[38] M. Mastali, E. Foreman, A. Modjtahedi, E. Samadani, A. Amirfazli, S. Farhad, R.A. Fraser, M. Fowler, Electrochemical-thermal modeling and experimental validation of commercial graphite/LiFePO4 pouch lithium-ion batteries, International Journal of Thermal Sciences, 129 (2018) 218-230.

[39] C.-C. Chang, S.-Y. Huang, W.-H. Chen, Thermal and solid electrolyte interphase characterization of lithium-ion battery, Energy, 174 (2019) 999-1011.

[40] T. Özdemir, A. Amini, Ö. Ekici, M. Köksal, Experimental assessment of the lumped lithium–ion battery model, E3S Web of Conferences, EDP Sciences, 2019, pp. 01022.

[41] X. Yang, P. Yang, Z. Zhang, Y. Duan, J. Hu, Experimental and numerical study on thermal performance of Li (NixCoyMnz) O2 spiral-wound lithium-ion batteries, Applied Thermal Engineering, 138 (2018) 446-455.

[42] D. Huang, H. Xie, H. Ma, Q. Sun, Driving cycle prediction model based on bus route features, Transportation Research Part D: Transport and Environment, 54 (2017) 99-113.

[43] E. Gümüşsu, Ö. Ekici, M. Köksal, 3-D CFD modeling and experimental testing of thermal behavior of a Li-Ion battery, Applied Thermal Engineering, 120 (2017) 484-495.

[44] D. Chalise, K. Shah, T. Halama, L. Komsiyska, A. Jain, An experimentally validated method for temperature prediction during cyclic operation of a Li-ion cell, International Journal of Heat and Mass Transfer, 112 (2017) 89-96.

[45] J. Huang, Z. Li, B.Y. Liaw, Z. Wang, S. Song, N. Wu, J. Zhang, Entropy coefficient of a blended electrode in a lithium-ion cell, Journal of The Electrochemical Society, 162 (2015) A2367.

[46] G. Liu, M. Ouyang, L. Lu, J. Li, X. Han, Analysis of the heat generation of lithium-ion battery during charging and discharging considering different influencing factors, Journal of Thermal Analysis and Calorimetry, 116 (2014) 1001-1010.

[47] M.S. Rad, D. Danilov, M. Baghalha, M. Kazemeini, P. Notten, Adaptive thermal modeling of Li-ion batteries, Electrochimica Acta, 102 (2013) 183-195.

[48] S. Chacko, Y.M. Chung, Thermal modelling of Li-ion polymer battery for electric vehicle drive cycles, Journal of Power Sources, 213 (2012) 296-303.

[49] D.H. Jeon, S.M. Baek, Thermal modeling of cylindrical lithium ion battery during discharge cycle, Energy Conversion and Management, 52 (2011) 2973-2981.

[50] N. Damay, C. Forgez, M.-P. Bichat, G. Friedrich, Thermal modeling of large prismatic LiFePO4/graphite battery. Coupled thermal and heat generation models for characterization and simulation, Journal of Power Sources, 283 (2015) 37-45.

[51] Y. Zhang, Z. Liu, X. Sun, Y. An, X. Zhang, K. Wang, C. Dong, Q. Huo, T. Wei, Y. Ma, Experimental study of thermal charge–discharge behaviors of pouch lithium-ion capacitors, Journal of Energy Storage, 25 (2019) 100902.

[52] K. Chatterjee, P. Majumdar, D. Schroeder, S.R. Kilaparti, Performance analysis of Li-ion battery under various thermal and load conditions, Journal of Electrochemical Energy Conversion and Storage, 16 (2019).

[53] A.M. Aris, B. Shabani, An experimental study of a lithium ion cell operation at low temperature conditions, Energy Procedia, 110 (2017) 128-135.

[54] F. Zhang, F. Guo, H. Huang, A Study of Driving Cycle for Electric Special-purpose Vehicle in Beijing, Energy Procedia, 105 (2017) 4884-4889.

[55] X. Feng, L. Lu, M. Ouyang, J. Li, X. He, A 3D thermal runaway propagation model for a large format lithium ion battery module, Energy, 115 (2016) 194-208.

[56] K.-C. Chiu, C.-H. Lin, S.-F. Yeh, Y.-H. Lin, K.-C. Chen, An electrochemical modeling of lithium-ion battery nail penetration, Journal of Power Sources, 251 (2014) 254-263.

[57] X. Feng, M. Ouyang, X. Liu, L. Lu, Y. Xia, X. He, Thermal runaway mechanism of lithium ion battery for electric vehicles: A review, Energy Storage Materials, 10 (2018) 246-267.

[58] T.G. Zavalis, M. Behm, G. Lindbergh, Investigation of short-circuit scenarios in a lithium-ion battery cell, Journal of The Electrochemical Society, 159 (2012) A848.

[59] V. Ruiz, A. Pfrang, A. Kriston, N. Omar, P. Van den Bossche, L. Boon-Brett, A review of international abuse testing standards and regulations for lithium ion batteries in electric and hybrid electric vehicles, Renewable and Sustainable Energy Reviews, 81 (2018) 1427-1452.

[60] M. Ouyang, D. Ren, L. Lu, J. Li, X. Feng, X. Han, G. Liu, Overcharge-induced capacity fading analysis for large format lithium-ion batteries with LiyNi1/3Co1/3Mn1/3O2+ LiyMn2O4 composite cathode, Journal of Power Sources, 279 (2015) 626-635.

[61] C.F. Lopez, J.A. Jeevarajan, P.P. Mukherjee, Characterization of lithium-ion battery thermal abuse behavior using experimental and computational analysis, Journal of The Electrochemical Society, 162 (2015) A2163.

[62] I. Esho, K. Shah, A. Jain, Measurements and modeling to determine the critical temperature for preventing thermal runaway in Li-ion cells, Applied Thermal Engineering, 145 (2018) 287-294.

[63] P. Peng, Y. Sun, F. Jiang, Thermal analyses of LiCoO2 lithium-ion battery during oven tests, Heat and Mass Transfer, 50 (2014) 1405-1416.

[64] S. Abada, M. Petit, A. Lecocq, G. Marlair, V. Sauvant-Moynot, F. Huet, Combined experimental and modeling approaches of the thermal runaway of fresh and aged lithium-ion batteries, Journal of Power Sources, 399 (2018) 264-273.

[65] P.T. Coman, S. Rayman, R.E. White, A lumped model of venting during thermal runaway in a cylindrical Lithium Cobalt Oxide lithium-ion cell, Journal of Power Sources, 307 (2016) 56-62.

[66] M. Parhizi, M. Ahmed, A. Jain, Determination of the core temperature of a Li-ion cell during thermal runaway, Journal of Power Sources, 370 (2017) 27-35.

[67] P. Huang, P. Ping, K. Li, H. Chen, Q. Wang, J. Wen, J. Sun, Experimental and modeling analysis of thermal runaway propagation over the large format energy storage battery module with Li4Ti5O12 anode, Applied Energy, 183 (2016) 659-673.

[68] J. Anderson, F. Larsson, P. Andersson, B.-E. Mellander, Thermal modeling of fire propagation in lithium-ion batteries, Proceedings of The 24th International Technical Conference on the Enhanced Safety of Vehicles (ESV), Gothenburg, Sweden, 2015, pp. 8-11.

[69] K.F. Yeow, H. Teng, Characterizing thermal runaway of lithium-ion cells in a battery system using finite element analysis approach, SAE International Journal of Alternative Powertrains, 2 (2013) 179-186.

[70] N. Tanaka, W.G. Bessler, Numerical investigation of kinetic mechanism for runaway thermo-electrochemistry in lithium-ion cells, Solid State Ionics, 262 (2014) 70-73.

[71] A.D. Pasquier, F. Disma, T. Bowmer, A.S. Gozdz, G. Amatucci, J.M. Tarascon, Differential Scanning Calorimetry Study of the Reactivity of Carbon Anodes in Plastic Li-Ion Batteries, Journal of The Electrochemical Society, 145 (1998) 472-477.

[72] A. Melcher, C. Ziebert, B. Lei, W. Zhao, J. Luo, M. Rohde, H.J. Seifert, Modeling and Simulation of Thermal Runaway in Cylindrical 18650

Lithium-Ion Batteries, The Proceedings of the 2016 COMSOL Conference, 2016.

[73] X. Feng, J. Sun, M. Ouyang, F. Wang, X. He, L. Lu, H. Peng, Characterization of penetration induced thermal runaway propagation process within a large format lithium ion battery module, Journal of Power Sources, 275 (2015) 261-273.

[74] R. Zhao, J. Liu, J. Gu, A comprehensive study on Li-ion battery nail penetrations and the possible solutions, Energy, 123 (2017) 392-401.

[75] H. Wang, E. Lara-Curzio, E.T. Rule, C.S. Winchester, Mechanical abuse simulation and thermal runaway risks of large-format Li-ion batteries, Journal of Power Sources, 342 (2017) 913-920.

[76] M. Sheikh, A. Elmarakbi, S. Rehman, A combined experimental and simulation approach for short circuit prediction of 18650 lithium-ion battery under mechanical abuse conditions, Journal of Energy Storage, 32 (2020) 101833.

[77] L. Yiding, W. Wenwei, L. Cheng, Z. Fenghao, High-efficiency multiphysics coupling framework for cylindrical lithium-ion battery under mechanical abuse, Journal of Cleaner Production, 286 (2021) 125451.

[78] D. Ren, X. Feng, L. Lu, M. Ouyang, S. Zheng, J. Li, X. He, An electrochemical-thermal coupled overcharge-to-thermal-runaway model for lithium ion battery, Journal of Power Sources, 364 (2017) 328-340.

[79] P.T. Coman, E.C. Darcy, C.T. Veje, R.E. White, Modelling Li-ion cell thermal runaway triggered by an internal short circuit device using an efficiency factor and Arrhenius formulations, Journal of The Electrochemical Society, 164 (2017) A587.

[80] T. Dong, P. Peng, F. Jiang, Numerical modeling and analysis of the thermal behavior of NCM lithium-ion batteries subjected to very high C-rate discharge/charge operations, International Journal of Heat and Mass Transfer, 117 (2018) 261-272.

[81] C. Qi, Y. Zhu, F. Gao, K. Yang, Q. Jiao, Mathematical model for thermal behavior of lithium ion battery pack under overcharge, International Journal of Heat and Mass Transfer, 124 (2018) 552-563.

[82] G.-H. Kim, A. Pesaran, R. Spotnitz, A three-dimensional thermal abuse model for lithium-ion cells, Journal of Power Sources, 170 (2007) 476-489.

[83] G. Guo, B. Long, B. Cheng, S. Zhou, P. Xu, B. Cao, Three-dimensional thermal finite element modeling of lithium-ion battery in thermal abuse application, Journal of Power Sources, 195 (2010) 2393-2398.

[84] A. Melcher, C. Ziebert, B. Lei, M. Rohde, H.J. Seifert, Modeling and simulation of the thermal behavior of Li-ion cells, CEES-Conf., Environmental Testing And Safety Of Batteries and Fuel Cells, Pfinztal-Berghausen, 2014.

[85] D. Ren, X. Liu, X. Feng, L. Lu, M. Ouyang, J. Li, X. He, Model-based thermal runaway prediction of lithium-ion batteries from kinetics analysis of cell components, Applied Energy, 228 (2018) 633-644.

[86] Z. Liao, S. Zhang, K. Li, M. Zhao, Z. Qiu, D. Han, G. Zhang, T.G. Habetler, Hazard analysis of thermally abused lithium-ion batteries at different state of charges, Journal of Energy Storage, 27 (2020) 101065.

[87] H. Kondo, N. Baba, Y. Makimura, Y. Itou, T. Kobayashi, Model validation and simulation study on the thermal abuse behavior of LiNi0. 8Co0. 15Al0. 05O2-based batteries, Journal of Power Sources, 448 (2020) 227464.

[88] P.J. Bugryniec, J.N. Davidson, S.F. Brown, Computational modelling of thermal runaway propagation potential in lithium iron phosphate battery packs, Energy Reports, 6 (2020) 189-197.

[89] Panasonic NCR18650b Lithium-ion Battery Data Sheet, https://pdf1.alldatasheet.com/datasheet-pdf/view/597043/PANASONICBATTERY/NCR18650B.html. (December, 2022).

[90] E. Gümüşsu, Thermal Modeling of Lithium Ion Batteries, Master Thesis in Mechanical Engineering, Hacettepe University, Ankara (2017).

[91] Y. Çengel, A. Ghajar, Heat and Mass Transfer: Fundamentals [and] Applications. New York City, United States: McGraw-Hill Education, 2020.

[92] COMSOL Multiphysics Programming Reference Manual, version 5.4, Stockholm, Sweden, 2018.

[93] I. Dincer, M.A. Rosen, Chapter 18 - Exergy Analysis of Fuel Cell Systems, in: I. Dincer, M.A. Rosen (Eds.) Exergy (Second Edition), Elsevier2013, pp. 363-382.

[94] C.Y. Wang, W.B. Gu, B.Y. Liaw, Micro-Macroscopic Coupled Modeling of Batteries and Fuel Cells: I. Model Development, Journal of The Electrochemical Society, 145 (1998) 3407-3417.

[95] T.L. Bergman, T.L. Bergman, F.P. Incropera, D.P. Dewitt, A.S. Lavine, Fundamentals of heat and mass transfer, John Wiley & Sons2011.

[96] Y. Xie, W. Li, Y. Yang, F. Feng, A novel resistance-based thermal model for lithium-ion batteries, International Journal of Energy Research, 42 (2018) 4481-4498.

[97] M. Hagen, D. Hanselmann, K. Ahlbrecht, R. Maça, D. Gerber, J. Tübke, Lithium–Sulfur Cells: The Gap between the State-of-the-Art and the Requirements for High Energy Battery Cells, Advanced Energy Materials, 5 (2015) 1401986.

[98] D. Krsmanovic, Development of a property forecast tool for flexible compositions of Li-ion batteries, including raw material availability and price forming, Master Thesis in Energy Technology, Uppsala University, Sweeden, 2019.

[99] V.R. Subramanian, V. Boovaragavan, V. Ramadesigan, M. Arabandi, Mathematical model reformulation for lithium-ion battery simulations: Galvanostatic boundary conditions, Journal of The Electrochemical Society, 156 (2009) A260.

[100] M. Doyle, Y. Fuentes, Computer simulations of a lithium-ion polymer battery and implications for higher capacity next-generation battery designs, Journal of The Electrochemical Society, 150 (2003) A706.

[101] J. Christensen, V. Srinivasan, J. Newman, Optimization of lithium titanate electrodes for high-power cells, Journal of The Electrochemical Society, 153 (2006) A560.

[102] S. Brown, N. Mellgren, M. Vynnycky, G. Lindbergh, Impedance as a tool for investigating aging in lithium-ion porous electrodes: II. Positive electrode examination, Journal of the Electrochemical Society, 155 (2008) A320.

[103] K. Kumaresan, G. Sikha, R.E. White, Thermal Model for a Li-Ion Cell, Journal of the Electrochemical Society, 155 (2008) A164.

[104] T.F. Fuller, M. Doyle, J. Newman, Simulation and optimization of the dual lithium ion insertion cell, Journal of the Electrochemical Society, 141 (1994) 1.

[105] P. Albertus, J. Christensen, J. Newman, Experiments on and modeling of positive electrodes with multiple active materials for lithium-ion batteries, Journal of the Electrochemical Society, 156 (2009) A606.

[106] S.G. Stewart, V. Srinivasan, J. Newman, Modeling the performance of lithium-ion batteries and capacitors during hybrid-electric-vehicle operation, Journal of The Electrochemical Society, 155 (2008) A664.

[107] Y. Dai, L. Cai, R.E. White, Simulation and analysis of stress in a Li-ion battery with a blended LiMn2O4 and LiNi0. 8Co0. 15Al0. 05O2 cathode, Journal of Power Sources, 247 (2014) 365-376.

[108] R. Amin, D.B. Ravnsbæk, Y.-M. Chiang, Characterization of electronic and ionic transport in Li1-xNi0. 8Co0. 15Al0. 05O2 (NCA), Journal of the Electrochemical Society, 162 (2015) A1163.

[109] M.W. Verbrugge, B.J. Koch, Electrochemical analysis of lithiated graphite anodes, Journal of The Electrochemical Society, 150 (2003) A374.

[110] N. Yang, X. Zhang, G. Li, D. Hua, Assessment of the forced air-cooling performance for cylindrical lithium-ion battery packs: A comparative analysis between aligned and staggered cell arrangements, Applied Thermal Engineering, 80 (2015) 55-65.

[111] Properties of Nickel 200, the commercially pure grade, https://www.nickel-alloys.net/article/commercially-pure-properties.html. (December, 2022).

[112] S. Chen, C. Wan, Y. Wang, Thermal analysis of lithium-ion batteries, Journal of Power Sources, 140 (2005) 111-124.

[113] S. Garimella, GF Hewitt, GL Shires, TR Bott, Process Heat Transfer, CRC Press, Boca Raton, FL, USA, 1994; 1042 pages; Price: U $94.95, 1998.

[114] Y.-S. Duh, M.-T. Tsai, C.-S. Kao, Characterization on the thermal runaway of commercial 18650 lithium-ion batteries used in electric vehicle, Journal of Thermal Analysis and Calorimetry, 127 (2017) 983-993.

[115] J.K. Carroll, M. Alzorgan, C. Page, A. Mayyas, Active battery thermal management within electric and plug-in hybrid electric vehicles, SAE Technical Papers, 2016 (2016).

[116] M. Taffal, Electro-Thermal Modelling of Lithium-Ion Battery 2019.

[117] Data Sheet of Mechanical and Thermal Properties of Nickel Material, https://www.matweb.com/search/DataSheet.aspx?MatGUID=e6eb83327e534850a062dbca3bc758dc&ckck=1. (December, 2022).

[118] D.R. Baker, M.W. Verbrugge, Temperature and current distribution in thin-film batteries, Journal of the Electrochemical Society, 146 (1999) 2413.

[119] C. Press, Inc., Cleveland, Ohio, Handbook of Chemistry and Physics, (1977).

[120] T. Wang, K. Tseng, J. Zhao, Z. Wei, Thermal investigation of lithium-ion battery module with different cell arrangement structures and forced air-cooling strategies, Applied energy, 134 (2014) 229-238.

[121] M.Y. Pour, Electro-thermal Modeling of Lithium-ion Batteries, Simon Fraser, 2015.

[122] J. Newman, W. Tiedemann, Porous-electrode theory with battery applications, AIChE Journal, 21 (1975) 25-41.

[123] M. Doyle, T.F. Fuller, J. Newman, Modeling of galvanostatic charge and discharge of the lithium/polymer/insertion cell, Journal of the Electrochemical Society, 140 (1993) 1526.

[124] T. Hatchard, D. MacNeil, A. Basu, J. Dahn, Thermal model of cylindrical and prismatic lithium-ion cells, Journal of The Electrochemical Society, 148 (2001) A755.

[125] R. Spotnitz, J. Franklin, Abuse behavior of high-power, lithium-ion cells, Journal of Power Sources, 113 (2003) 81-100.

APPENDICES

Appendix 1: Equations (4.1) to (4.7) in which x denotes the electrode's state of charge condition.

Eq. (4.1):

$$1.4523e\text{-}13\exp\left(\frac{68025.7}{8.314}\left(\frac{1}{T_{ref}}-\frac{1}{T_2}\right)\right)$$

Eq. (4.2):

$$3e\text{-}15\left((1+\tanh(-20(x-0.73))\right)+0.02$$

Equation (4.3):

for x>0.95

$$OCV_e = -162.54x^3 + 449.21x^2 - 413.89x + 127.22$$

for 0.90<x<0.95

$$OCV_e = \frac{-162.54x^3 + 449.21x^2 - 413.89x + 127.22}{2} + \frac{-1.6525x^4 + 3.6877x^3 - 2.7892x^2 + 0.7551x + 0.0629}{2}$$

for 0.2032<x<0.9

$$OCV_e = -1.6525x^4 + 3.6877x^3 - 2.7892x^2 + 0.7551x + 0.0629$$

for x <0.2032

$$OCV_e = 1683.3x^4 - 1148.7x^3 + 286.93x^2 - 31.745x + 1.5005$$

Eq. (4.4):

$$OCV_e = 0.7222 + 0.1387x + 0.029x^{0.5} - \frac{0.0172}{x} + \frac{0.0019}{x^{1.5}}$$
$$+0.2808\exp(0.9 - 15x) - 0.7984\exp(0.4465x - 0.4108)$$

Eq. (4.5):

for 0.001<x<0.0109

$$OCV_e = 0.113 - 0.0208\tanh(15.064x - 8.199) - 2.435(x - 0.440)^3$$
$$+65.394(x - 0.154)^3 - 960.307(x - 0.0897)^3 - 1.006 * 10^7(x - 0.0109)^3$$

for 0.109<x<0.0897

$$OCV_e = 0.113 - 0.0208\tanh(15.064x - 8.199) - 2.435(x - 0.440)^3$$
$$+65.394(x - 0.154)^3 - 960.307(x - 0.0897)^3$$

for 0.0897<x<0.154

$$OCV_e = 0.113 - 0.0208\tanh(15.064x - 8.199) - 2.435(x - 0.440)^3 + 65.394(x - 0.154)^3$$

for 0.154<x<0.440

$$OCV_e = 0.113 - 0.0208\tanh(15.064x - 8.199) - 2.435(x - 0.440)^3$$

for 0.440<x<0.854

$$OCV_e = 0.113 - 0.0208\tanh(15.064x - 8.199)$$

for 0.854<x<0.92

$$OCV_e = 0.113 - 0.0208\tanh(15.064x - 8.199 - 252.707(x - 0.854)^3$$

Eq. (4.6):

$$OCV_e = \frac{-4.656 + 88.669x^2 - 401.119x^4 + 342.909x^6 - 462.471x^8 + 433.434x^{10}}{-1 + 18.933x^2 - 79.532x^4 + 37.311x^6 - 73.083x^8 + 95.96x^{10}}$$

Eq. (4.7):

for $0.36 \le x \le 0.410$

$$OCV_e = 8.535 - 17.059x + 21.038x^2 - 9.153x^3 + 9.875(x - 0.700)^3 - 2.176(x - 0.550)^3 - 1331.866(x - 0.410)^3$$

for $0.410 \le x \le 0.55$

$$OCV_e = 8.535 - 17.059x + 21.038x^2 - 9.153x^3 + 9.875(x - 0.700)^3 - 2.176(x - 0.550)^3$$

for $0.55 \le x \le 0.70$

$$OCV_e = 8.535 - 17.059x + 21.038x^2 - 9.153x^3 + 9.875(x - 0.700)^3$$

for $0.70 \le x \le 0.935z$

$$OCV_e = 8.535 - 17.059x + 21.038x^2 - 9.153x^3$$

for $0.935 \le x \le 0.959$

$$OCV_e = 8.535 - 17.059x + 21.038x^2 - 9.153x^3 + 9.875(x - 0.700)^3 - 5370.872(x - 0.935)^3$$

for $0.959 \le x \le 0.980$

$$OCV_e = 8.535 - 17.059x + 21.038x^2 - 9.153x^3 + 9.875(x - 0.700)^3 - 5370.872(x - 0.935)^3 - 47690.304(x - 0.959)^3$$

Appendix 2: Publications related to the thesis.

Özdemir T., Amini A., Ekici Ö., Köksal, M., Experimental Assessment of the Lumped Lithium Ion Battery Model at Different Operating Conditions, Heat Transfer Engineering, 43 (3-5) **(2021)** 314-325.

Özdemir T., Ekici Ö., Köksal, M., Numerical and experimental investigation of the thermal and electrical characteristics of a lithium ion cell, E3S Web of Conferences, 321 **(2021)** 03007.

Özdemir T., Amini A., Ekici Ö., Köksal, M., Experimental assessment of the lumped lithium–ion battery model, E3S Web of Conferences, 128 **(2019)** 01022.

Appendix 3: Presentations related to the thesis

Özdemir T., Ekici Ö., Köksal, M., Sensitivity analysis of a thermal model for lithium-ion cells, 15th ATE HEFAT 2021, Virtual Conference **(2021)**.

Özdemir T., Ekici Ö., Köksal, M., Numerical and experimental investigation of the thermal and electrical characteristics of a lithium ion cell. 13th ICCHMT Virtual Conference **(2021).**

Özdemir T., Amini A., Ekici Ö., Köksal, M., Experimental assessment of the lumped lithium–ion battery model, 12th ICCHMT Conference, Rome, ITALY **(2019).**

- Özdemir T., Ekici Ö., Köksal, M., E3S Web of Conferences, 321 **(2021)** 03007.
- Amini A., Özdemir T., Ekici Ö., Başlamışlı S. Ç., Köksal, M., Applied Thermal Engineering, 185 **(2021)** 116338.
- Amini A., Özelci B., Özdemir T., Ekici Ö., Başlamışlı S. Ç., Köksal, M., Kocaeli Journal of Science and Engineering, 3 (1) **(2020)** 1-8.
- Özdemir T., Amini A., Ekici Ö., Köksal, M., E3S Web of Conferences, 128 **(2019)** 01022.

Conferences

- **July 2021:** 15th ATE HEFAT 2021, Virtual Conference.
- **May 2021:** 13th ICCHMT 2021, Virtual Conference.
- **September 2019:** 12th ICCHMT 2019, Rome, Italy.
- **September 2019:** ULIBTK'19 22nd Congress of Thermal Sciences and Technology. Kocaeli, Turkey.